Doctoral thesis

Photoproduction of neutral kaons on the deuteron near the threshold

Department of Physics, Tohoku University

Kyo Tsukada

March, 2005

Contents

List of Figures

List of Tables

Chapter 1

Introduction

1.1 Photo/Electro production of strangeness

Strangeness production by electromagnetic interaction gives important information of the strangeness production mechanism, the strength of meson-baryon interactions (coupling constants) and the structure of hadrons (form factor), and it has been performed since the late 1950s both experimentally (Sect. 1.1.1) and theoretically (Sect. 1.1.2) because electromagnetic probe (electrons or real photons) are well understood.

However, the elementary processes of strangeness photoproduction are not well known yet. In Fig. 1.1, the photon energy dependence of total production cross section for all six isospin channels of kaon photoproduction on nucleon target in the threshold region. Although examples of a recent theoretical calculations and experimental data are shown, high quality data are available only for the two K^+ channels, that is $p(\gamma, K^+)\Lambda$ and $p(\gamma, K^+)\Sigma^0$, and a few data for $p(\gamma, K^0)\Sigma^+$. No data have been measured for other three channels, that is $n(\gamma, K^0)\Lambda$, $n(\gamma, K^0)\Sigma^0$ and $n(\gamma, K^+)\Sigma^-$. It is because of the experimental difficulties to measure neutral kaons and to prepare a neutron target.

The precise measurements of other production channels can provide important information to realize the strangeness production mechanism, especially, the $n(\gamma, K^0)\Lambda$ reaction plays an essential role to clarify the strangeness photoproduction (Sect. 1.2).

1.1.1 Previous experimental investigation

The strangeness photoproduction in the threshold region consists of 6 channels as follows,

processes	threshold photon energy (MeV)
$\gamma p \to K^+\Lambda$	911.1
$\gamma p \to K^+\Sigma^0$	1046.1
$\gamma p \to K^0\Sigma^+$	1047.5
$\gamma n \to K^0\Lambda$	915.4
$\gamma n \to K^0\Sigma^0$	1052.1
$\gamma n \to K^+\Sigma^-$	1050.5.

!h

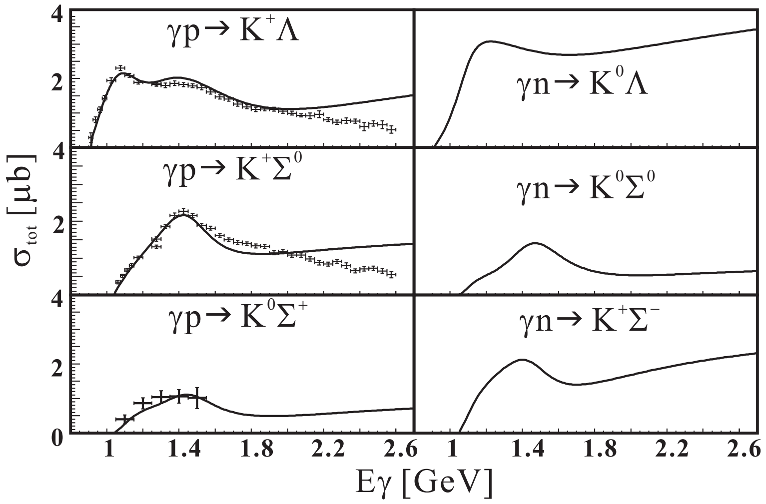

Figure 1.1: *Total cross sections for 6 isospin channels of kaon photoproduction. The data was obtained at SAPHIR [1]. The solid line is the theoretical calculation by Kaon-MAID[2].*

The first generation of investigations of strangeness photo-production had been carried out since the late 1950s. The $p(\gamma, K^+)\Lambda$ reaction was studied from the threshold up to 1.4 GeV by measuring differential cross sections[3, 4, 5, 6, 7, 8], total cross sections[9] and final state Λ polarizations[5, 7]. Some of the experiments used polarized targets[10]. In addition, the measurements with higher energy[11] and those of electro-production[12, 13] were conducted. However, precise measurements of other strangeness production channels were still to be conducted at that time.

Since 1990's, new experiments have been carried out at the accelerator facilities with a photon or electron beam, JLab(CLAS) [14, 15], ELSA(SAPHIR) [16, 1] and SPring-8(LEPS) [17].

Total and differential cross sections and hyperon polarizations of the $p(\gamma, K^+)\Lambda$ and $p(\gamma, K^+)\Sigma^0$ reactions with photon energies from 0.8 to 2.6 GeV were measured at SAPHIR [16] with much higher quality than before. This data lead into the missing resonance interpretation as mentioned above. In this experiment, the cross section of the $p(\gamma, K^0)\Sigma^+$ reaction was also measured, but the statistics was poor. The total cross sections of these reactions are shown in Fig. 1.1. Moreover, the following experiment was also carried out with an extended photon energy range, from 0.85 to 2.65 GeV [1], and further improved data were provided.

The transferred polarization in the exclusive $p(\vec{e}, e'K^+)\Lambda$ reaction was measured by CLAS for the first time at a electron energy of 2.567 GeV. They reported that the kaon angular dependence of the transferred Λ polarizations was not reproduced by the calculations of recent models [14]. The group also measured the $p(\gamma, K^+)\Lambda$ reaction in the photon energies from 0.911 to 2.325 GeV and reported that the bump structure is seen at the energy same to SAPHIR data. However, the magnitude of the cross sections was systematically larger than SAPHIR data at forward angles.

The beam polarization asymmetries for the $p(\vec{\gamma}, K^+)\Lambda$ and $p(\vec{\gamma}, K^+)\Sigma^0$ reaction at the photon energies from 1.5 to 2.4 GeV have been measured at SPring8/LEPS. The asymmetries for both reactions are positive, which are not reproduced by the theoretical calculations [17].

Many physical quantities of kaon production on a proton target have been provided and some can't be explained by the present models. For further realizing the strangeness photoproduction, the investigation of other isospin channels is important.

1.1.2 Previous theoretical investigation

There are various approaches for describing the elementary photoproduction of strangeness. A phenomenological models, which describes the kaon photoproduction processes in terms of hadronic degrees of freedom using effective Lagrangian approach are suitable for low energy region and is called isobar model. A Regge model [18] is appropriate for the higher photon energy region, $E_\gamma \gtrsim 4$ GeV. Chiral perturbation theory[19] may be useful in the threshold region.

The isobar models are based on the Feynman diagrammatic technique in tree levels, which includes Born terms and the resonance terms which exchange resonances as intermediate states. Figure 1.2 shows the Feynman diagrams for the isobar model. In this approach, every intermediate particle is treated as an effective field with its characteristic mass, photo-coupling amplitudes and strong decay widths. The coupling constant for each resonance is not determined by the theory itself and, thus, is treated as a free parameter in the fitting to the experimental data assuming some constraints from isospin symmetry.

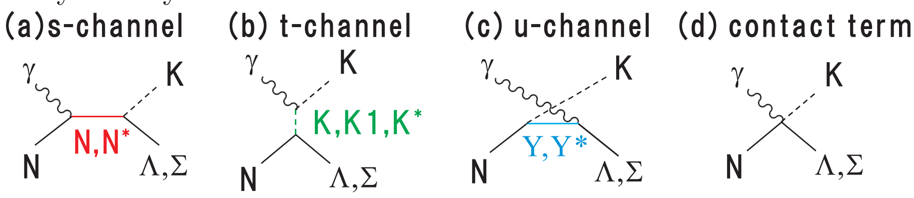

Figure 1.2: *Feynman diagrams used in isobar models.*

For the Born terms, the coupling constants, $g_{K\Lambda p}$ and $g_{K\Sigma^0 p}$, are related to $g_{\pi NN}$ assuming SU(3) flavor symmetry. For the 20 % breaking of the SU(3) symmetry due to the heavy constituent mass of s-quark, the $g_{K\Lambda p}$ and $g_{K\Sigma^0 p}$ are set within

$$-4.5 \; < \; g_{K\Lambda p}/\sqrt{4\pi} < -3.0 \tag{1.1}$$
$$0.9 \; < \; g_{K\Sigma^0 p}/\sqrt{4\pi} < 1.3, \tag{1.2}$$

respectively, in recent models[20]. For nucleon resonances, there are a large number of resonances to be considered in the mass region smaller than 2 GeV/c^2 due to the absence of dominant exchanged baryon resonances. Therefore, the constraints from the crossing symmetry[21, 22] and the duality hypothesis[21] are required so as to reduce the number of parameters in the models.

Historically, the isobar model for kaon photoproduction was developed 40 years ago by Thom[23], in which Feynman diagrams for Born terms and partial wave amplitudes for the resonances were used. However the theoretical analysis made little progress for almost two decades after Thom's work due to lack of experimental data.

Adelseck et al. constructed a refined model using diagrammatic techniques for the resonance terms as well as the Born terms[24]. Relativistic invariance was satisfied in the model. In the following decade, many theoretical models were proposed[20, 21, 22, 25, 26, 27, 28, 29]. By that time, new accelerators and detectors were constructed and new experimental projects just started (Sect.1.1.1). Such experimental conditions triggered the progress of the theoretical investigations.

In the early days, some models did not impose the SU(3) conditions (Eq.1.1,1.2), and other models took wrong phase relations. Most of recent models were constructed requiring these conditions. However, as far as the SU(3) symmetry is realized to the two main coupling constants, the contribution of the Born terms is nonphysically large[30]. To reduce this contribution, hyperon resonances or hadronic form factors need be considered. In this paper, the Kaon-MAID[2] and the Sacray-Lyon A (SLA) model[29], which are the latest theoretical models, are compared with the experimental data.

In the Kaon-MAID model, the hadronic form factors are included. Gauge invariance and current conservation are restored by introducing a contact term(Fig. 1.2(d), [31]). Furthermore, four N* and two Δ (for $K\Sigma$ channel) resonances in s-channel and K^* and K_1 in t-channel are included. Specifically, the resonance $D_{13}(1900)$[32] is newly added, which is needed to reproduce the bump structure around W = 1900 MeV of the total cross section of K^+ photoproduction data obtained by the SAPHIR group[16]. This is one of the missing resonances which have not been observed in pion induced and pion photoproduction reactions but its existence is predicted by the constituent quark model[33]. No hyperon resonances in u-channel is taken into account in the model.

On the other hand, the SLA takes into account four hyperon resonances in u-channel in addition to one N* resonances in s-channel, K^* and K_1 in t-channel. The details of two models are described in Sect. 4.2.

These two models reproduce reasonably well the total cross section of K^+ photoproduction since the parameters are adjusted from those data. However, as mentioned in Sect. 1.1.1, the transferred Λ polarizations for the $p(\vec{e}, e'K^+)\Lambda$ reaction measured by CLAS [14] or the beam polarization asymmetries for the $p(\vec{\gamma}, K^+)\Lambda$ and $p(\vec{\gamma}, K^+)\Sigma^0$ reactions observed by LEPS [17] are not explained by the present theoretical calculations. To realize what resonances are essential in kaon production, the information on other isospin channels are necessary.

1.2 Purpose of the present study

As described in Sect. 1.1.1 and 1.1.2, strangeness photoproduction processes have been studied mainly through the $p(\gamma, K)\Lambda, \Sigma$ reactions. However, the $n(\gamma, K^0)\Lambda$ process has not been experimentally studied. The reaction in the threshold has the following unique features;

- Since no charge is involved in the reaction, the Born term in the t-channel does not contribute.

- The sign of the coupling constant of Σ^0 exchange term in the u-channel is opposite to the $p(\gamma, K^+)\Lambda$ reaction from the isospin symmetry, that is $g_{K^0\Sigma^0 n} = -g_{K^+\Sigma^0 p}$.

Interference among the diagrams in the $K^0\Lambda$ production process is quite different from that of the $K^+\Lambda$ production process because of these characteristics. Besides, the influence from the higher mass resonances is considered to be small near the threshold. Comparing of the K^0 production data with the K^+ production data plays a unique role for the investigation of the strangeness photoproduction mechanism. Figure 1.3 show the elementary cross section for the $K^+\Lambda$ and $K^0\Lambda$ photoproduction. For K^+ production, both the energy dependences and angular distributions agree between the Kaon-MAID and SLA models. It is natural because the model parameters are adjusted to reproduce the K^+ production data.

However, for K^0 production, the calculated cross sections show quite different behavior. This implies that the K^0 photoproduction process can give additional information on the strangeness photoproduction. In the calculation of the K^0 production using SLA, the coupling constant of the K_1 exchange term in t-channel is not fixed and remain as a free parameter. In figure 1.3, the value which is derived in Kaon-MAID model frame work is assumed for SLA ($r_{K_1K\gamma}$ =−0.4474, see Sect. 4.2).

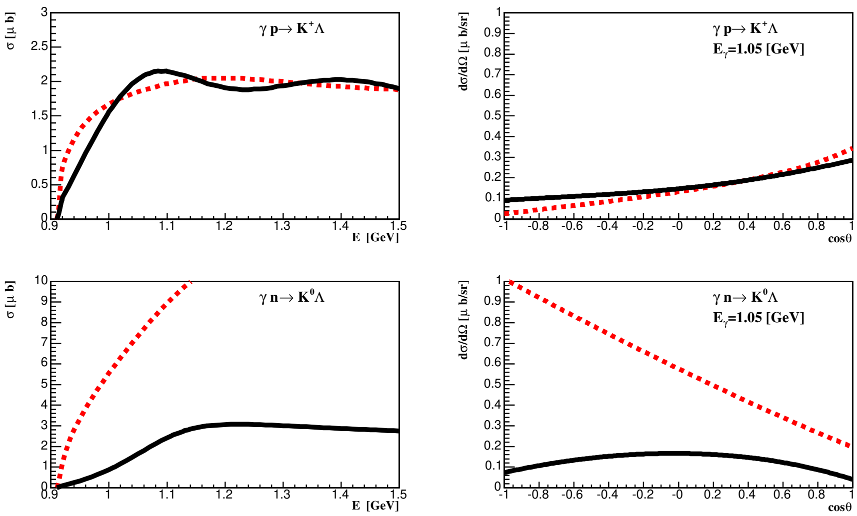

Figure 1.3: *Elementary cross section for $K^+\Lambda$ (upper) and $K^0\Lambda$ (lower) photoproduction in terms of the energy dependence(left) and angular distribution(right). The solid(dashed) curves are calculated from the Kaon-MAID(SLA($r_{K_1K\gamma}$ =−0.4474)).*

We carried out the experiment of the $d(\gamma, K^0)$ reaction in the threshold region, E_γ=0.8 ∼ 1.1 GeV. Prior to the present experiment,an experiment on a carbon target were carried out in March, 2003 [34] with Neutral Kaon Spectrometer (NKS), which was constructed for this experiment. We succeeded in detecting K^0 and analyzing K^0 photoproduction process via the quasi-free process. The measured exciting function of K^0 photoproduction on a carbon target was compared with that of K^+ photoproduction on a carbon target, which was measured by Yamazaki et al. [35]. It was found that the cross sections of K^0 and K^+ were nearly equal. Furthermore, it was shown that the latest isobar models, Kaon-MAID and SLA, could explain the differential cross section of K^+ and K^0 photoproduction on a carbon target based on the quasi-free calculation.

The purpose of the present experiment is investigation of the elementary reaction, $n(\gamma, K^0)\Lambda$, using a deuteron target. Since the Fermi motion of neutron in the deuteron is smaller than that in the carbon, and the structure of the deuteron is simpler than that of the carbon, the measured data can be compared with the theoretical calculation with much smaller ambiguity. It is expected that we can obtain a key information constructing phenomenological models for strangeness photoproduction.

The present thesis is arranged in the following order. Firstly, the experimental method and apparatus are described in Chapter 2. Secondly, details of analysis are presented in Chapter 3. In Chapter 4, the experimental results and comparison with the theoretical calculations based on the Kaon-MAID and SLA are discussed. The contribution of Σ production is also discussed in this chapter. Finally, the conclusion is given in Chapter 5.

Chapter 2

Experiment

In this chapter, experimental method and apparatus are described. The basic idea to measure K^0 is discussed in Sect. 2.1.

In this experiment, K^0 was measured in $\pi^+\pi^-$ decay channel by Neutral Kaon Spectrometer (NKS) which was constructed in the Laboratory of Nuclear Science of Tohoku University (LNS-Tohoku). The detectors system is described in Sect.2.3. This experiment was carried out using 1 GeV photon beam at the second experimental hall in LNS-Tohoku. The photon beam is generated from 1.2 GeV electron beam via bremsstrahlung and tagged by STB-tagger system, which is described in Sect. 2.2.

In order to investigate K^0 elementary production process, the liquid deuterium target was used. The target system was developed for this experiment and provided the stable liquid-state deuterium during the experimental period as described in Sect. 2.4.

The online trigger condition and data acquisition system are explained in Sect. 2.5. In Sect. 2.6, datasets obtained in the present study are summarized.

2.1 Method

We measured $n(\gamma, K^0)\Lambda$ process on a deuteron. Because both K^0 and $\overline{K^0}$ have the same decay modes, generated K^0 can change to $\overline{K^0}$, e.g. via 2π or 3π as intermediate state.

$$K^0 \leftrightarrow \left\{ \begin{array}{c} 2\pi \\ 3\pi \end{array} \right\} \leftrightarrow \overline{K^0}$$

In the view of quark diagram, K^0 and $\overline{K^0}$ are mixed via so-called box diagrams as shown in Fig. 2.1.

Although K^0 and $\overline{K^0}$ are not eigenstate of CP, final states of 2π and 3π are CP eigenstates,

$$\begin{aligned} CP|\pi\pi > &= +1 \cdot |\pi\pi > \\ CP|\pi\pi\pi > &= -1 \cdot |\pi\pi\pi > . \end{aligned}$$

In the assumption of CP conservation in weak interaction, initial state of decay should be also a eigenstate of CP. Such states are made of a linear combination of K^0 and $\overline{K^0}$

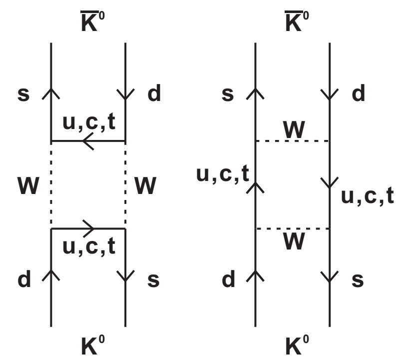

Figure 2.1: *The box diagram of K^0-$\overline{K^0}$ mixing.*

as follows,

$$\begin{aligned}|K_S^0> &= \frac{1}{\sqrt{2}}\{|K^0> -|\overline{K^0}>\},\quad CP|K_S^0>= +1\cdot|K_S^0> \\ |K_L^0> &= \frac{1}{\sqrt{2}}\{|K^0> +|\overline{K^0}>\},\quad CP|K_L^0>= -1\cdot|K_L^0>,\end{aligned}$$

where the phase of $|K^0>$ is chosen so that $C|K^0>= +1\cdot|\overline{K^0}>$.

When K^0 is generated, its state is also described as linear combination of K_S^0 and K_L^0. Therefore, the probability of detecting K^0 as K_S^0 is 50 %. The lifetime of K_L^0 which decays into three pions is longer than that of K_S^0 because the phase space of three pions is smaller than that of two pions. Table 2.1 shows properties of both K_S^0 and K_L^0.

We detected K^0 via the $K_S^0 \to \pi^+\pi^-$ decay channel.

Table 2.1: *Property of K^0.*

	K_S^0	K_L^0
mass	497.648 MeV/c^2	
lifetim($c\tau$)	2.67 cm	15.5 m
decay modes	$\pi^+\pi^-$ (68.6 %)	$3\pi^0$ (21.1 %)
	$2\pi^0$ (31.4 %)	$\pi^+\pi^-\pi^0$ (12.5 %)
		$\pi^\pm\mu^\mp\nu_\mu$ (27.2 %)
		$\pi^\pm e^\mp\nu_e$ (38.8 %)

2.2 Tagged photon beam at Laboratory of Nuclear Science (LNS)

LNS is one of a few laboratories providing photon beams with energy of around 1 GeV. Figure 2.2 shows the schematic view of the experimental hall. The 200 MeV electron beam from LINAC is injected to 1.2 GeV STrecher Booster (STB) ring, boosted up to 1.2 GeV, and kept for 20 sec in the ring.

The photon is generated via bremsstrahlung and scattered electron is tagged by STB-Tagger. Figure 2.3 shows the schematic view of STB-Tagger.

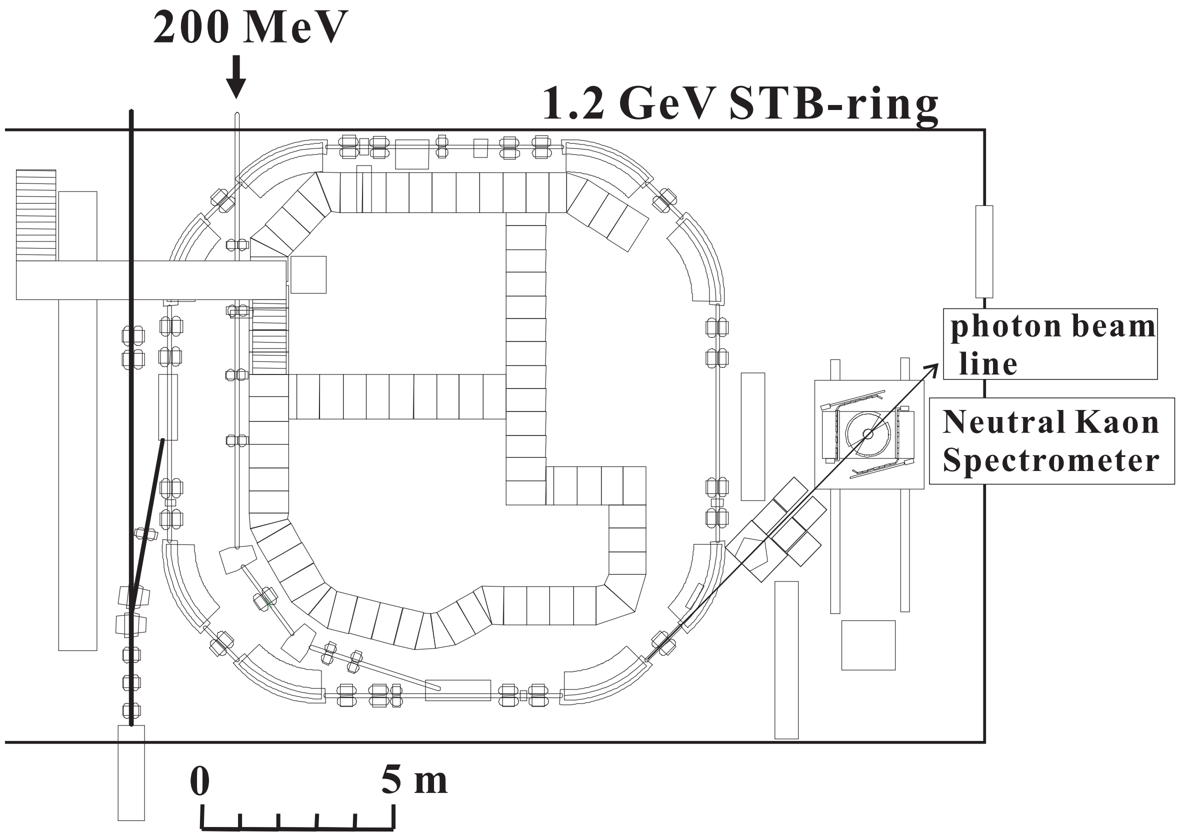

Figure 2.2: *Schematic view of the second experimental hall at LNS*

The STB-Tagger is an internal tagging system and located at one of the bending corners. It consists of an $11\mu m\phi$ carbon string radiator, an analyzing magnet, fifty segments finger plastic scintillation counters (TagF) and twelve segments backup plastic scintillation counters (TagB).

Because the tagger counters are located near the circulating electron beam, large backgrounds exist. The trajectory of the background is not the same as that of the scattered electron from the radiator. Therefore coincidence between TagF and TagB is required to reject the background. One backup counter corresponds to four finger counters in the coincidence logic. Details for the trigger logic are explained in Sect. 2.5.2 and for analysis in Sect. 3.3.

The STB-Tagger system can provide uniform intensity of the photon beam tagged from 0.8 to 1.1 GeV by moving the radiator. When the radiator moves, the orbit of the scattered electron is changed. Therefore, the range of the radiator position is limited so that the shift of arrival point of scattered electron is less than the half width of a tagF.

Figure 2.4 shows the beam cycle. The beam intensity was adjusted to about 2∼3 mA so that summation of the counting rate of tagF was about 2∼3 MHz.

From the energy calibration carried out before [34], the correlation between a segment number of TagF and photon energy was given(described in Sect.3.3.2).

Number of tagged photons are counted by a scaler in each segment of TagF. The method to estimate the number of photon bombarded on the target is described in Sect.3.10.2.

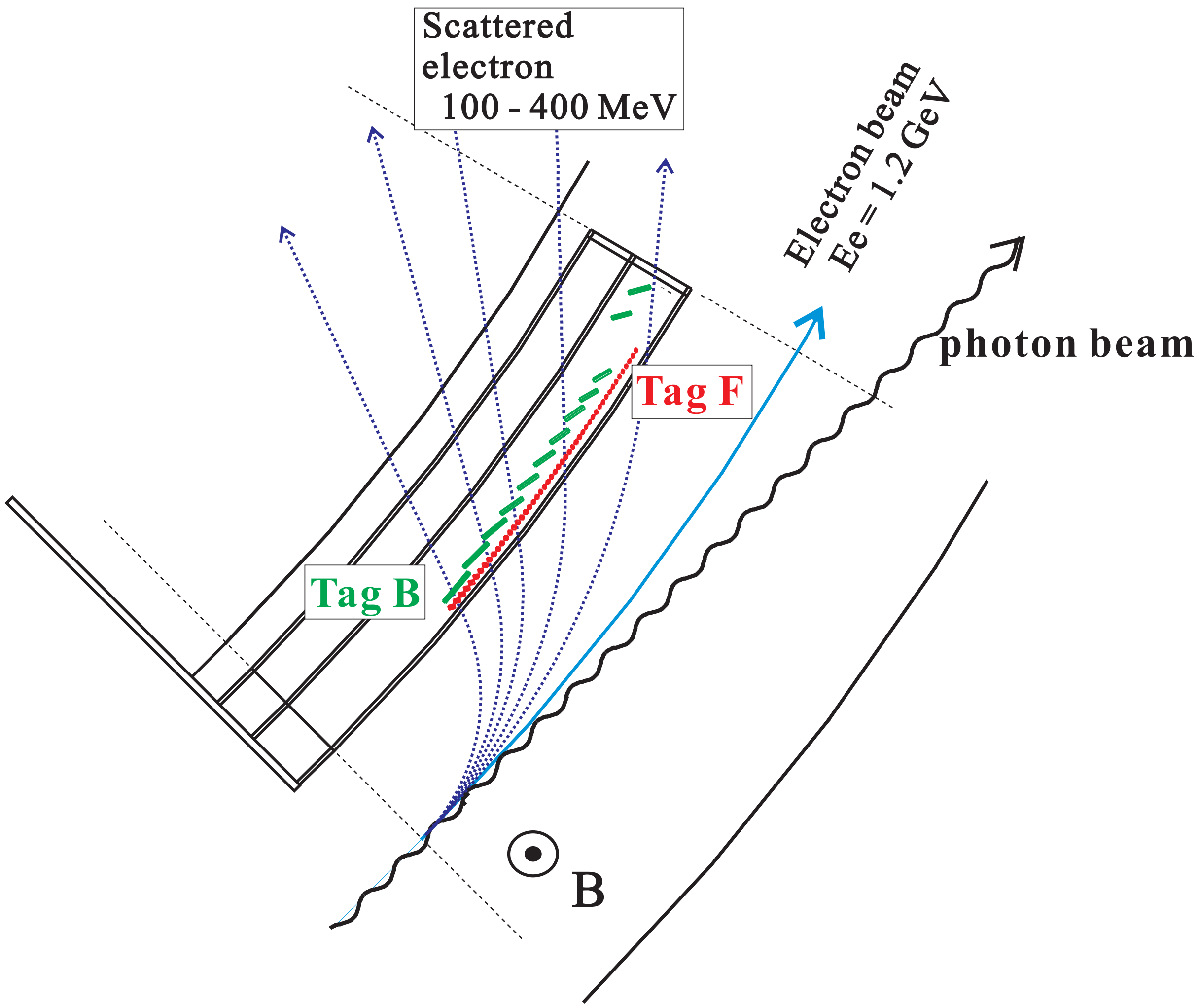

Figure 2.3: *Schematic view of the STB-tagger system. TagF consists of fifty plastic scintillation counters and TagB consists of twelve plastic scintillation counters.*

2.3 Neutral Kaon Spectrometer (NKS)

K^0's were measured with NKS by detecting the $K^0_S \rightarrow \pi^+\pi^-$ decay channel. Previously, NKS was used as a TAGX spectrometer at the Electron Synchrotron of Institute of Nuclear Study, University of Tokyo (INS-ES)[36] and moved to Tohoku University

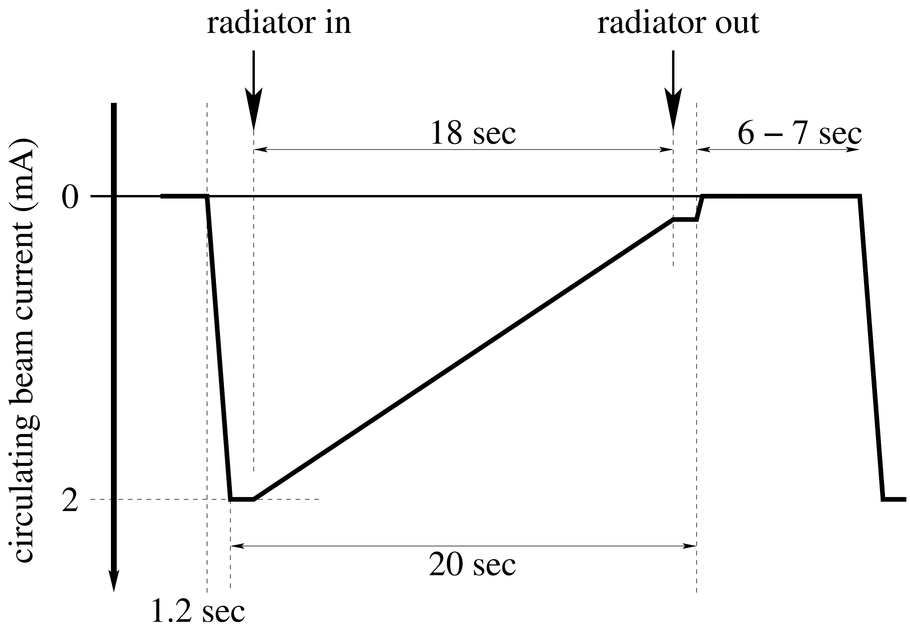

Figure 2.4: *The beam operation cycle of LNS at the present experimental period. Typical intensity of the circulating beam current was adjusted to 2 mA.*

after the shutdown of INS-ES. Figure 2.5 shows the schematic view of NKS and Figure 2.6 shows the detector configuration. The detector configuration was symmetric to the beam line. Therefore, the left and right are defined as shown in Fig. 2.6. The target cell was located in the vacuum chamber at the center of the spectrometer. The Inner plastic scintillator Hodoscope (IH) surrounded the vacuum chamber and acted as a time zero counter. Two types of drift chambers, the straw drift chamber (SDC) and the cylindrical drift chamber (CDC), were located in the magnetic field region for tracking and momentum analysis. The Outer plastic scintillator Hodoscope (OH) surrounded outside of the drift chamber and gave not only the information on time of flight but also the vertical positions of the charged particles. These detectors covered a geometrical acceptance of π sr. K^0's were identified by measuring π^+ and π^- in coincidence with the left and right detector arms.

Because the $\gamma \to e^+e^-$ process caused huge backgrounds in the trigger level, electron veto counters were set on the middle of OH to reject charged particles flying on the horizontal plane along the beam line.

2.3.1 TAGX Magnet

The TAGX magnet was a dipole magnet with a 107 cm diameter and a 60 cm gap. The magnetic field was 0.5 Tesla with 500 A which was the maximum current.

The magnetic field distribution was calculated by the TOSCA program. Figure.2.7 shows the distribution of vertical component of the magnetic field. The strength of magnetic field by TOSCA was found to have about 2 % systematic error by comparison with the measured values at INS-ES and at LNS.

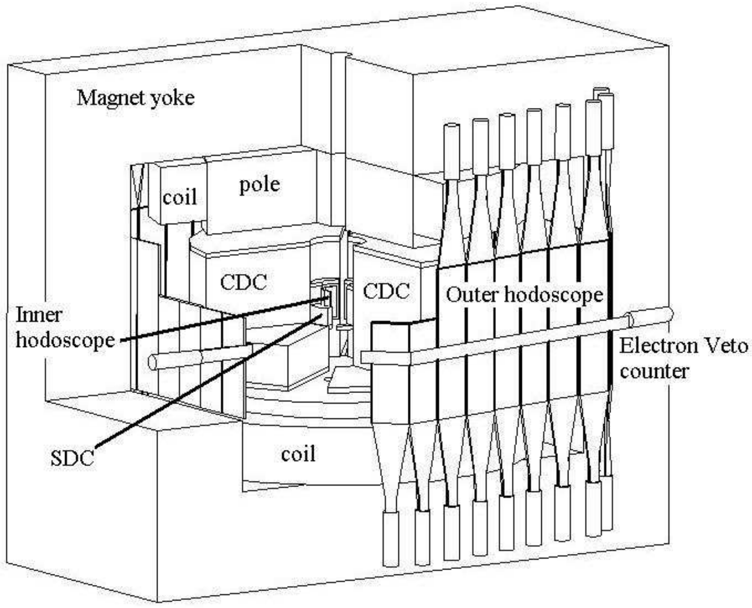

Figure 2.5: *Bird's eyes view of NKS.*

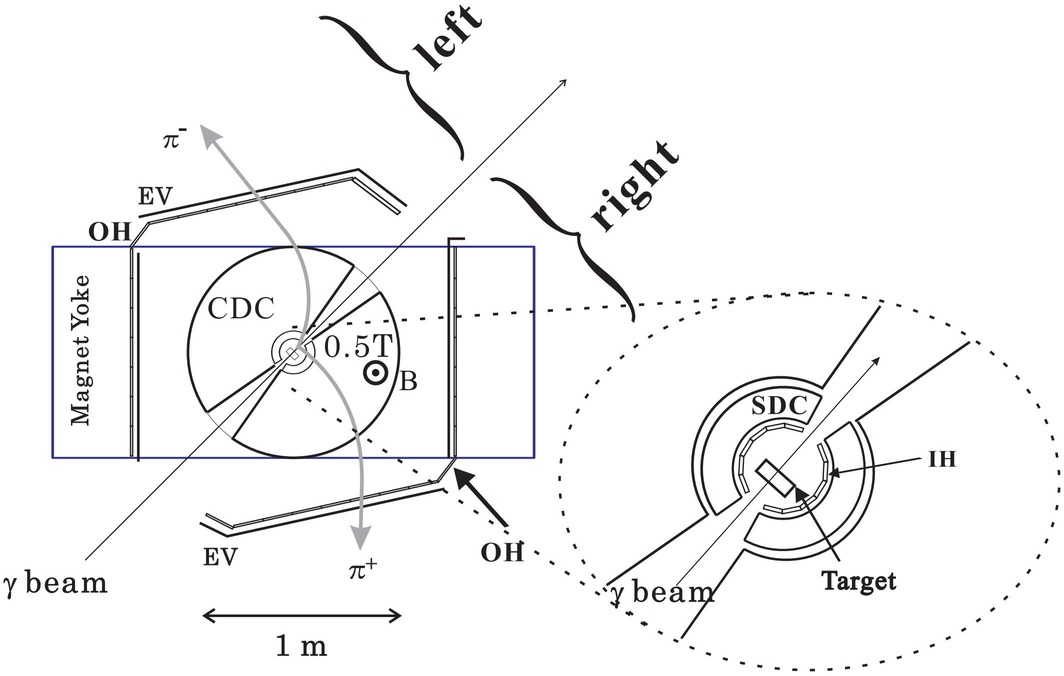

Figure 2.6: *Schematic view of NKS and triggered event. Detectors were positioned almost symmetric along the beam line. Each group is called Left or Right arm as in the figure.*

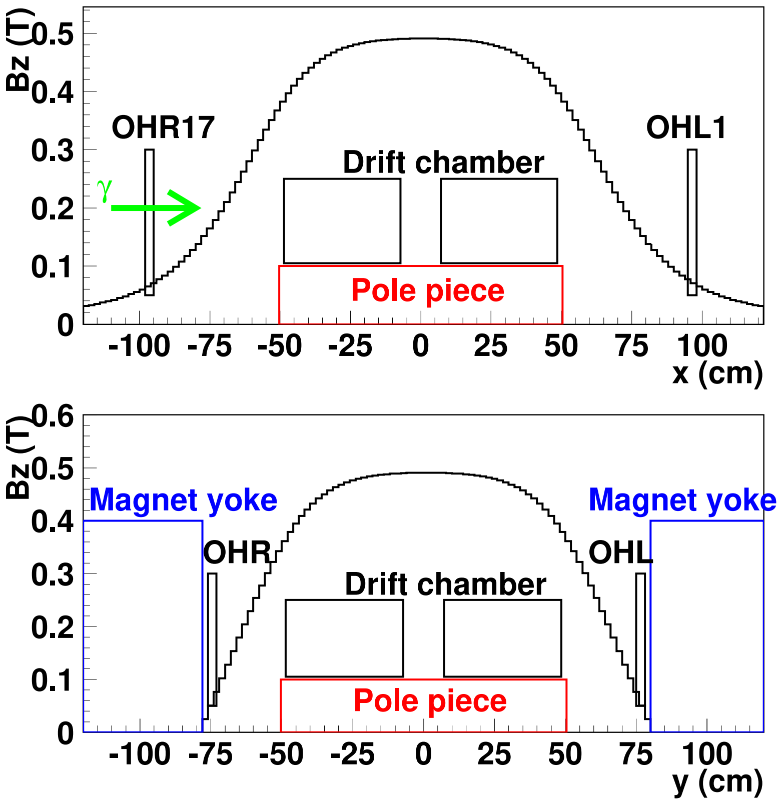

Figure 2.7: *Vertical component of the magnetic field along beam line and along perpendicular to beam line calculated by TOSCA. The radius of pole pieces is 53.5 cm. Positions of chamber, OH, and parts of magnet are drawn in the figure.*

2.3.2 drift chamber

The tracking device of NKS consisted of two types of drift chambers, namely, honeycomb type cylindrical drift chambers (CDC) and straw type cylindrical drift chambers (SDC).

Figure 2.8 shows the structure of these drift chambers. Operation condition is listed in Table 2.2. The signal of the drift chamber was amplified by a pre-amplifiers on the chamber and discriminated by amp-discriminator in the experimental hall.

SDC

SDC was a set of two chambers, which covered the angular ranges from 10 to 170 degrees and the radial ranges from 7.18 to 10.19 cm. The sense wires were made of gold plated tungsten (20 μmϕ), and the straw tubes were made of aluminized mylar film with 180 μm thickness.

SDC included four layers of sense wires.

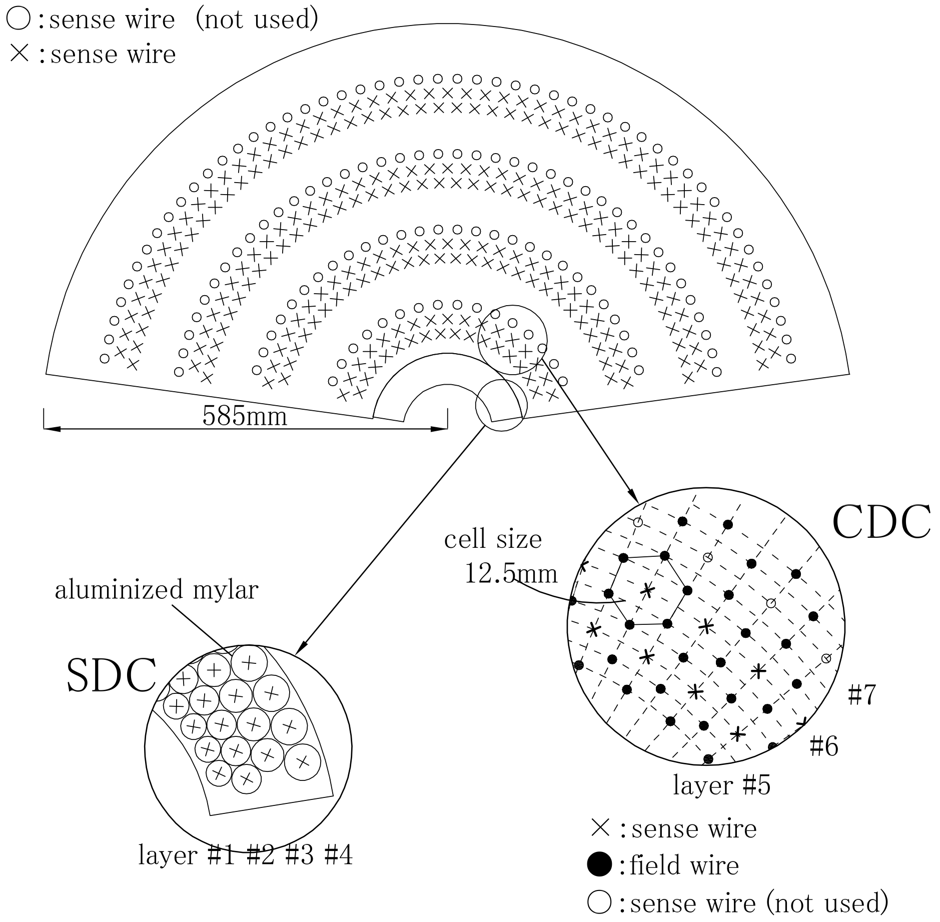

Figure 2.8: *Structure of the drift chambers. The position of sense wires are described.*

CDC

CDC was a set of two honeycomb type drift chambers, which covered the angular ranges from 15 to 165 degrees, and the radial ranges of 13.8 to 48.6 cm.

The geometrical parameters are listed in Table 2.3. The field wires were arranged hexagonally around a sense wire (Fig.2.8). Twelve layers of the sense wires were grouped into four, and each group had three layers. In the present experiment, the third layers of each group were not used. The sense wires were made of gold plated tungsten (30 μmϕ) for the inner two layers and stainless steel for the third layer in each group. The field wires were made of molybdenum (100 μmϕ).

The inner and the outer windows were made of mylar sheet of 200 μm thickness.

Table 2.2: *Operation condition of drift chambers.*

gas mixture	Ar (50%) + C_2H_6 (50%) at STP
high voltage	3000 V for CDC, 1900 V for SDC (typical value)
hit information	horizontal only

Table 2.3: *The design of SDC and CDC.*

Layer No.	straw size (cm)	radius of layers (cm)	#wires (sense)	
1	0.475	7.18	19	
2	0.535	8.07	20	
3	0.600	9.07	19	
4	0.675	10.19	20	
Layer No.	cell size (cm)	radius of layers (cm)	#wires (sense)	
5	1.084 [9.0°]	13.8	16	
6	1.249 [9.0°]	15.9	17	
7	1.414 [9.0°]	18.0	16	not used
8	1.164 [5.4°]	24.7	28	
9	1.263 [5.4°]	26.8	29	
10	1.362 [5.4°]	28.9	28	not used
11	1.243 [4.0°]	35.6	40	
12	1.316 [4.0°]	37.7	39	
13	1.389 [4.0°]	39.8	40	not used
14	1.299 [3.2°]	46.5	50	
15	1.357 [3.2°]	48.6	49	
16	1.416 [3.2°]	50.7	50	not used

We assigned the consecutive numbers from 1 to 16 to the layers through SDC and CDC.

2.3.3 Inner hodoscope (IH)

IH was the scintillator hodoscope with 120 mm long and 5 mm thickness, and segmented into six pieces for both left and right parts as shown Fig.2.9 and listed in Table 2.4. The scintillation photons were guided to outside of the magnet by the optical fiber cable and amplified by a 1 inch PMT to avoid the effect of the magnetic field. Because the counting rates were very high, additional high voltages were provided to the last two dynodes to avoid decrease of the gain.

IH was used not only as time of flight counters but also as time zero counters in the trigger. Dynamic range of the energy deposit at IH should be large, from 1 MeV for minimum ionizing particle to 10 MeV for proton of low momentum around 200 MeV/c. The signal of IH was divided into two lines at counting room. One was discriminated by CFD (Constant Fraction Discriminator) to prevent time walk from the large difference of pulse height and used as the trigger signal. The other was discriminated by LED (Leading Edge Discriminator) and sent to TDC for TOF measurement. Time walk was

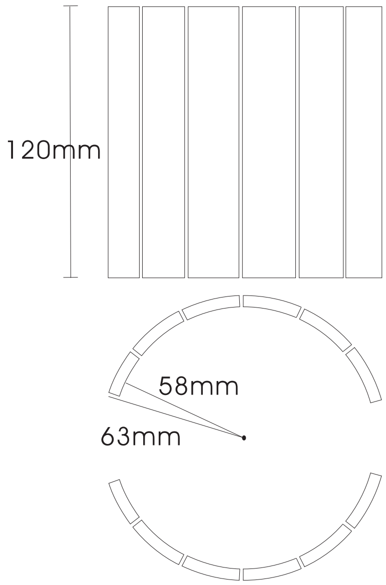

Figure 2.9: *Schematic view of IH.*

corrected in the offline analysis as described in Sect. 3.2.

2.3.4 Outer hodoscope (OH)

OH was the scintillator hodoscope which was segmented into seventeen pieces at both left and right side, where two PMTs were mounted at both ends of each counter, as described in Fig. 2.5 and listed in Table 2.4. The sizes were about 600 mm in height ,10 mm in thickness, and typically 150 mm in width. For the OH in the magnet gap, that is from OHL11 to OHL17 and from OHR1 to OHR7, the scintillation photons were guided to outside of the magnet by the fiber cable and amplified by 2 inch PMTs. All the PMTs were shielded by isolated iron cylinders to reduce the effect of magnetic field.

The signals of OH were used to make trigger signal. In analysis, information on the time of flight was obtained from time-walk-corrected TDC of IH and OH, and the vertical position of charged particle was evaluated by the time difference of the signals from up- and downside PMTs.

2.3.5 Electron veto counter (EV)

EV was the scintillation counter and set to suppress the background from the $\gamma \to e^+e^-$ process in the trigger level. They covered vertically $\pm$ 2.5 cm to the horizontal plane involving beam line at OHs positions. The geometrical acceptance was reduced by about 8 %.

Table 2.4: *List of the counters.*

counter	size	number	reading way
IH		left×6, right×6	PMT on a side
(IHL1-5)	$120^h \times 50^t \times 25^w$ (mm^3)		fiber cable
(IHR1-5)	$120^h \times 50^t \times 25^w$ (mm^3)		fiber cable
(IHL6,IHR6)	$120^h \times 50^t \times 20^w$ (mm^3)		fiber cable
OH		left×17, right×17	2 PMTs on both side
(OHL1)	$600^h \times 10^t \times 170^w$ (mm^3)		acrylic light guide
(OHL2)	$600^h \times 10^t \times 130^w$ (mm^3)		acrylic light guide
(OHL3-9)	$600^h \times 10^t \times 150^w$ (mm^3)		acrylic light guide
(OHL10)	$600^h \times 10^t \times 230^w$ (mm^3)		acrylic light guide
(OHL11-17)	$600^h \times 10^t \times 150^w$ (mm^3)		fiber cable
(OHR1-7)	$600^h \times 10^t \times 150^w$ (mm^3)		fiber cable
(OHR8-17)	$600^h \times 10^t \times 150^w$ (mm^3)		acrylic light guide
EV		left×2, right×2	PMT on a side
EVLF	$50^h \times 10^t \times 125^w$ (mm^3)	1	acrylic light guide
EVLB	$50^h \times 10^t \times 105^w$ (mm^3)	1	acrylic light guide
EVRF	$50^h \times 10^t \times 105^w$ (mm^3)	1	acrylic light guide
EVRD	$50^h \times 10^t \times 115^w$ (mm^3)	1	acrylic light guide

2.3.6 Sweep magnet

In order to suppress the serious background from the e^+e^- pair creation, a sweep magnet was placed between the radiator and NKS. The sweep magnet was a dipole magnet and the magnetic field was about 1.1 Tesla with 300 A. Furthermore, the helium bags were installed at the space from the sweep magnet to the front of the target. Besides, to remove the beam halo, a collimator was arranged just in front of the sweep magnet. The collimator was made of lead, and its hole was 1.0 cm in diameter and 30 cm in length. Although the materials in upstream were less than those at the target, the e^+e^- generated in upstream met the trigger condition easily. Hence, the materials in upstream had to be as small as possible so as to suppress the background in the trigger level. On the other hand, the e^+e^- generated at the target caused the large singles rates on each detectors. Thus, the conditions of the trigger rate and operation of the detectors, especially drift chambers, limited the beam intensity.

2.4 Liquid deuterium target

We used a liquid deuterium target in order to investigate the elementary process of the photo-production of neutral kaon on a neutron.

The target system which was able to control the liquefaction of deuterium and kept the liquid state was adapted to NKS. The target system was designed so as to maximize the yield of K^0, minimize the background and allow safe operation. For the yield of K^0, the target thickness was optimized to be 3.0 cm by the simulation. For the suprresion of the background, the amount of material around the target had to be reduced. Concerning the safe operation, the system was controlled remotely by LabVIEW program running on a Linux machine in the experimental hall, and we could operate and monitor it from the counting room via network.

The temperature around a liquid target and the pressure of the residual gas were monitored all through the period of experiment, and the density of the target was estimated with small ambiguities.

2.4.1 Design of a deuterium target system

The outline figure of the target system is shown in Fig. 2.10. Although the target cell was placed at the center of NKS, the refrigerator should be placed outside of the magnet because the space around the target was quite limited. The long cylindrical part of the cryostat was inserted in the vertical hole with an inner diameter of 120 mm at the center of the yoke and the pole of TAGX magnet. At the top of the cryostat, 2-Stage Gifford-McMahon refrigerator (Sumitomo Heavy Industry RD-208B) was placed. The ultimate temperature of the first and the second stage were measured as 9.2 K and 38.1 K, respectively, in the manufacturer's examination. The cooling powers of two stages were 20 W at 50 K and 8 W at 20 K, respectively. At the second stage of the refrigerator, an oxygen-free copper rod was attached to extend the stage to the center of NKS. Two heat exchangers, a condenser and a re-condenser, were located at the end of the copper rod. The deuterium was liquefied at the condenser and then dropped into the target cell. The re-condenser worked to liquefy the evaporated deuterium from the cell. The refrigeration power of the first stage was also used to cool the thermal shield made of aluminum alloy. The heat transfer to the radiation shield was estimated to be 3.7 W in the condition that the surrounding temperature was 300 K, the temperature of the shield was 50 K, and the vacuum of the cryostat was 1.8×10^{-3} Pa. The heat transfer to the copper rod was 0.6 W when the temperature of the rod was 18 K in the above condition.

2.4.2 Target cell

The cell in which the liquid deuterium was accumulated is shown in Fig.2.11. The holder was made of aluminum with 1mm thickness and the windows on the beam line were made of mylar film with 75μm thickness in order to reduce the background from e^+e^- pair creation and the effect of the multiple scattering of charged particles. More importantly, the events generated at the target window can not be distinguished from those in the liquid deuterium in analysis. Although the background events from the upstream window was considered to be small, the contribution from both windows were estimated as the systematic error for the number of the target (Sect. 3.10.3). The inside diameter of open parts of the target cell was 40 mm, which was determined from the beam size of about 5 mm in σ and the fluctuation of the beam spot position less than 5 mm.

When the cell was filled with the liquid deuterium, the mylar windows expanded due to the pressure. Its effect was estimated from the data analysis and calculated by a

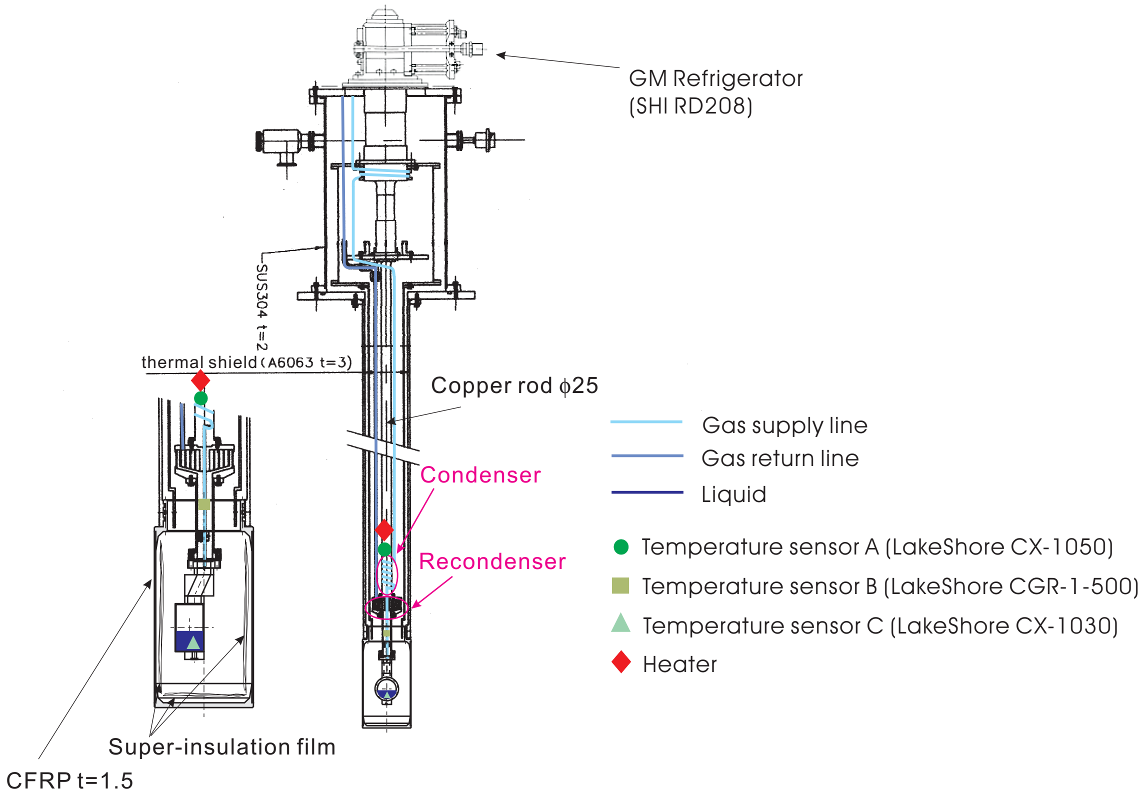

Figure 2.10: *Schematic view of the target system.*

finite element method, then the expansion was found to be about 2 mm for both side windows. Therefore the target width was evaluated to be 34 $\pm$ 2 mm along the beam line.

2.4.3 Equipment

A 50 W heater and a temperature sensor (sensor A in Fig. 2.10) were placed on the copper rod. The temperature was controlled by feeding back the measured value by the sensor to the heater. Two more temperature sensors (B, C) were placed to measure the temperature of the gas and the liquid directly. The sensor (B) was placed on the pipe between the re-condenser and the target cell. The other one (C) was placed in the cell as shown in Fig. 2.11. These temperature sensors had low sensitivity to the magnetic field and high resistance to ionizing radiations.

The temperature of the liquid deuterium was kept to be 19 $\pm$ 0.1 K during the data taking. The pressure of the residual gas was about 50 $\pm$ 2 kPa. The density of the liquid deuterium target was evaluated from the temperature and the pressure by rule of thumb. The density was estimated to be typically 0.17 g/cm^3. The amount of the target deuteron was calculated in Sect.3.10.3.

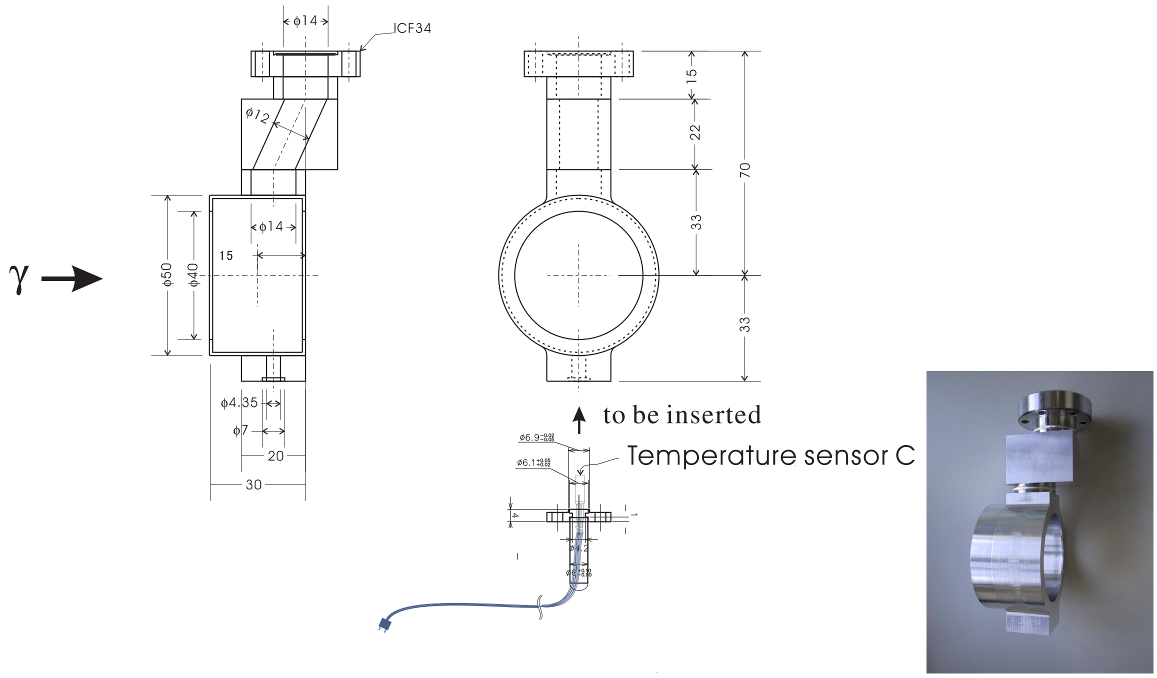

Figure 2.11: *The target cell.*

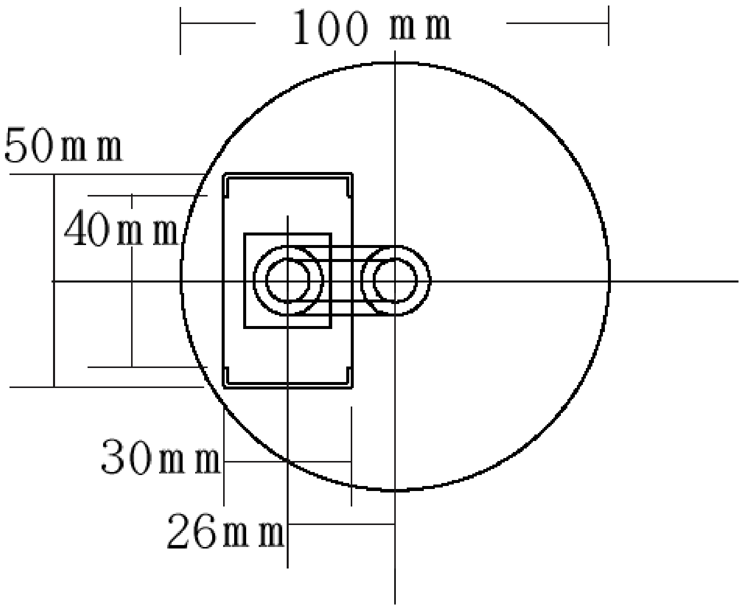

Figure 2.12: *Size and position of the target cell in the vacuum chamber.*

2.5 Data acquisition (DAQ) system

2.5.1 Setup

Since the counting house was located on the ground far from the experimental hall, analog signals from the detectors were sent through 50∼100 m cables.

The signals of IH, OH and EV were discriminated in the counting house to make triggers or to measure TDC. These signals were sent through 50∼60 m cables. For IH, the signal was divided before digitization and sent to ADC. For OH and EV, the signal was divided at the PMT into TDC and ADC lines in the experimental hall and one was sent to ADC module through 100 m long cable.

On the other hand, tagger signals were discriminated and used to make a coincidence between TagF and TagB in the experimental hall. We could change the coincidence mode ON/OFF by relay switch from the counting house. Figure 2.15 shows the tagger trigger logic. Thus, the logic signal of TagF was sent to TDC in the counting house. The logic and analog signals of TagB were sent to TDC and ADC, respectively. Besides, in order to count the number of photons, the logic signals of TagF, TagB and SUM which was defined as Fig. 2.15 were sent to CAMAC scalers. Scaler data were read at the end of each spill.

Figure 2.13 shows a diagram of the data acquisition system. The system was operated synchronously to the accelerator cycle. The data for IH,OH,EV and tagger were fed into the TDC and ADC modules of the TKO or CAMAC. The data in TKO were then stored in a VME memory module (SMP). The SMP had a dual memory and exchanged the roles of storing and reading event by event to take data efficiently.

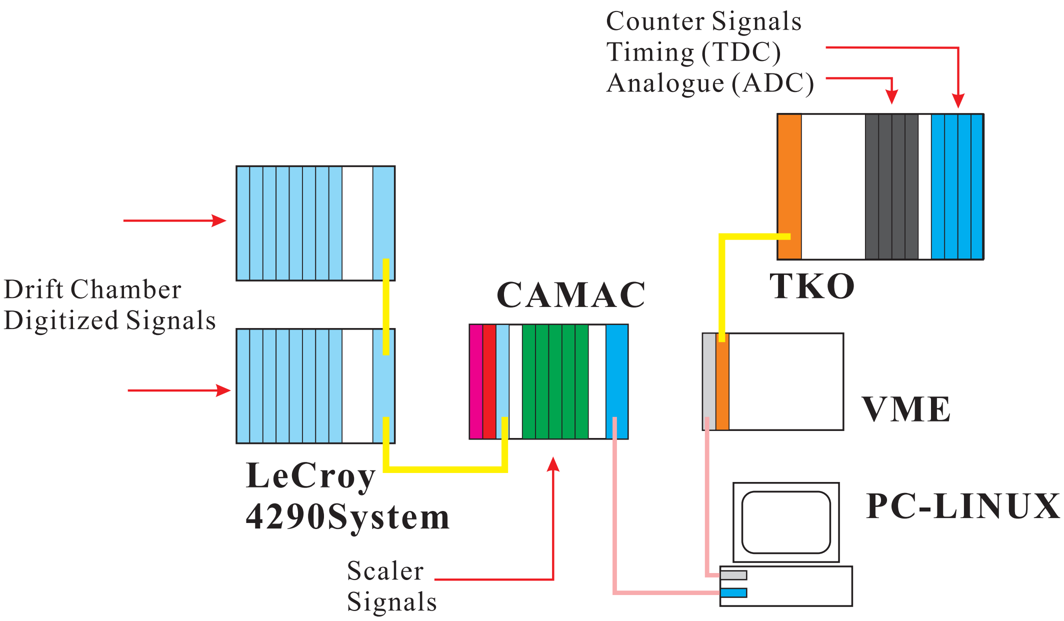

Figure 2.13: *Data acquisition system.*

2.5.2 Trigger logic

The trigger conditions of this experiment are shown in Table 2.5, and the trigger logic is shown in Fig.2.14.

The main trigger (MT) logic was generated of 3 parts.

$$MT = LEFT \otimes RIGHT \otimes BEAM$$

.

BEAM : Photons were generated in the energy region of 0.8 to 1.1 GeV and charged particles passed IH.

LEFT or RIGHT : More than one charged particles passed through IH and OH in the Left and Right arms, respectively.

To reject the e^+e^- background events, the electron veto counters were required for both Left and Right triggers.

Table 2.5: *Trigger logic.*

MainTrigger	MT = LEFT $\otimes$ RIGHT $\otimes$ Beam
Left Trigger	LEFT = IHL $\otimes$ OHLU $\otimes$ OHLD $\otimes$ $\overline{\text{EVL}}$
Right Trigger	RIGHT = IHR $\otimes$ OHRU $\otimes$ OHRD $\otimes$ $\overline{\text{EVR}}$
Beam Trigger	BEAM = (IHL$\otimes$IHR$\otimes$SUM)
Tagger Trigger (B: Backup Counter) (F: Finger Counter)	TagB = TagB1 $\oplus \cdots \oplus$ TagB12 SUM1 = TagB1 $\otimes$ (TagF1 $\oplus \cdots \oplus$ TagF4) SUM = SUM1 $\oplus \cdots \oplus$ SUM12
Left Side Trigger (U: up, D: down)	IHL = IHL1 $\oplus \cdots \oplus$ IHL6 OHLU = OHLU1 $\oplus \cdots \oplus$ OHLU17 OHLD = OHLD1 $\oplus \cdots \oplus$ OHLD17 EVL = EVLF $\oplus$ EVLB
Right Side Trigger	IHR = IHR1 $\oplus \cdots \oplus$ IHR6 OHRU = OHRU1 $\oplus \cdots \oplus$ OHRU17 OHRD = OHRD1 $\oplus \cdots \oplus$ OHRD17 EVR = EVRF $\oplus$ EVRB

For tagger calibration runs, only the Tagger Trigger was used as the main trigger. This trigger was not biased by conditions in the NKS side.

2.6 Data summary

The experiments were carried out in September, November, December in 2003 and April, May, June in 2004. Each period was about 2 or 3 weeks. The duty factor was about 60 % with 20 seconds of flat top time as shown in Fig.2.4. The radiator was inserted for 18 seconds. The intensity of the beam was from 2 to 3 MHz in the region from 0.8 to 1.1 GeV photon energy.

Table 2.6 and 2.7 summarize the conditions of the data taking.

In this thesis, the data on the hydrogen target taken in June 2004 is not discussed.

The tagging efficiency run was for the estimation of the transmission rate of the photons from the radiator to the target. The tagger run was for the estimation of the analysis efficiency of tagger counter. These are discussed in Sect. 3.10.2.

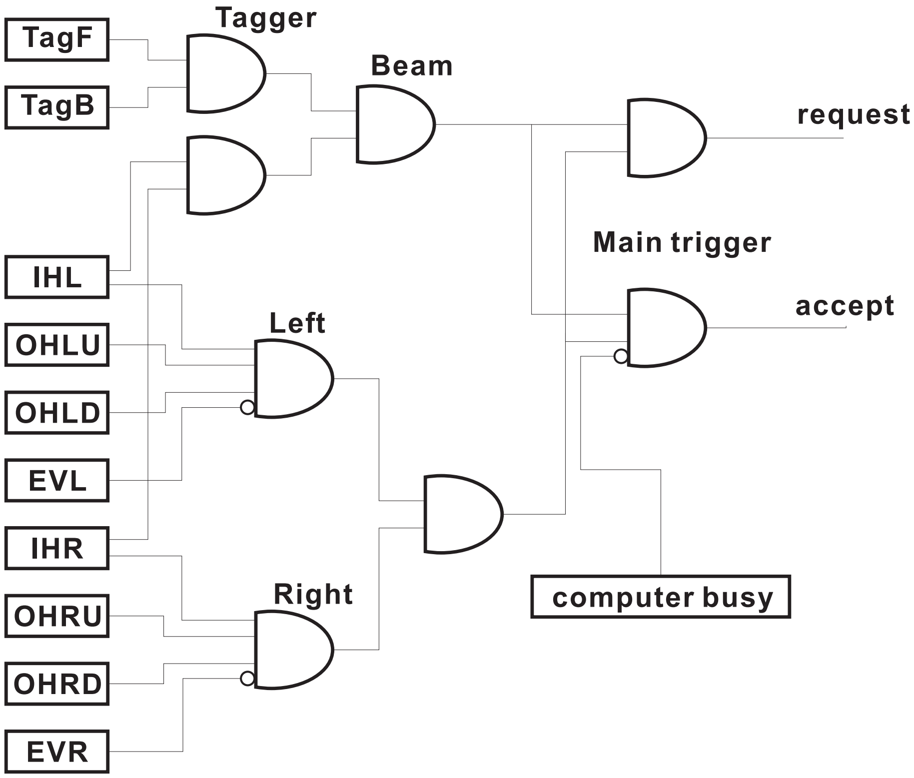

Figure 2.14: *Schematic view of the trigger logic.*

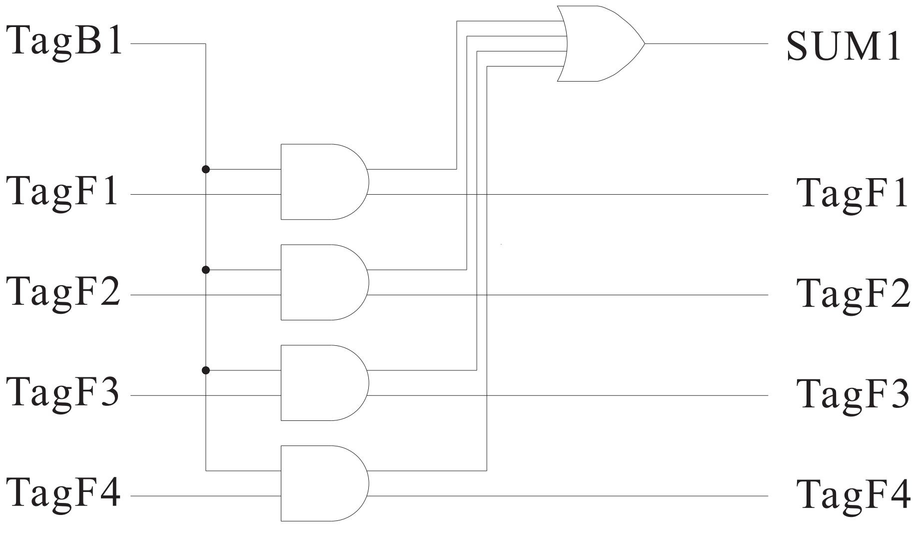

Figure 2.15: *Schematic view of the trigger logic for the tagger. The output signals are sent to TDC and scaler.*

Table 2.6: *Data summary for the normal data taking for each experimental period.*

period		target	#spill	#photon	typical photon intensity (MHz)
	1st	liq. D_2	9.7×10^3	5.6×10^{11}	1.5
September	2nd	empty	2.1×10^3	7.5×10^{10}	1.7
	3rd	liq. D_2	6.3×10^3	3.2×10^{11}	2.6
November		liq. D_2	2.7×10^4	8.5×10^{11}	1.7
December		liq. D_2	1.6×10^4	5.4×10^{11}	1.8
April		liq. D_2	1.9×10^4	7.4×10^{11}	2.2
May		liq. D_2	3.9×10^4	1.6×10^{12}	2.3
June		liq. H_2	2.9×10^4	1.2×10^{12}	2.3

Table 2.7: *Data summary of tagger trigger runs.*

period	run name	#photon
September	tagging efficiency	2.4×10^6 (by CsI)
	tagger	1.8×10^9
November	tagging efficiency	4.8×10^6 (by CsI)
		1.9×10^9 (by Lead Glass)
	tagger	5.6×10^9
December	tagging efficiency	1.2×10^8 (by Lead Glass)
	tagger	3.2×10^9
April	tagging efficiency	1.9×10^8 (by Lead Glass)
	tagger	4.1×10^9
May	tagging efficiency	5.7×10^7 (by Lead Glass)
	tagger	7.6×10^9
June	tagging efficiency	1.6×10^7 (by Lead Glass)
	tagger	1.9×10^{10}

Chapter 3

Analysis

3.1 Outline

The goal of the analysis in the present experiment is to obtain the differential cross section of K^0 photoproduction and compare it with theoretical calculations. In this chapter, those procedures are described.

We measured events in which at least two charged particles were detected by NKS. The invariant mass of K^0 is calculated as the following formula,

$$M(\pi^+\pi^-)^2 = \left(\sqrt{\vec{p}_{\pi^+}{}^2 + m_{\pi^+}^2} + \sqrt{\vec{p}_{\pi^-}{}^2 + m_{\pi^-}^2}\right)^2 - (\vec{p}_{\pi^+} + \vec{p}_{\pi^-})^2,$$

where $\vec{p}$ is a 3-momentum and m_π is a mass of pion, respectively.

The momenta of the charged particles were calculated from the curvature of tracks, and the particle velocities were calculated from the length of the tracks and time of flight between IH and OH.

In sect. 3.2, the way of calibration for the hodoscope, (IH, OH) and the tagger counters are explained, and performances of the hodoscope are shown.

Calibration and performance of drift chambers are shown in Sect. 3.4. Simultaneously, tracking method and momentum reconstruction are explained. The ways to suppress the background are explained in Sect. 3.5, 3.6 and 3.7. Evaluating various efficiencies and calculating the cross sections are described in Sect. 3.10.

3.2 Calibration of hodoscope

For IH, OH and TagB, which have ADC data, the time measured by TDC were corrected by pulse height as

$$T_{cor} = T_{raw} - \frac{p_0}{Q - p_1} + p_2$$

where Q, T_{raw} are ADC and TDC data of a hodoscope, p_0, p_1, p_2 are fitting parameters, T_{cor} is corrected time, respectively. Figure 3.1 shows an appearance of the pulse height correction for IHR4. Although IH was used as a time zero counter in the trigger

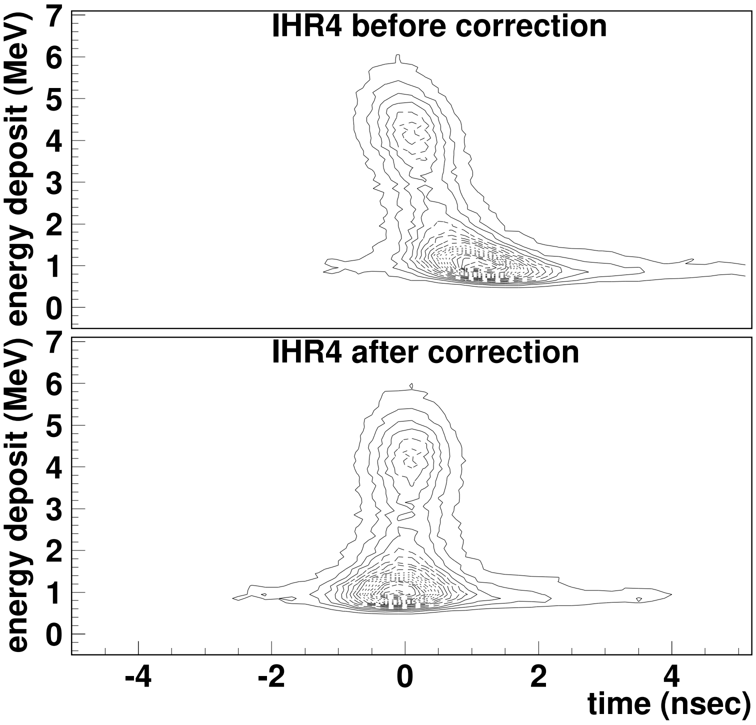

Figure 3.1: *Contour plots of the time v.s. the energy deposit of IHR4. Upper figure is before the correction and lower one is after. Due to the position of IHR4, there are two peaks at 1 MeV and 4 MeV. The former is that the particles generated near the target passed through IHR4 from the inside to the outside, on the other hand, the latter is that the particles generated in upstream passed across IHR4.*

level, relative difference of the timing among IH existed within 1 nsec. Therefore, time difference between each IH and each tagF or tagB were adjusted to be 0 nsec run by run in the analysis. Figure 3.2 shows the time difference distribution between IH and TagF when the multiplicity of TagF is 1. The time of IH was the mean value of the time of IHL and IHR. Details of analysis for tagger are described in Sect. 3.3.

The peak at 0 nsec is true coincidence, and others with 2 nsec cycle are accidental coincidence which is caused by the beam bunch. The time resolution is derived to be 410 psec in rms.

Figure 3.3 shows the time difference between IHL and IHR when the particles tracks can be reconstructed and are identified as pions (see Sect. 3.5). Fitting by the gaussian, the time resolution is estimated about 660 psec in rms. Therefore, it was found that the time resolution of IH was $660/\sqrt{2} \sim 470$ psec and that of tagF was $\sqrt{410^2 - (660/2)^2} \sim$ 240 psec.

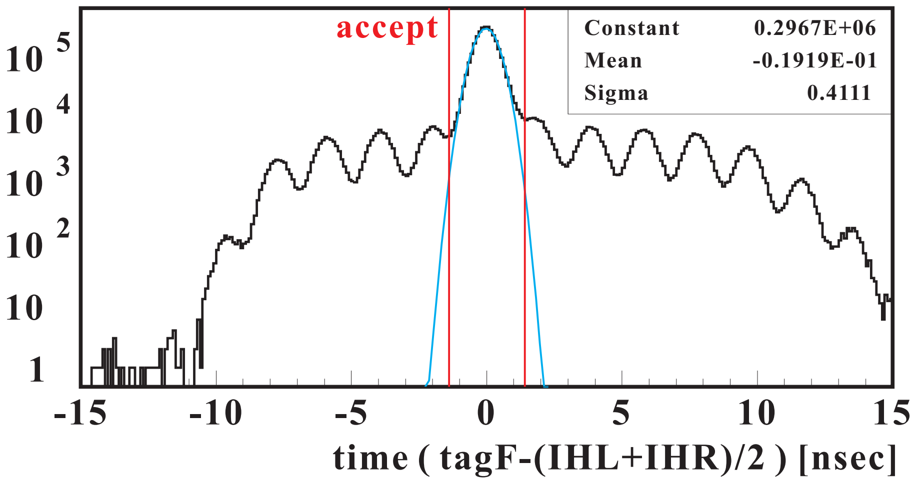

Figure 3.2: *Time difference between IH and tagger. The beam bunch structure of 2 nsec can be seen. The time resolution was derived to be 410 psec in rms*

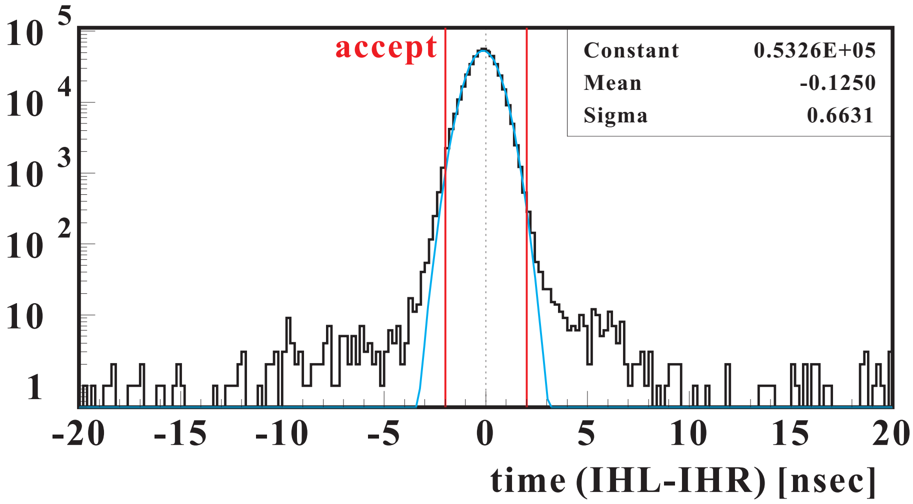

Figure 3.3: *Time difference between IHL and IHR. The time resolution was derived to 660 psec in rms*

We required the time gates for these time difference distributions, $\pm$ 1.3 nsec for IH-tagger and $\pm$ 2.0 nsec for IHL-IHR, respectively. The width of these gates correspond to about 3 σ.

In the case of OH, the time difference between the up and down PMT's gives the information of the vertical position of the track, namely,

$$z_{OH} = v \cdot (T_{down} - T_{up})/2,$$

where T_{up} and T_{down} are corrected times at the up and down PMT's, and v is the propagation velocity of the scintillation light.

Figure 3.4 shows the vertical distribution at OHR1 when pions are selected. The dent at z=0 is due to EV. The length of OH is 60 cm, and the width of EV is 5 cm.

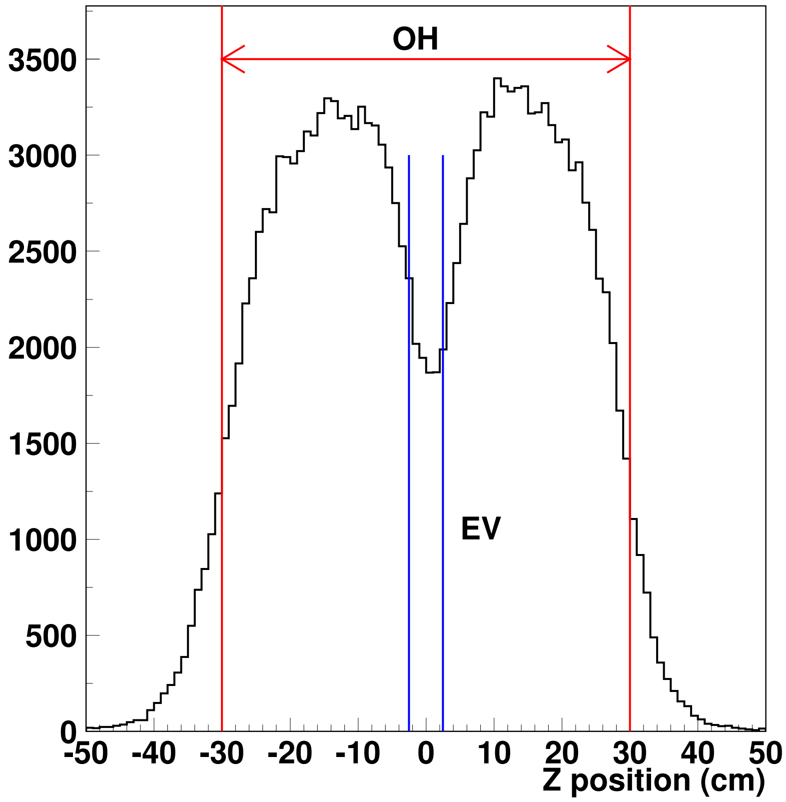

Figure 3.4: *Distribution of vertical position at OH (from OHL3 to OHL9) calculated from time difference between up and down PMT's signals for pions. The hight of these OHs are 30 cm and of EV is 5 cm as shown in the figure.*

Moreover, time of flight was derived from the time difference between the mean times for the up and down PMT's of OH to IH. The offset of mean time of OH was adjusted using the trajectory information on the particles to give time of flight correctly. Figure 3.5 shows the resolution of time of flight estimated from track information and the hodoscope information, that is the trajectory length fl and the time difference between OH and IH ft_{diff},

$$TOF_{rel} = fl/c - ft_{diff}$$

for e^+/e^- events. Although the tail due to slow particle existed, the resolution was found to be 510 psec. Therefore, the time resolution of one of PMTs mounted on OH was about 280 psec. The position resolution of OH was estimated to be about 4 cm, it was consistent to FIg. 3.4.

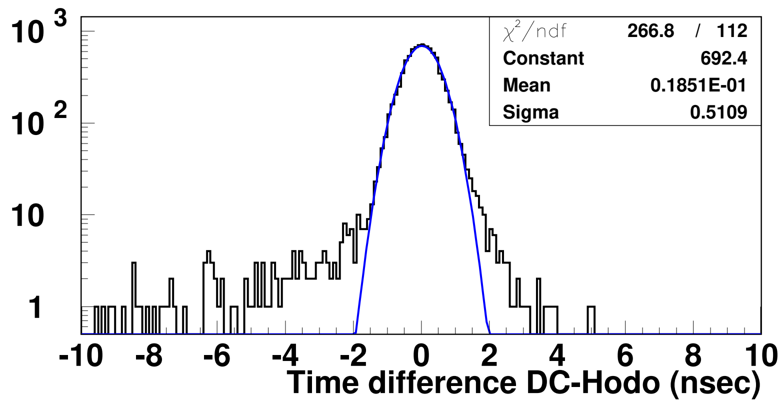

Figure 3.5: *The difference of time of flight estimated from the track information and the hodoscope information.*

3.3 Calibration of tagger

3.3.1 Clustering and timing gate

The tagger gives us the information on the photon energy and the number of photons. In this section, the way how the accidental hits are removed and the clusters are decided is explained.

Figure 3.6 shows the hit pattern of TagF. The structures around TagF15 and TagF45 come from support frames of the window of vacuum chamber of STB-ring, where some parts of electrons lose its energy and are scattered. These effects were well reproduced and understood by a Geant4 simulation.

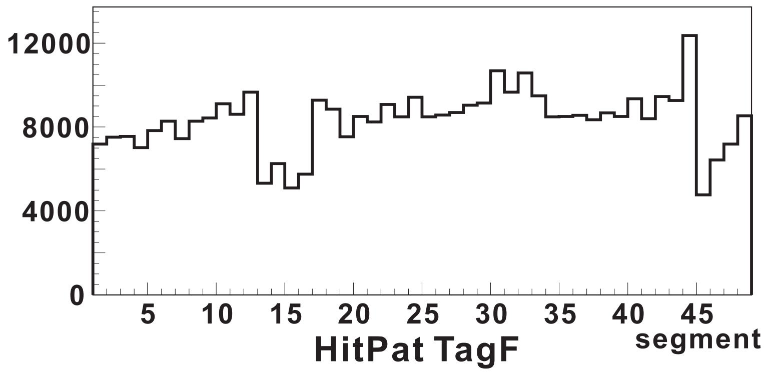

Figure 3.6: *Tagger hit pattern from the number of TDC hits.*

Figure 3.7 shows the time difference between TagF and TagB. Because the pulse height correction is applied only to TagB as mentioned in Sect. 3.2, the shape of the time difference is not symmetric. However, the time gate of |time diff| < 2 nsec was applied because the tail was small.

Next, relative timings among each TagF segment were adjusted using time difference between IH and TagF which was gated to remove the accidental hits as mentioned in Sect. 3.2

Finally, TagF hits were collected in clusters. A cluster was identified as TagF hits in serial segments in the same timing in coincidence with corresponding TagB. This cluster was defined as TagH, and its segment number and time were derived as the average of associated TagF hits. Figure 3.8 shows the time difference between different TagH in a trigger, in which the condition of the number of TagH is 2. In the lower figure, it was required that the TagB segment of each TagH was separated more than 2 to show the correlation between accidental events, and it was found that TagF had the resolution of $530/\sqrt{2} \sim 370$ psec. The resolution in the upper figure is slightly larger than that in the lower figure. This was caused by accidental hit at TagB.

Then, the time gate of |time diff| < 1.8 nsec was applied.

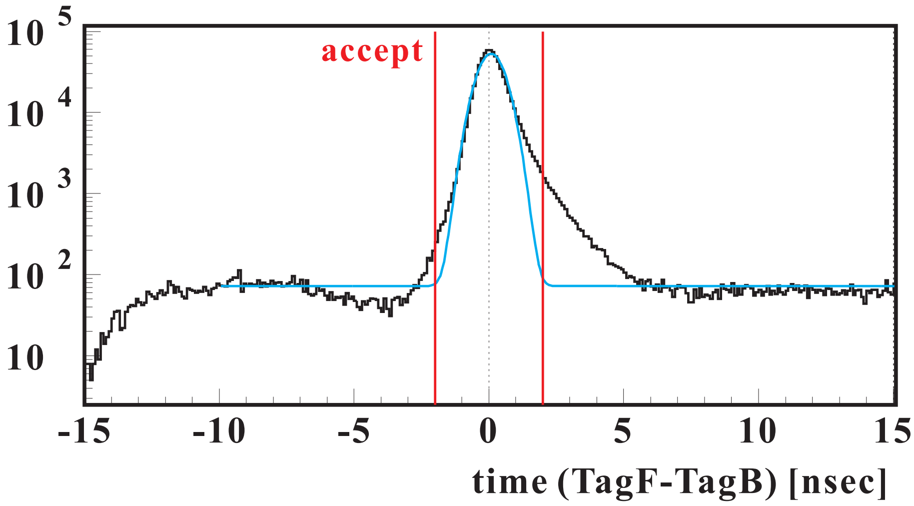

Figure 3.7: *Time difference between TagF and TagB. The multiplicity of TagF is required to be 1.*

3.3.2 Energy calibration

The photon energy was calibrated in July 2004 [34] with the sweep magnet (Sect. 2.3.6) and the tracking drift chamber installed at downstream of the magnet by detecting the e^+e^- created at a copper converter at upstream of the magnet(Fig. 3.9). Figure 3.10 shows the result. The accuracy of energy was measured to be $\pm$ 10 MeV.

However, at the experiment using liquid deuterium, tagger hit pattern was shifted by one segment to low energy side (Fig. 3.11). This causes the systematic error of -6 MeV.

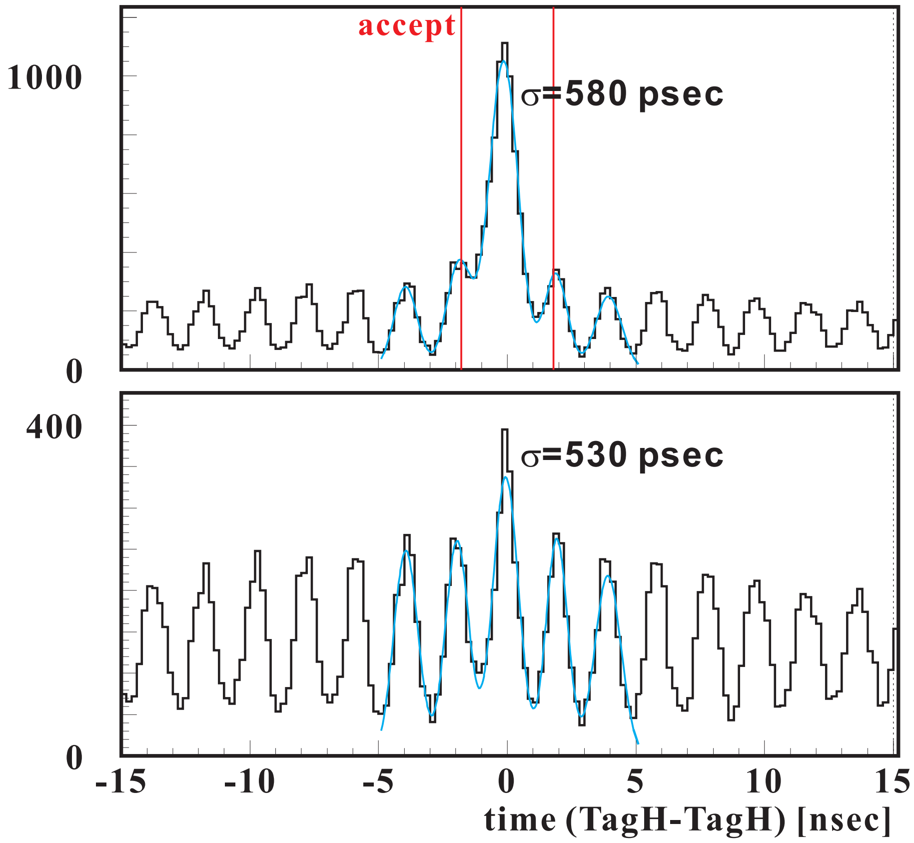

Figure 3.8: *Time difference between different TagH with #TagH=2. The lower figure is required that the TagB segments in TagH are separated more than 2.*

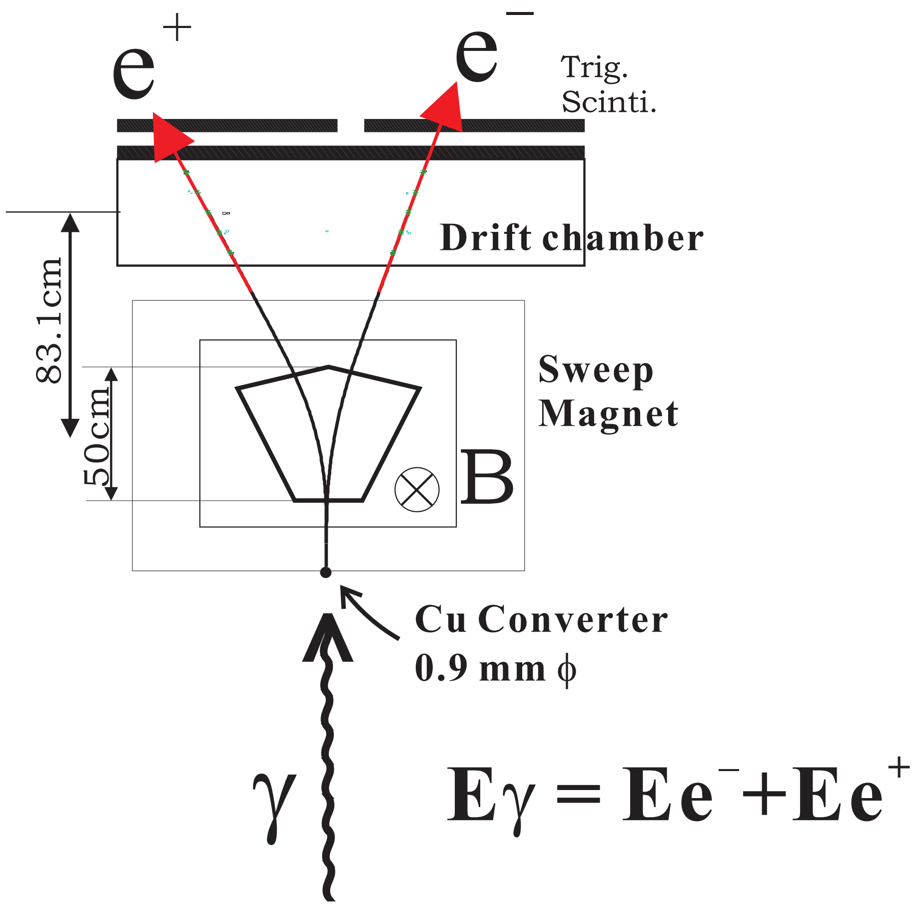

Figure 3.9: *Schematic view of the experiment for the calibration of the photon energy. The e^+e^- converted from γ at Cu converter was measured by a drift chamber. The momentum of the e^+/e^- was calculated using the magnetic field of the sweep magnet, and the photon energy was derived as the sum of the energies of e^+e^- by each tagger segment.*

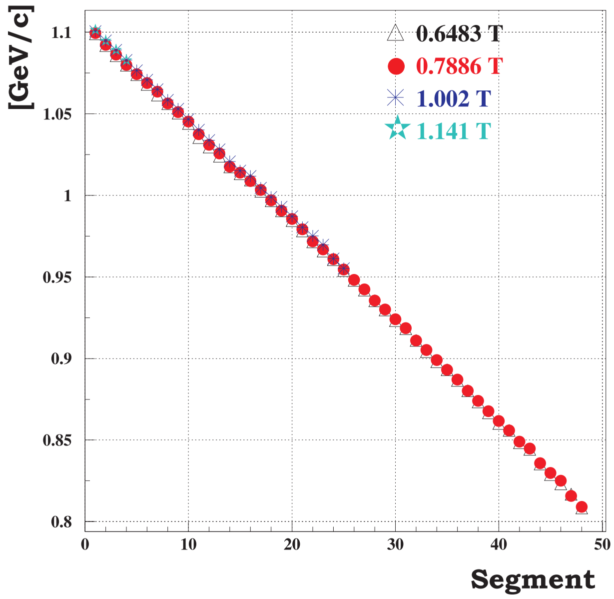

Figure 3.10: *Result of the photon energy calibration. The energy was calibrated via* $\gamma \to e^+e^-$ *conversion with four magnetic fields of spectrometer, in order to measure all the range of the tagged photon energy.*

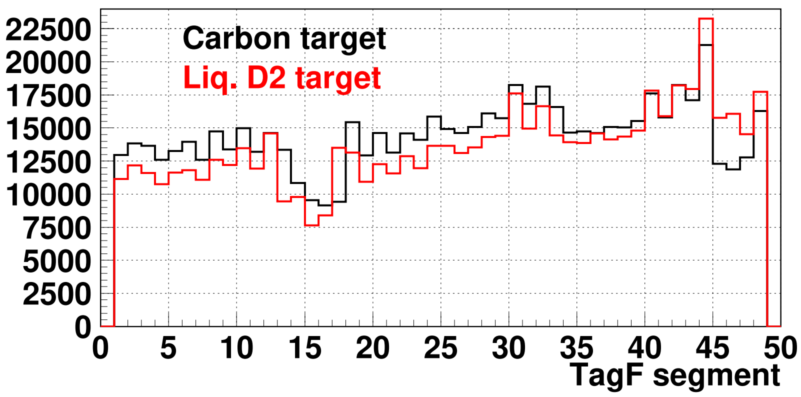

Figure 3.11: *Difference of hit pattern TagF between tagger calibration experiment and the present experiment. The structures around segment 15 and 30 were shifted by one segment. This causes systemtic error on photon energy of* -6 *MeV.*

3.4 Calibration of drift chamber

3.4.1 TDC calibration

The drift chambers play an essential role in this experiment because the momentum of charged particles is obtained from the trajectory in the magnetic field. Furthermore, the vertex point of K^0 decay is reconstructed by extrapolating trajectories of 2 pions.

Due to non-uniformity of the electric field in the drift space, the relation of a drift length and a drift time (x-t relation) is not linear. We assumed that x-t relation was polynomial function of 7th order for CDC and 4th order for SDC. The x-t relations were adjusted run by run. The parameters were decided for each layer. Fig. 3.12 shows x-t relation for two layers in SDC and CDC, respectively, at a certain run.

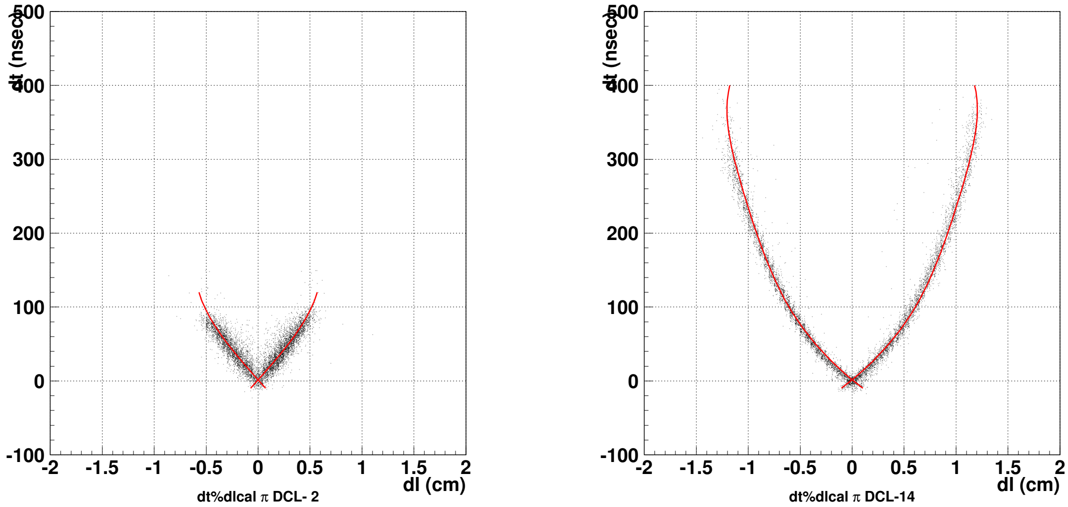

Figure 3.12: *x-t relation of SDC layer 2 (left) and CDC layer 14 (right)*

3.4.2 Tracking

Pre-selection before tracking

The procedure of pre-selections before tracking analysis is presented in this section.

First, a selection by maximum number of hits in each layer (MLH) was applied. Figure 3.13 shows MLH distribution for Layer 1 and 14 in both sides.

Most events with a large MLH are caused by electromagnetic background processes and take a long time for searching tracks due to a large number of combinations of hits. Therefore, those events were rejected to reduce the analyzing time. In the present analysis, the MLH was set at 10.

Next, clusters were made in the following groups,

- SDC (Layer#1-#4),
- CDC1 (Layer#5 and #6),

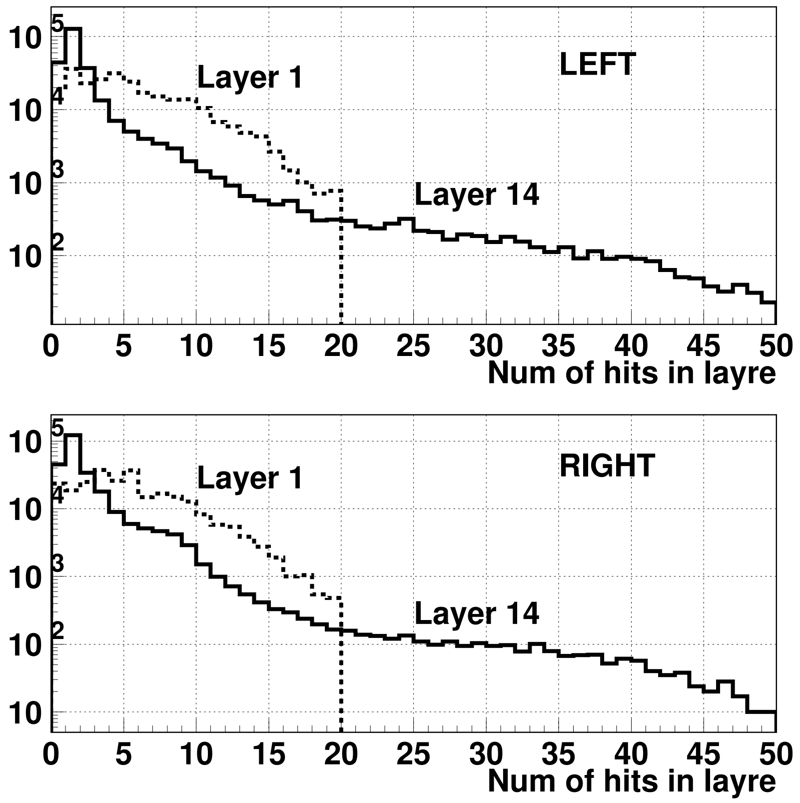

Figure 3.13: *MLH distributions for Layer 1 and 14 in both sides.*

- CDC2 (Layer#8 and #9),
- CDC3 (Layer#11 and #12),
- CDC4 (Layer#14 and #15).

The cluster combined neighboring hits between layers, e.g., (layer# - wire#)=(1-10,2-9,3-10,4-11) in SDC group as shown Fig 3.14. Therefore, the track candidates were made of the clusters in each group under following condition,

- 1 cluster in each group,
- at least 4 groups,
- at least 6 hits in total,
- the selection of the angles between clusters

  ▷ $|\phi_{CDC1} - \phi_{SDC}| < 30^{\circ}$

  ▷ $|\phi_{CDC2} - \phi_{CDC1}| < 15^{\circ}$

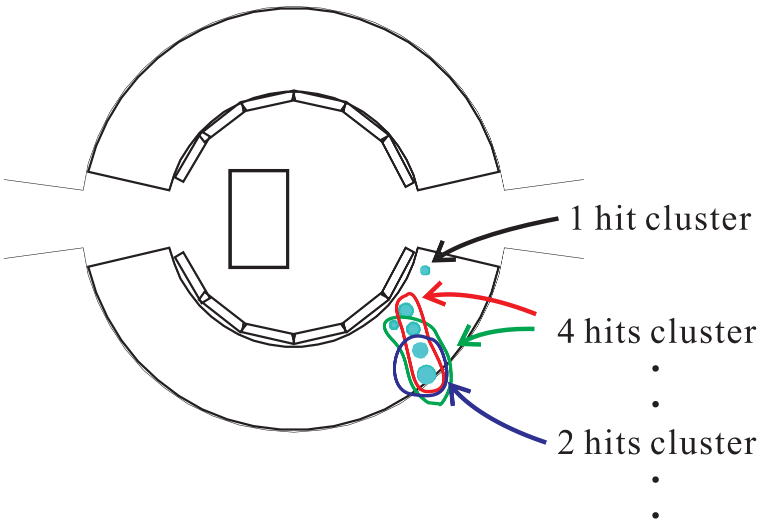

Figure 3.14: *The combination of hits in the clusters. In the case of this figure, 21 clusters are made.*

- ▷ $|\phi_{CDC3} - \phi_{CDC2}| < 15^{\circ}$
- ▷ $|\phi_{CDC4} - \phi_{CDC3}| < 15^{\circ}$

where ϕ is the angle in the horizontal plane against the beam direction.

Tracking of particle trajectory

The trajectory of a charged particle in the magnetic field was calculated by the cubic spline interpolation method [37]. Because the vertical positions in the drift chamber were not measured, fitting was carried out in mid-plane using vertical component of magnetic field at wire positions by least χ^2 method, firstly. Bad tracks ($\chi^2 > 300$) were rejected. After the OH segment corresponding to the track was found, vertical components of the magnetic field off mid-plane were used in re-fitting assuming a trajectory connecting the origin point to the vertical hit position at OH, in which horizontal positions on a track were known by previous fitting. In the latter analysis, a robust fitting method by J.W.Tukey [38] was used, which is a method to find a plausible track in consideration of weights for hits. The weights were changed by the residual calculated in the previous fitting. In these fitting, the momentum of the track was parameterized and obtained from the tracking result.

The trajectory was extrapolated from DC to OH by 4th Runge-Kutta method, in which initial conditions were the position and the derivative at the outermost layer and the momentum obtained from the fitting. In Runge-Kutta method, secondary derivative at each step was calculated using vertical component of magnetic field and initial momentum. The momentum was assumed to be constant. Thus, the nearest OH were searched and labeled to the track. The IH segment corresponding to the track was searched by simple extrapolation of a track. Figure 3.15 shows the residual distribution between a center of IH or OH and the point extrapolated from the track. The typical width of the residual distributions on IH and OH are 2.7 cm and 15 cm, respectively (see Sect. 2.3.3, 2.3.4). The cuts for these distribution are 1.6 cm and 10.0 cm, respectively.

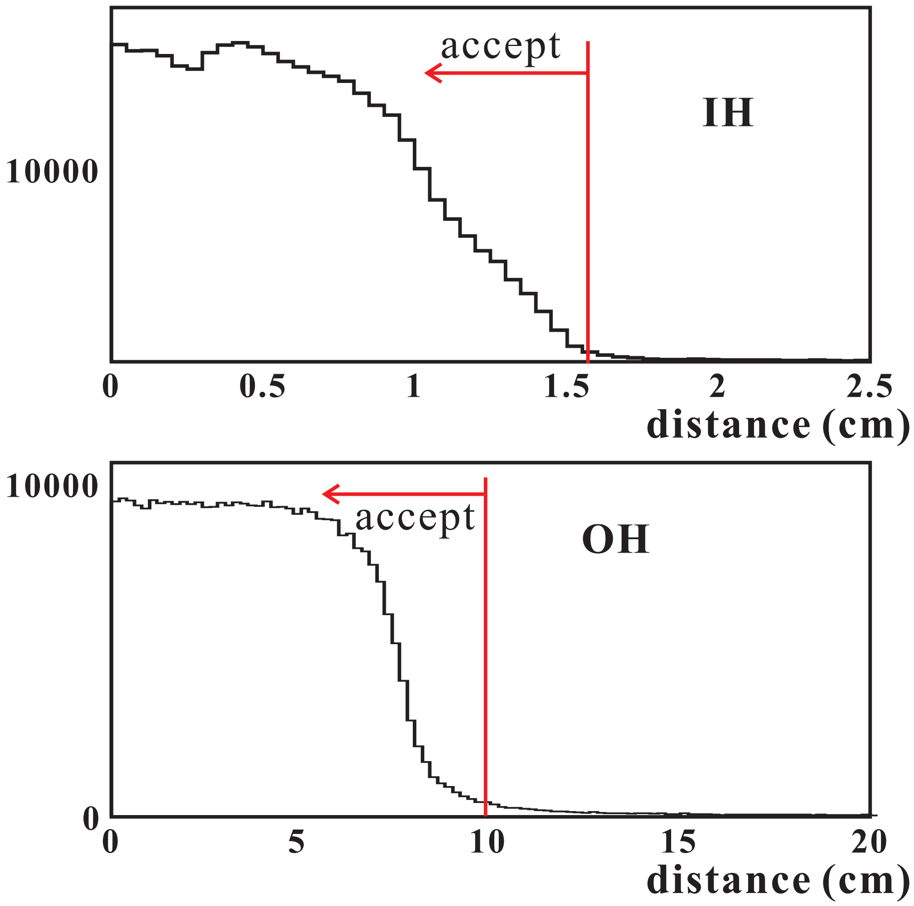

Figure 3.15: *The residual distribution between a center of hodoscope and the point extrapolated from the track.*

3.4.3 Momentum reconstruction

Particle momentum p was calculated by

$$p = \sqrt{{p_H}^2 + {p_V}^2},$$

where p_H and p_V were horizontal and vertical momenta, respectively. p_H was calculated from the curvature of the trajectory measured by drift chambers. On the other hand, p_V was estimated from p_H , z_{OH} and flight length (fl),

$$p_V = p_H \cdot \frac{z_{OH}}{fl}.$$

fl was the length from IH to OH calculated by 4th Runge-Kutta method from DC to IH and OH.

3.4.4 Plane efficiencies and residual resolutions in a plane

The chamber plane efficiency and resolution were estimated for pions (Figure 3.16). In these estimations, tracking was carried out without using the layer for investigation. To select the events as clear as possible, the following conditions were required.

- Number of hits of IH, OH and tagger is all one
- Max layer hits of DC equals to 1
- Number of tracks is 1 for both Left and Right arms
- Both inside and outside of the measured layers (except layer 1,15) include hits
- Two inside layers for layer 1,15 include hits
- Pions are selected from relation between momentum and velocity (see Sect. 3.5)

The plane efficiencies were found to be typically 95% in CDC and 90% in SDC.

These resolutions include resolutions of the trajectories. Therefore, to estimate the effects of trajectory resolution, simulation data were analyzed assuming some resolutions (Fig. 3.17). Figure 3.18 shows the ratio of resolutions of plane to trajectory. The resolutions of trajectory were estimated by

$$\begin{aligned}
(\sigma_{total}^{simulation})^2 &= (\sigma_{plane}^{simulation})^2 + (\sigma_{trajectory}^{simulation})^2. \\
f &\equiv \frac{\sigma_{trajectory}^{simulation}}{\sigma_{plane}^{simulation}} = \sqrt{(\sigma_{total}^{simulation})^2 - (\sigma_{plane}^{simulation})^2}/\sigma_{plane}^{simulation} \quad \text{for each layer}
\end{aligned}$$

where $\sigma_{total}^{simulation}$ is derived by fitting the residual distribution, $\sigma_{plane}^{simulation}$ is the assumed chamber resolution introduced to simulation and $\sigma_{trajectory}^{simulation}$ is the resolution of trajectory. In the range from $\sigma_{plane}^{simulation} = 300$ to $600\mu m$, the ratios are constant for each layers. Therefore, using these ratios, the resolutions of data were estimated as

$$\begin{aligned}
(\sigma_{total}^{measured})^2 &= (\sigma_{plane}^{measured})^2 + (\sigma_{trajectory}^{measured})^2 = (1+f^2)(\sigma_{plane}^{measured})^2 \\
\sigma_{plane}^{measured} &= \frac{1}{\sqrt{1+f^2}}\sigma_{total}^{measured}.
\end{aligned}$$

where $\sigma_{total}^{measured}$ is derived by fitting the residual distribution, $\sigma_{plane}^{measured}$ is the spatial resolution of each plane and $\sigma_{trajectory}^{measured}$ is the resolution of trajectory whose relation to $\sigma_{plane}^{measured}$ is assumed to be the same with that of simulation. Figure 3.19 shows results after subtraction of resolution of trajectories. Typical values of the plane resolutions were found to be 400μm for CDC and 500μm for SDC.

Figure 3.20 shows χ^2 distribution for events which are selected as pions assuming the position resolution of 300 μm for each layers. For detecting K^0, we accepted $\chi^2 < 8$ for both tracks.

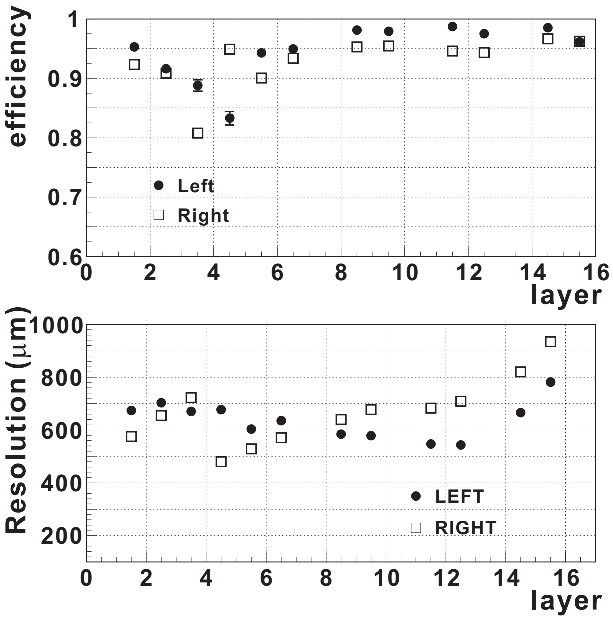

Figure 3.16: *Plane efficiencies and residual resolutions for each plane.*

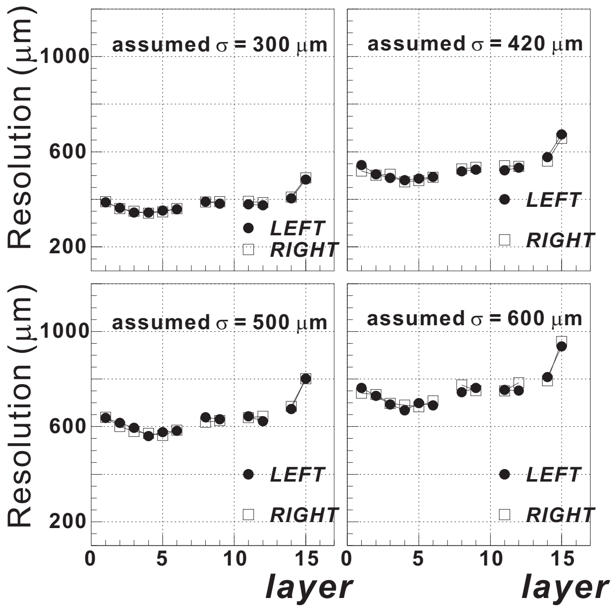

Figure 3.17: *Spatial resolutions of the drift chambers evaluated by analysis for simulation data. Plane resolutions are assumed as 300, 420, 500, 600μm , respectively.*

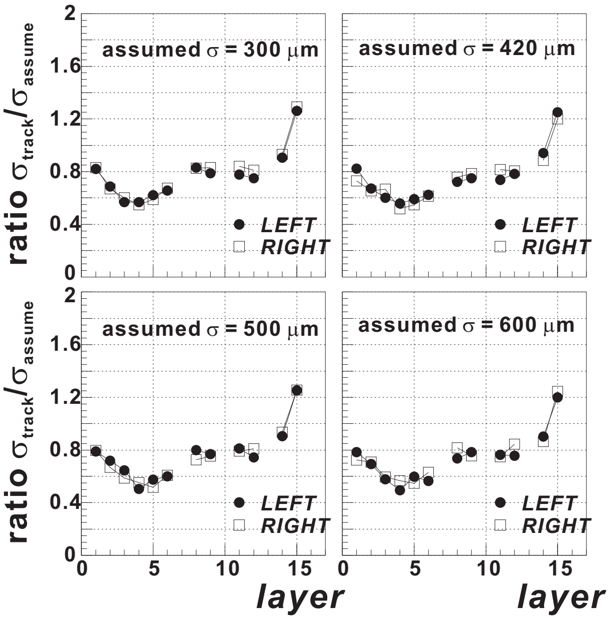

Figure 3.18: *Estimation of the ratios of the resolution for trajectories to that for the plane for each layer. Plane resolutions are assumed as 300, 420, 500, 600μm , respectively.*

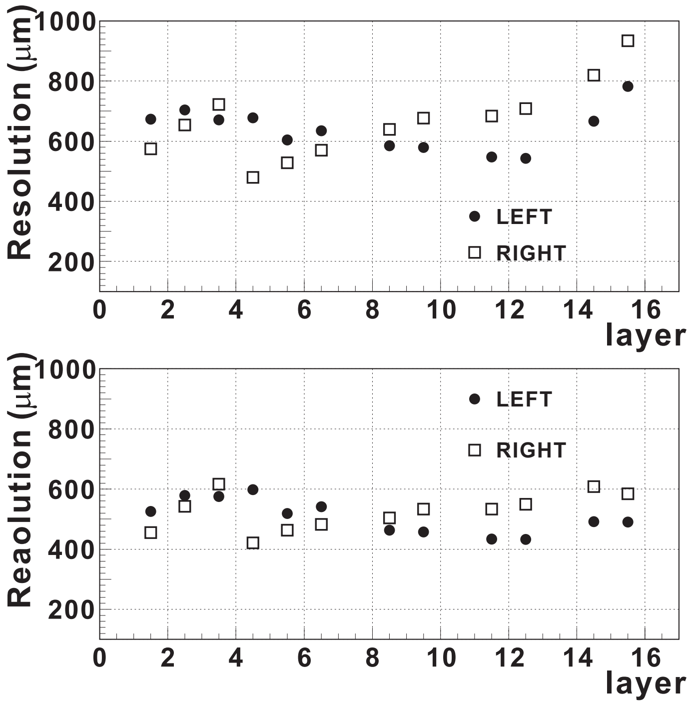

Figure 3.19: *Chamber resolutions for each layers before (top) and after (bottom) subtraction of resolutions of trajectories.*

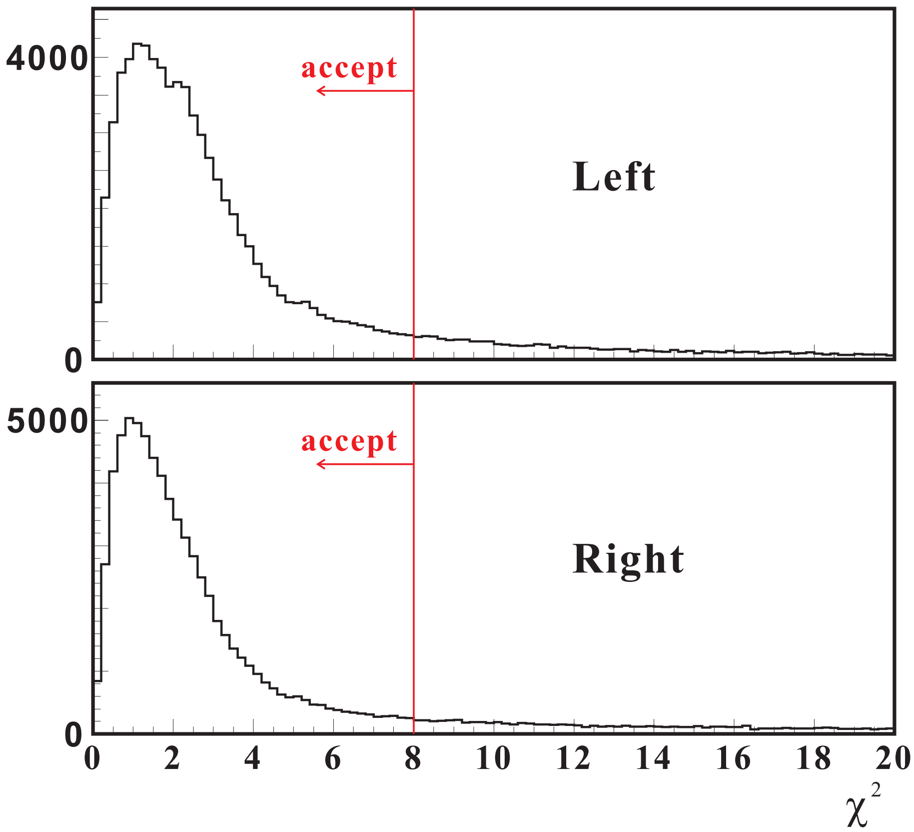

Figure 3.20: χ^2 *distribution for pions. Top for Left arm, bottom for Right arm, respectively.*

3.5 Particle identification

In this section, the separation between protons and pions is described.

The process $\gamma \to e^+e^-$ caused the largest background even using EV in the trigger level. In analysis, the e^+e^- pairs generated upstream of the target were removed by the vertex point selection. Figure 3.21 shows a vertex point distribution along the beam line. The structure in upstream corresponds to the step size of Runge-Kutta method used for extrapolation of the trajectory. Details for the vertex point are explained in Sect. 3.6. When the opening angle is very small, the vertex point is derived at the extrapolated point. Because the acceptance for e^+e^- events generated near the target is much smaller than that generated in the upstream region, most of the e^+e^- events are removed by selection of the vertex point near the target.

Furthermore, the opening angle of e^+e^- is very small, $\cos\theta_{OA} \sim 1$, while the opening angle of $\pi^+\pi^-$ from K^0_S is relatively large. Hence, we applied the opening angle cut, $-0.9 < \cos\theta_{OA} < 0.8$ to remove the e^+e^- events. Details for the opening angle are also explained in Sect. 3.6.

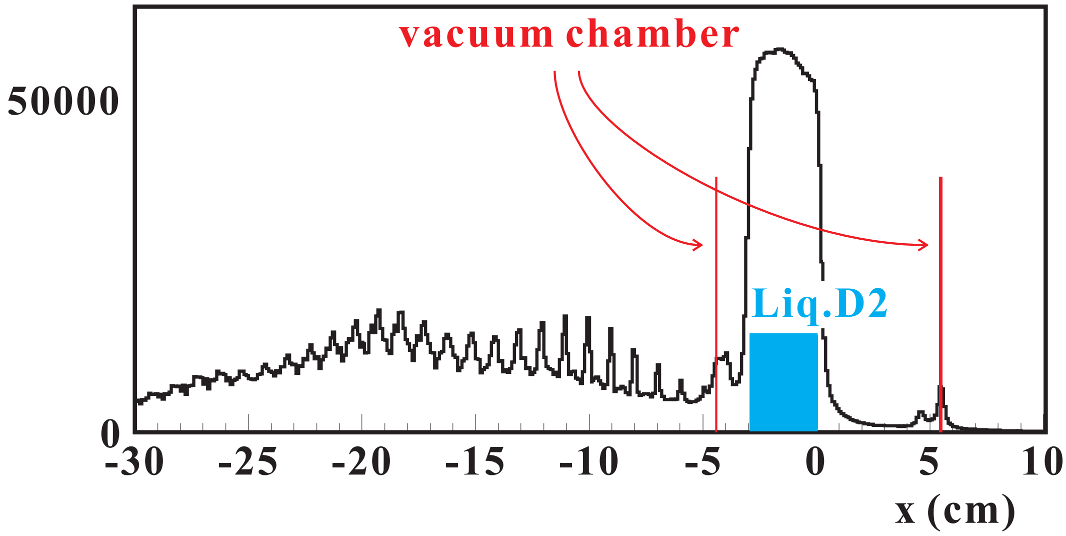

Figure 3.21: *Vertex point distribution along the beam line. The structure in upstream are due to analysis method. The distance between the peaks corresponds to the step size of Runge-Kutta method used for extrapolation of the trajectory.*

Figure 3.22 shows the scatter plot of inversed velocities v.s. momenta of particles after applying the cut of opening angles, that is $-0.9 < \cos\theta_{OA} < 0.8$, and the selection of decay points near the target. The sign of momentum represents the charge of a particle. The particles were identified by selecting the regions drawn by solid lines. These regions are represented as the following conditions,

$$\left.\begin{array}{l} 0.5 < 1/\beta \\ \pm 0.144/(1/\beta - 0.2) - 0.08 \lesseqgtr p \lesseqgtr \pm 0.5/\sqrt{1/\beta^2 - 1} \end{array}\right\} \text{ for } \pi^\pm ,$$

$$0.5/\sqrt{1/\beta^2 - 1} < p < 2.5/\sqrt{1/\beta^2 - 1} \qquad \text{for proton.}$$

Figure 3.23 shows the distributions of inversed velocities for three momentum regions, from 0.5 to 0.52, 0.6 to 0.62 and 0.7 to 0.72 GeV/c, respectively. The distributions are fitted with two gaussians. Vertical lines indicate the threshold. Although the separation between pion and proton is worse as momentum is higher, the rate that proton is identified as pion is less than 3 % even for the momentum of 0.7 GeV/c. Figure 3.24 shows the momentum distributions of pions calculated by Monte Carlo simulation for the photon energies of 0.95, 1.0 and 1.1 GeV. The momentum distribution of neutron was assumed as in Fig. 3.32-(1) and the angular distribution of K^0 was assumed to be uniform in the center of mass system. The momentum of pion from K^0 decay is typically 0.25 GeV/c in the present photon energy. The existence of pions with the momentum of more than 0.7 GeV/c are less than 0.1 % even the photon energy of 1.1 GeV and the fermi momentum of neutron are assumed. Moreover, the inefficiency of the selection of pions is considered in the acceptance of NKS as described in Sect. 3.10.1

Picture/PID2.eps

Figure 3.22: *The scatter plot of inversed velocity v.s. momentum. The sign of momentum represents the charge. To remove electrons and positrons, events are required in which a vertex can be reconstructed from two tracks and its opening angle, θ_{OA}, is* $\cos\theta_{OA} < 0.8$.

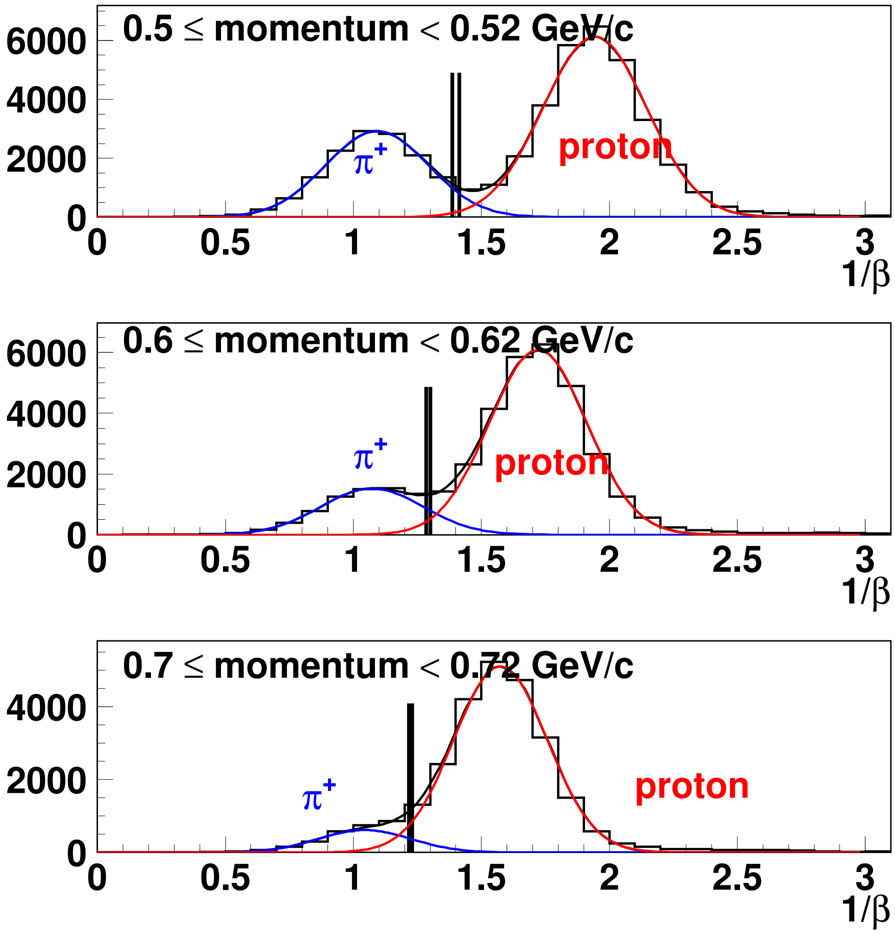

Figure 3.23: *The distributions of the inversed velocity for three momentum regions, from 0.5 to 0.52 (upper), from 0.6 to 0.62 (middle) and 0.7 to 0.72 (lower) GeV/c, respectively. The distribution is fitted with two gaussians. Vertical lines indicate the threshold.*

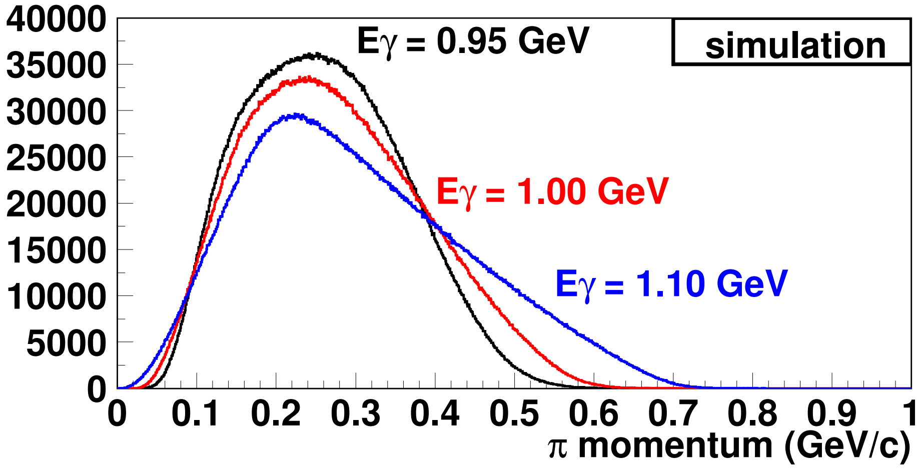

Figure 3.24: *The momentum distributions of pions calculated by Monte Carlo simulation for the photon energies of 0.95, 1.0 and 1.1 GeV. The fermi momentum of neutron was assumed as in Fig. 3.32-(1) and the angular distribution of* K^0 *was assumed to be uniform in the center of mass system.*

3.6 Event selection

When two trajectories are obtained, a vertex point can be reconstructed as a intersection point of extrapolations of these trajectories. Figure 3.25 shows the method of vertex reconstruction. We accepted that the two tracks were intersected, that is *dist* = 0.0 cm (Fig. 3.26).

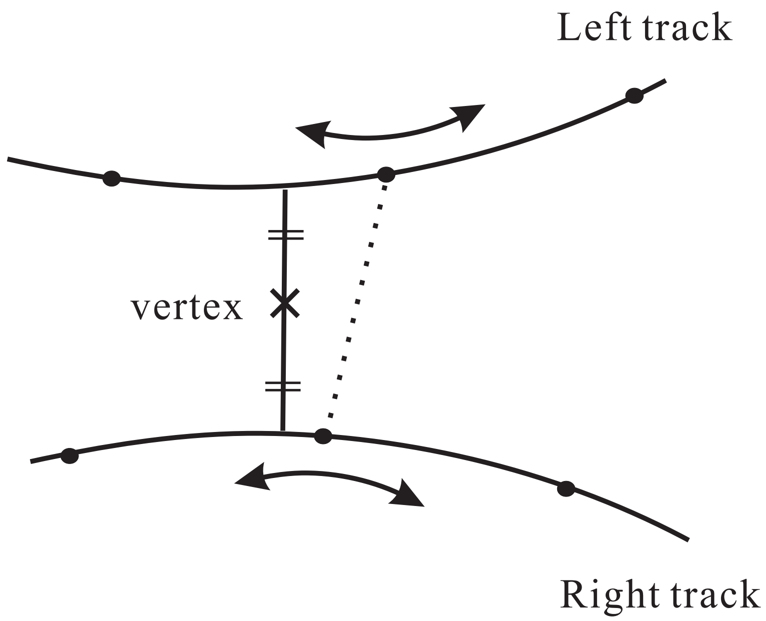

Figure 3.25: *Vertex reconstruction from two tracks. The distance between the closest points of two tracks was calculated at that time.*

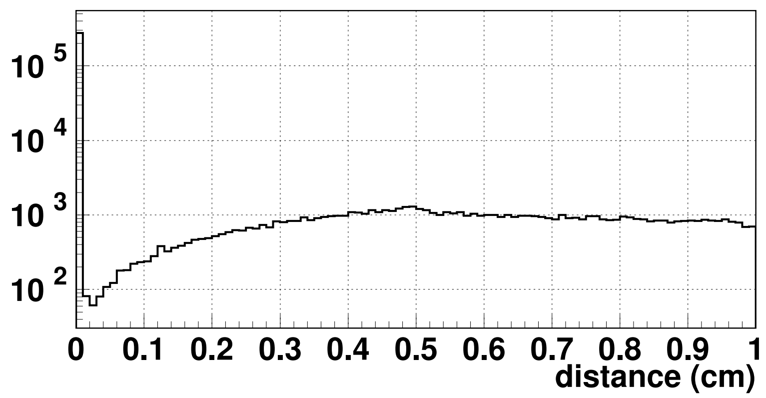

Figure 3.26: *The distribution of the distance of two tracks at vertex.*

Figure 3.27 shows the opening angle distribution for K_S^0 by Monte Carlo simulation for the photon energy of 0.95, 1.0 and 1.05 GeV and assuming the Fermi momentum of neutron (Fig. 3.32-(1)). The opening angle, $\cos\theta_{OA}$, for K_S^0 is less than 0.8, kinematically in the photon energy of the present experiment. Applying the cut of $\cos\theta_{OA} < 0.8$, almost all e^+e^- events can be removed. Furthermore, when the opening angle is large, it is difficult to calculate the vertex point. Therefore, the opening angle cut of $-0.9 < \cos\theta_{OA} < 0.8$ was applied in the present analysis.

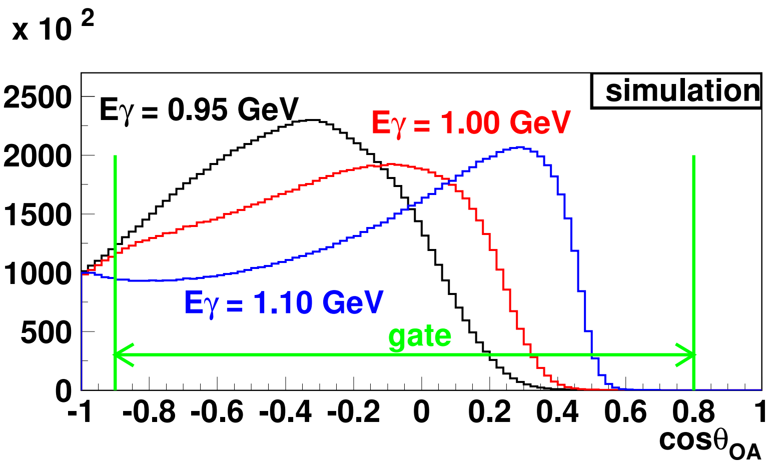

Figure 3.27: *Opening angle distribution for $\pi^+\pi^-$ from K_S^0 calculated by Monte Carlo simulation for the photon energy of 0.95, 1.0 and 1.05 GeV. The fermi momentum of neutron was assumed as in Fig. 3.32-(1) and the angular distribution of K^0 was assumed to be uniform in the center of mass system. In present analysis, a cut for the region of $-0.9 \leq \cos\theta_{OA} \leq 0.8$ was applied.*

Figure 3.28 shows the vertex point distribution around the target for $\pi^+\pi^-$ events. The materials around the target are also drawn in the figure. Figure 3.29 shows the distribution along the beam line. The resolution of the vertex point was found to be about 1.3 mm. Although most of the events came from the target, the events which were generated at the vacuum chamber or mylar film can be seen. Figure 3.30 shows spectra of the $\pi^+\pi^-$ invariant mass for the events reconstructed in the target and out of the target. For events in the target region, huge background of non-strangeness processes, e.g. production of ρ, nucleon resonances and multi-pions, etc. exist, thereby K^0 events are not seen in the invariant mass spectrum. In contrast, for the events whose vertex were reconstructed out of the target, a peak of K^0 is clearly seen because the life of K^0, $c\tau \sim 2.68$ cm, is relatively longer than that of other processes which decay immediately by strong interaction. Thus, we defined the Decay Volume to search for K_s^0 as the following conditions,

$$
\begin{aligned}
(\; VT_x \;\; &> \;\; 2.0 \; (cm) \;) \; \oplus \; (\; |VT_y| > 2.5 \; (cm) \;) \\
&\otimes \\
r \;\; &= \;\; \sqrt{(VT_x - 2.0)^2 \; + \; VT_y^2} < 5.0 \; (cm),
\end{aligned}
$$

where VT_x and VT_y are the coordinates in the frame in which the center of the target is origin as shown in Fig. 3.31. Because the target position was different in each experimental period, the coordinates of VT_x and VT_y are used.

Besides, in order to suppress the background, we apply the cut to the generating points of K^0. The cut conditions are

$$\begin{aligned} 1.8 &< dlen < 5.5 \text{ (cm)} \\ |G_x| &< 1.8, \quad |G_y| \ < \ 2.5, \end{aligned}$$

where G_x and G_y are generating points measured from the center of target, and *dlen* is the distance between the generating point and the vertex point as shown in Fig. 3.31. *dlen* and G_x, G_y were derived from the following equations,

$$\begin{aligned} dlen &= \frac{\vec{P_K} \cdot \vec{VT}}{P_K} \\ \vec{G} &= \vec{VT} - dlen \cdot \frac{\vec{P_K}}{P_K}. \end{aligned}$$

Picture/VertexDistribution2Dim.eps

Figure 3.28: *The vertex distribution. The materials around target are drawn. Almost all events come from the target region.*

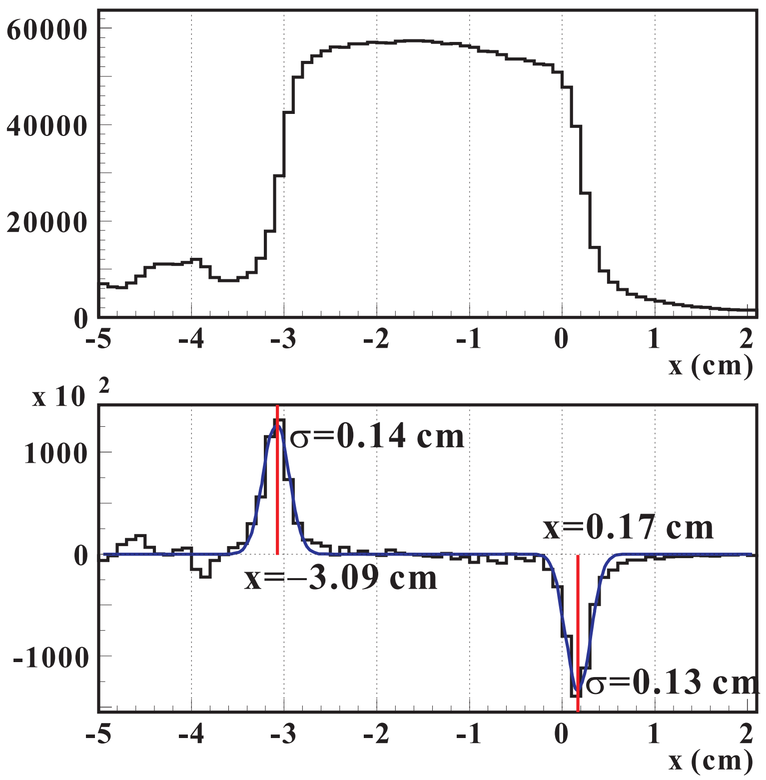

Figure 3.29: *Upper panel shows vertex point distribution along the beam line. Lower one shows the differential of the vertex point distribution and results of the fitting with two gaussians. Vertex point resolution is estimated to be about 1.3 mm in rms.*

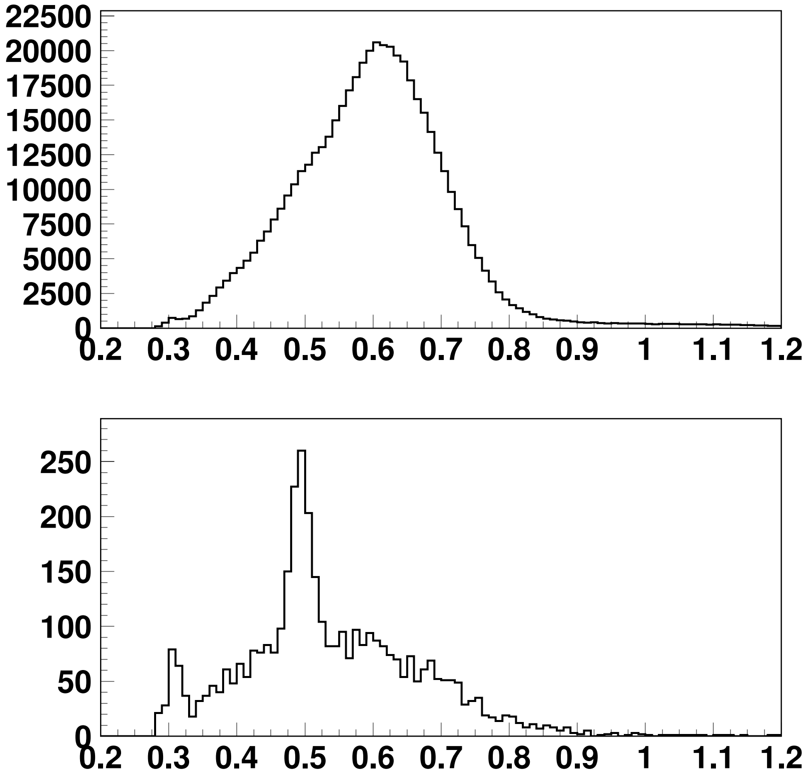

Figure 3.30: $\pi^+\pi^-$ *invariant mass spectrum in the target region (up) and in the decay volume (down). A peak at 0.3 GeV/c^2 is caused from e^+e^- events idendified as $\pi^+\pi^-$ events.*

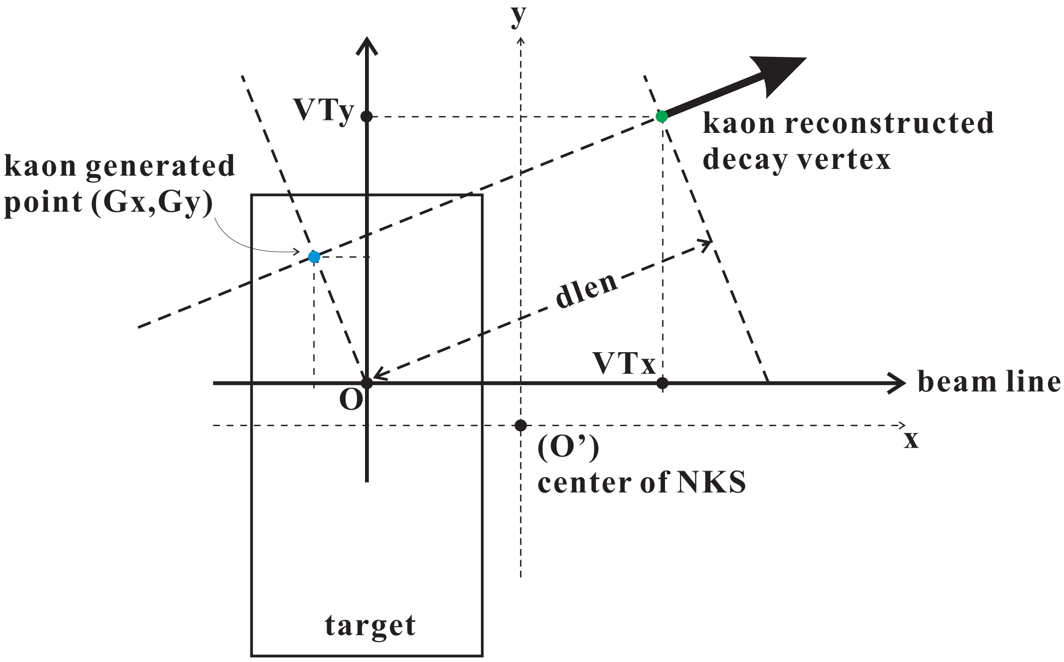

Figure 3.31: *Schematic view of the definition of the vertex and generate points. The flight of length of* K^0, *dlen, is defined as the length between the generate point and vertex point.*

3.7 Estimation of the background

In Fig. 3.30, the background contribution rather than K^0's exists in the $\pi^+\pi^-$ invariant mass spectrum even in the decay volume, and the ratio of signal(S) to noise(N), S/N, is about 1 in the mass gate from 0.46 to 0.54 GeV/c^2. The origin of this background is considered as

case 1 : leakage from the target region due to the finite resolution of the vertex points.

case 2 : wrong combination, such as π^+ from K^0 and π^- from Λ .

3.7.1 case 1

The background of case 1 is estimated from the experimental data whose vertex points are reconstructed in the target region, because it is considered that the kinematics of this background is almost the same as those of events in the target region.

3.7.2 case 2

The background of case 2 is estimated by Geant4 simulation. In the simulation, the following conditions were assumed,

1. K^0 and Λ were generated isotropically in the center of mass frame,
2. the cross section increased linearly with the energy of photon,
3. Hulthen wave function was used as the momentum distribution of a neutron in the deuteron.

Figure 3.33 shows the invariant mass spectrum for $\pi^+\pi^-$ from simulation data. The shapes of momentum and angular distributions for the wrong combination events were also evaluated. If the assumptions of this evaluation are changed, these shapes may be also changed. Fig. 3.34 shows the results for some situations of the angular and photon energy dependences, and Table 3.1 lists the conditions of these situations. These ambiguities cause the systematic error on the shape of the B.G case 2 of typically $\pm 5\%$.

Then, measured invariant mass spectra (Fig. 3.30) are fitted using a gaussian for the peak of K^0 and the shapes of two backgrounds which are only scaled in the three photon energy regions, that is $0.8 \le E_\gamma < 0.9, 0.9 \le E_\gamma < 1.0$ and $1.0 \le E_\gamma \le 1.1$ GeV (Fig. 3.35). The scale factors for two backgrounds are listed in Table 3.2. Because the scale factor itself is very small, statistical error from these background is small. Hence, the significant error for the cross section is due to the fitting error, typically 5 % for the case 1 and 10 % for the case 2.

3.8 Invariant mass spectrum

We obtained the $\pi^+\pi^-$ invariant mass spectrum in Fig. 3.35. The peak around 0.5 GeV/c^2 is fitted with the gaussian and its RMS width is 15.4 ± 1.5 MeV/c^2 for the

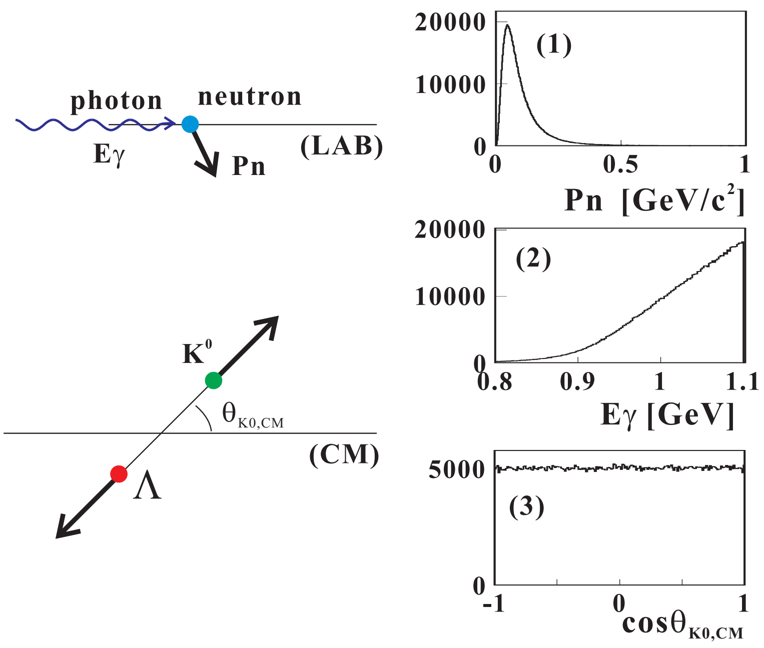

Figure 3.32: *The conditions of the simulation for background estimation. The initial state of $\gamma + n$ is described in laboratory frame. Figure (1) shows the distribution of neutron momenta, and figure (2) shows the distribution of photon energy which has the tail under threshold due to neutron Fermi momentum. Figure (3) shows the angular distribution of K^0 in center of mass frame of γn system.*

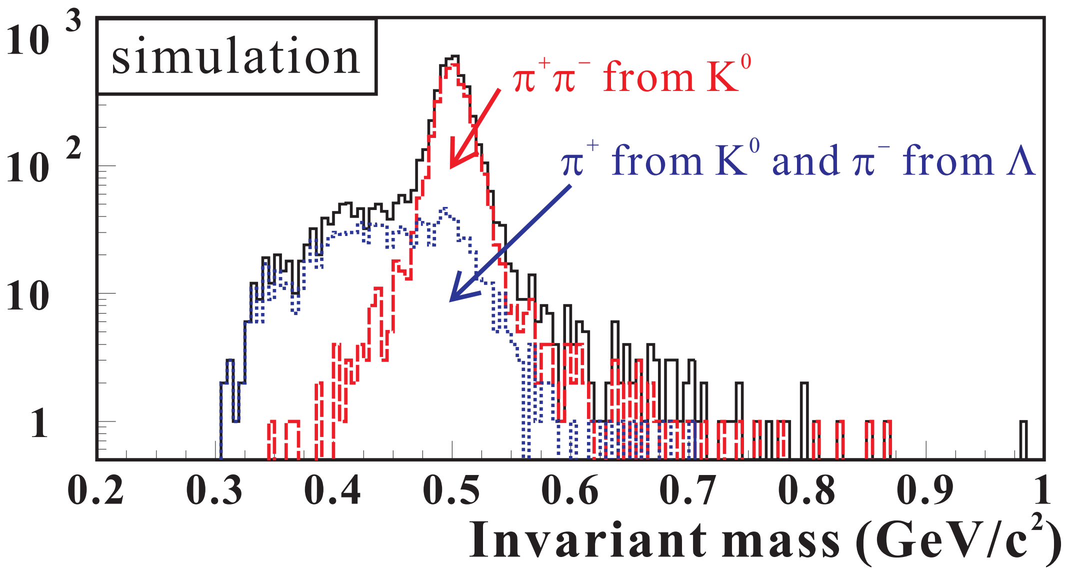

Figure 3.33: *Invariant mass spectrum from the simulation. The contamination of the combination of π^+ from K^0 and π^- from Λ are shown (dotted line), $\pi^+\pi^-$ from K^0 (dashed line).*

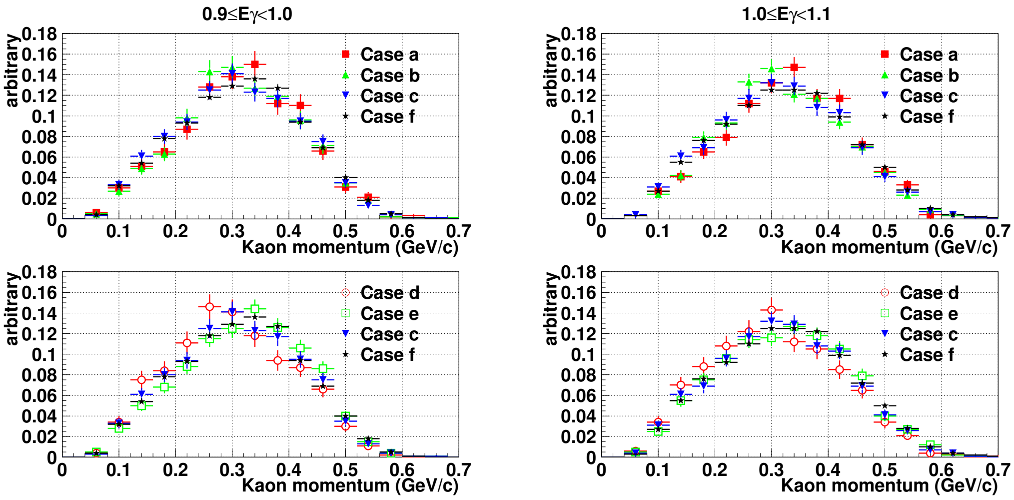

Figure 3.34: *The momentum distribution of wrong combination events for some conditions of simulations. The conditions are listed in Table 3.1. Case f is the same condition with Case 2.*

Table 3.1: *The list of conditions of simulations evaluating the shape of momentum and angular distribution. Case f is the same condition with Case 2.*

	momentum distribution of neutron	energy dependence	angular distribution
Case a	Hulthen w.f.	Linear from threshold	Kaon-MAID (90° peak)
Case b	Hulthen w.f.	Linear from threshold	SLA (backward peak)
Case c	Hulthen w.f.	flat	isotropic
Case d	Hulthen w.f.(200 MeV peak)	flat	isotropic
Case e	Rest	flat	isotropic
Case f	Hulthen w.f.	Linear from threshold	isotropic

photon energy from 0.9 to 1.0 GeV and 14.8 ± 1.8 MeV/c^2 for the photon energy from 1.0 to 1.1 GeV. Then, we set the mass gate from 0.46 to 0.54 GeV/c^2 to select K^0 events. The inefficiency of K^0 selection is estimated by the simulation because the tail exists as shown in Fig. 3.33. According to the simulation, this inefficiency is less than 4 %. Table 3.3 shows the S/N (Signal to Noise) ratio in the invariant mass from 0.46 to 0.54 GeV/c^2. The ratios are found to be about 2 for the photon energy from 0.9 to 1.0 GeV and 1 for the photon energy from 1.0 to 1.1 GeV.

Furthermore, it seems that the peak exists around 0.55 GeV/c^2 in both photon energy regions. Although the origin of the peak can't be found out, the ratio of the number of events of the peak in the mass gate to the number of events of the main peak is less

Table 3.2: *Scale factors for two backgrounds derived by fitting the invariant mass spectra.*

background	photon energy region	scale factor
case 1	$0.8 \leq E_\gamma < 0.9$ GeV	$(4.65 \pm 0.21) \times 10^{-3}$
	$0.9 \leq E_\gamma < 1.0$ GeV	$(4.00 \pm 0.19) \times 10^{-3}$
	$1.0 \leq E_\gamma \leq 1.1$ GeV	$(3.54 \pm 0.19) \times 10^{-3}$
case 2	$0.8 \leq E_\gamma < 0.9$ GeV	$(7.68 \pm 2.22) \times 10^{-2}$
	$0.9 \leq E_\gamma < 1.0$ GeV	$(3.78 \pm 0.41) \times 10^{-2}$
	$1.0 \leq E_\gamma \leq 1.1$ GeV	$(3.04 \pm 0.24) \times 10^{-2}$

Table 3.3: *S/N (Signal to Noise) ratio in the invariant mass from 0.46 to 0.54 GeV/c^2. The noise indicates the sum of backgrounds, that is case 1 + case 2, and the signal is the rest of events after subtraction of the noise from the number of events. The error is statistical and fitting error.*

photon energy region	#events	Signal	Noise	S/N
$0.9 \leq E_\gamma < 1.0$ GeV	584±24	410±25.6	174±9	2.36±0.19
$1.0 \leq E_\gamma \leq 1.1$ GeV	472±22	249±26.1	223±14	1.12±0.14

than 3 %. Because the kinematics of this peak is unknown, it is considered that the systematic error of the invariant mass selection is −3 %.

3.9 Event distribution

Figure 3.36 and 3.37 show the angular and momentum distribution of events after the invariant mass selection. Errors of the data is statistical only. On the other hands, The errors of two backgrounds are mainly the fitting error since the statistical error of backgrounds is small.

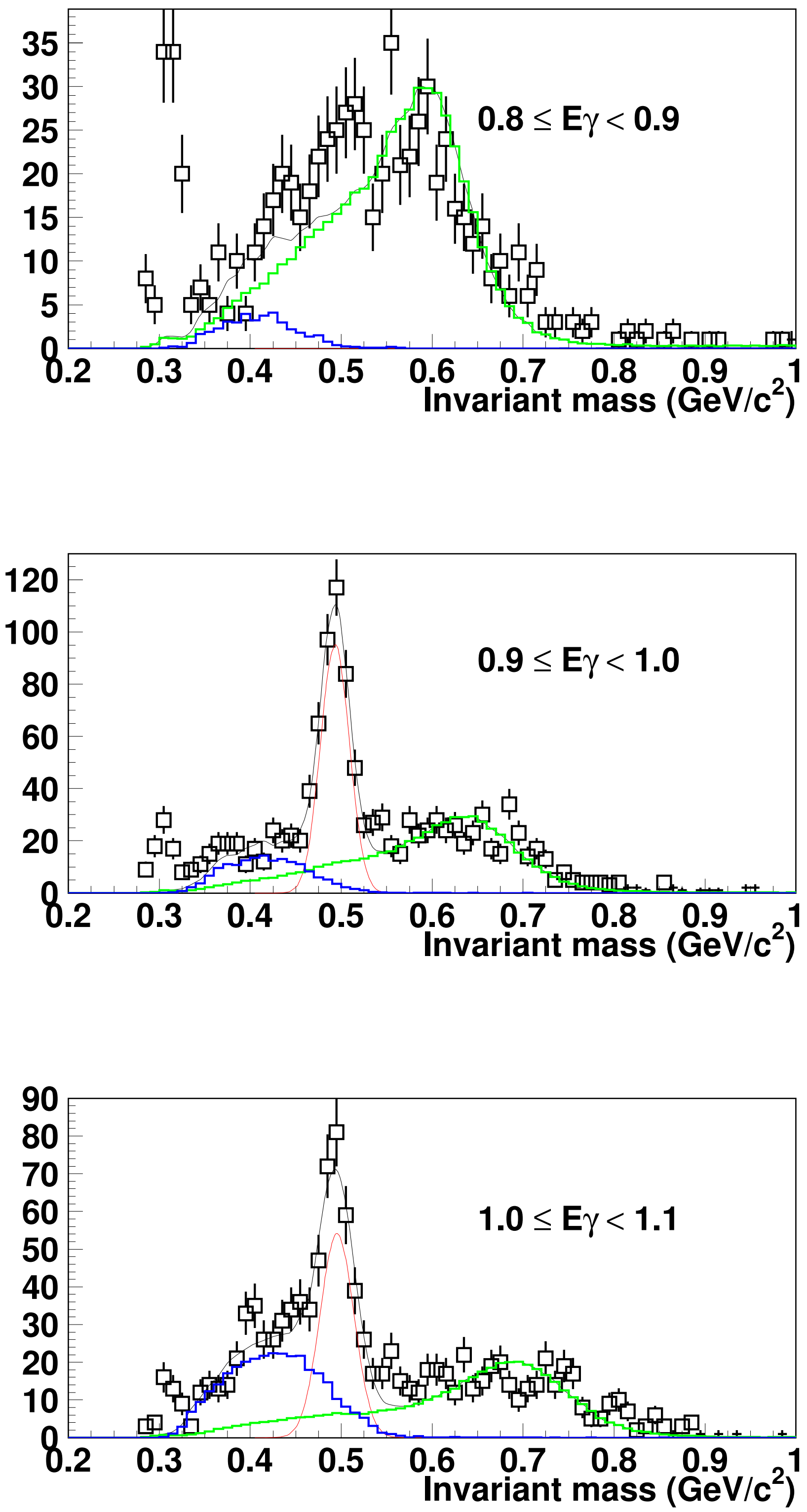

Figure 3.35: *Fitting results of invariant mass spectra in the photon ranges from 0.8 to 0.9 GeV (upper), from 0.9 to 1.0 GeV (middle) and from 1.0 to 1.1 GeV (lower), respectively. The peak around 0.4 GeV/c^2 comes from the wrong combination background and around 0.6 GeV/c^2 comes from the leakage of target events. The peak near 0.3 GeV/c^2 comes from the e^+e^- event.*

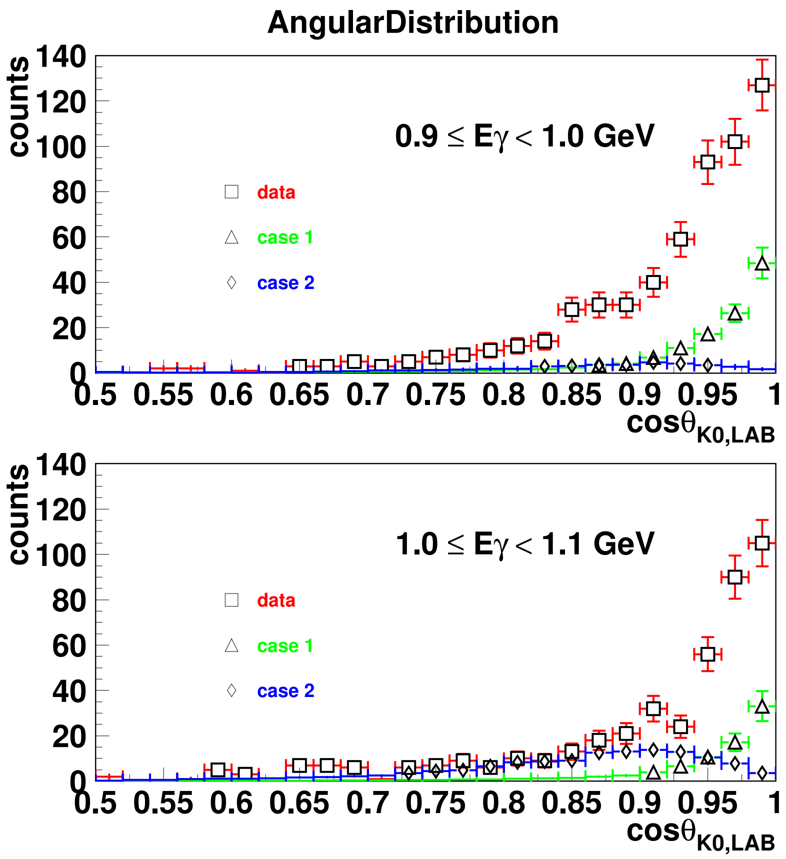

Figure 3.36: *Angular distribution of events with the invariant mass cut for K^0 in the photon energy ranges from 0.9 to 1.0 GeV (upper) and from 1.0 to 1.1 GeV (lower). The background contributions (open triangle for leakage from the target, diamond for wrong combination) are compared with data (open square) The errors of two backgrounds are mainly the fitting error.*

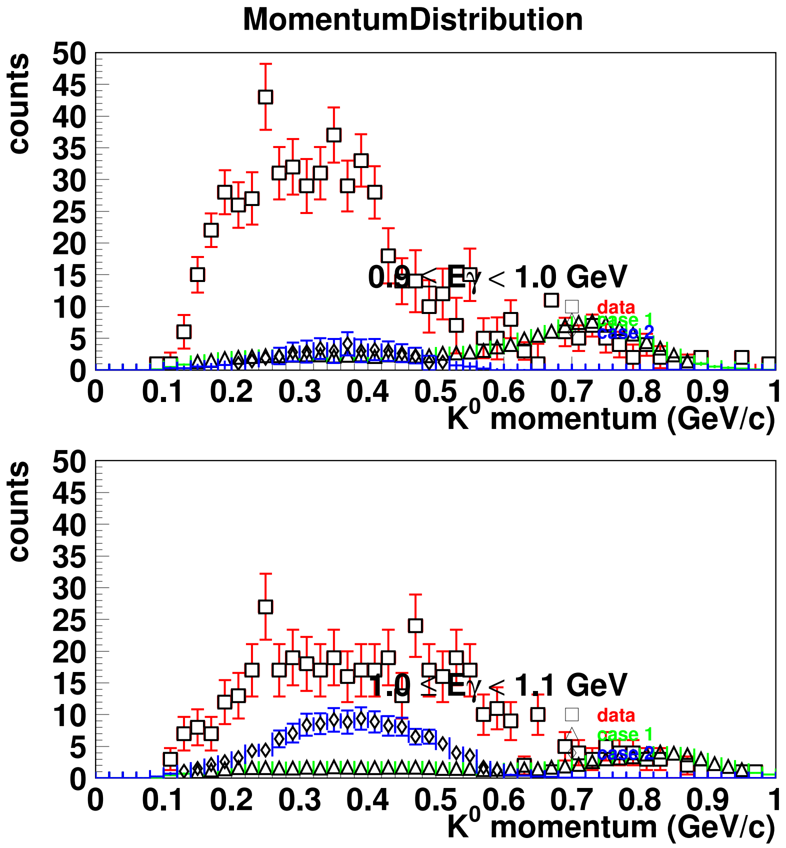

Figure 3.37: *Momentum distribution of events with the invariant mass cut for K^0 in the photon energy ranges from 0.9 to 1.0 GeV (upper) and from 1.0 to 1.1 GeV (lower). The background contributions (open triangle for leakage from the target, diamond for wrong combination) are compared with data (open square). The errors of two backgrounds are mainly the fitting error.*

3.10 Differential cross section

The differential cross section is calculated by

$$\frac{d\sigma}{d\Omega dp} = \frac{N_{yield}(p, \cos\theta)}{N'_{\gamma} \cdot N_{target} \cdot \epsilon_{acpt}(p, \cos\theta) \cdot \epsilon_{DAQ} \cdot \epsilon_{track} \cdot \epsilon_{Gate} \cdot 2\pi \; d(\cos\theta)dp} \tag{3.1}$$

where N_{yield}, N'_{γ} and N_{target} are the number of the selected events, the numebr of photons bombarded on the target and the number of the targets, respectively, $\epsilon_{acpt}(p, \cos\theta)$ is the acceptance of NKS, ϵ_{track}, ϵ_{Gate} and ϵ_{DAQ} are the efficiencies in the tracking analysis, the gating for spectrum and the data taking.

The acceptance $\epsilon_{acpt}(p, \cos\theta)$ is a detection efficiency of K^0s which are generated uniformly in laboratory frame. Because the detection efficiency strongly depends on the momentum and the emitted angle of K^0, the acceptance is evaluated and applied by the momentum and the emitted angle of K^0.

The tracking analysis efficiency is given as

$$\epsilon_{track} = \epsilon_{MLH} \cdot \epsilon_{tracking} \cdot \epsilon_{goodtrack}$$

where ϵ_{MLH}, $\epsilon_{tracking}$ and $\epsilon_{goodtrack}$ are the cut efficiency of the max layer hit selection, the track finding efficiency and the good track selection efficiency, respectively. The definition and the prcedure of estimation of each efficiency is described in Sect. 3.10.5.

The efficiency of gating for spectrum is given as

$$\epsilon_{Gate} = \epsilon_{GateTdiff} \cdot \epsilon_{GateIM}$$

where $\epsilon_{GateTdiff}$ is the efficiency of gating the time difference between IHL and IHR or between TagF and IH, ϵ_{GateIM} is the efficiency of gating the invariant mass spectrum. ϵ_{GateIM} is 96 % and systematic error is -3 % as discussed in Sect. 3.8. The time gate for the time difference between IHL and IHR or between TagF and IH is determined to cover more than 3σ region of the peak. Therefore, $\epsilon_{GateTdiff} = 0.99$ % and their systematic errors are negligible small.

The number of photon, N'_{γ}, is estimated from scaler counts, N_{γ}, after the following correction,

$$N'_{\gamma} = \epsilon_{tagging} \cdot \epsilon_{tagana} \cdot N_{\gamma}$$

where $\epsilon_{tagging}$ and ϵ_{tagana} are the tagging efficiency and the tagger analysis efficiency, respectively. Estimation of these effects are described in Sect. 3.10.2.

The yields of K^0 and the two kinds of backgrounds are corrected by the same procedure, and then, the contributions of backgrounds are subtracted.

3.10.1 Evaluation of acceptance of NKS (ϵ_{acpt})

Acceptance of NKS was evaluated by the Geant4 simulation program. The geometry of NKS was considered realistically. K^0 was generated in the deuterium target with a momentum of 0 to 1.0 GeV/c and $\cos\theta$ of 0.5 to 1 uniformly in the laboratory frame. The generating point was uniform in the target along the beam line with a radius of 5 mm.

The same trigger condition with the experiment was required, and the data was analyzed by the same program. The chamber resolution of 500 μm was assumed, of which value was estimated in Sect. 3.4.2. The plane efficiency of chamber and the resolution of the hodoscope were also assumed to be the estimated values from data. The number of generated K^0 was 40 million for the geometry of each experimental period. The result is shown in Fig. 3.38. The width of a bin is 0.02 GeV/c and 0.02 for $\cos\theta$. The efficiency is maximum at a forward region and the momentum region of about 300 MeV/c.

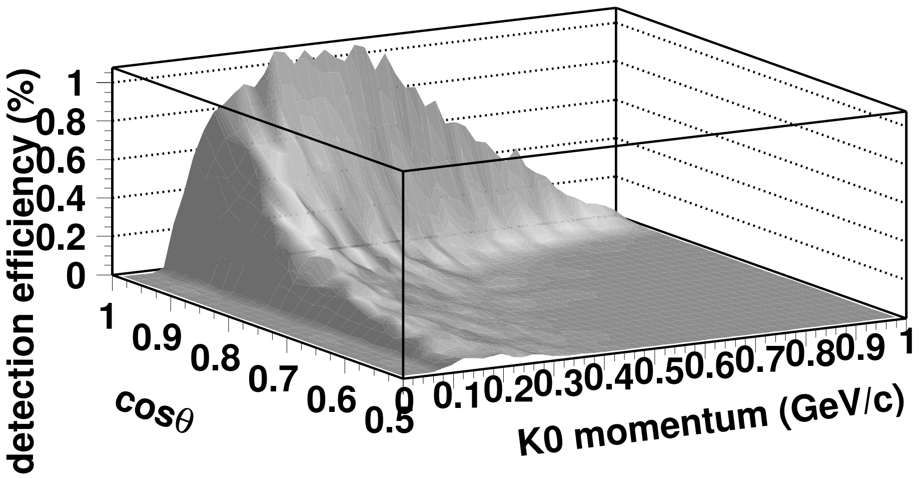

Figure 3.38: *Acceptance map evaluated by simulation. Width of a bin is 0.02 GeV/c and 0.02 for* $\cos\theta$.

The acceptance of each period is different due to a limited position accuracy to setup the detectors and the cryostat. Therefore, although the position of the target cell in the vacuum chamber was fixed as shown in Fig. 2.12, the position to the NKS in each experimental period was different. The positions of the target cell along the beam line were derived from data as listed in Table 3.4.

Table 3.4: *Target position along the beam line in each experimental period. In September, the values correspond to the condition before and after the empty-target run (1st and 3rd), respectively.*

period		position (cm)
September	1st	−2.0
	3rd	−2.2
November		−1.6
December		−1.6
April		−1.5
May		−1.5

Figure 3.39 shows the difference of the acceptance among three periods. The differences among the acceptance for other periods are very small.

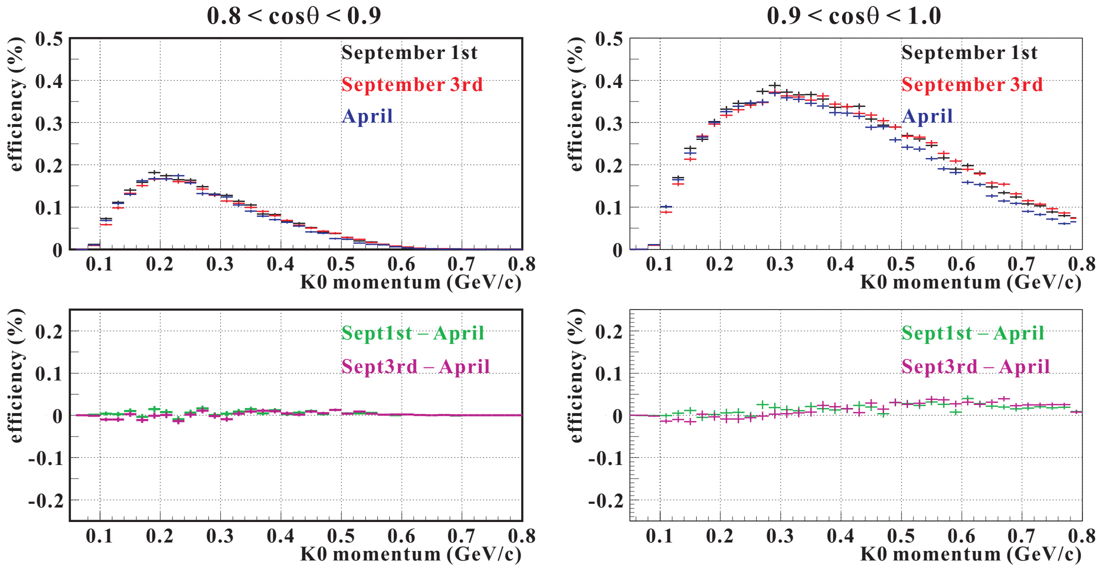

Figure 3.39: *Acceptances in different data-taking periods. The regions of the angle θ are $0.8 < \cos\theta < 0.9$ for the left figures and $0.9 < \cos\theta < 1.0$ for the right figures. Two conditions in September and one in April are compared in upper figures. In lower figure, the differences between September and April are displayed.*

Figure 3.40 is the contour plot of the Fig. 3.38. To avoid the low efficiency area, the effective region is defined as drawn in Fig. 3.40. When the momentum dependence of the cross sections are derived, the effective region is divided into three regions, namely from Region 1 to Region 3, and the results at Region 1 and 2 are compared with theoretical calculations.

Figure 3.41 and 3.42 show the angular and momentum distribution after selections of the invariant mass and the effective region. It is important to check whether the fitting of the invariant mass is reasonable in any kinematical region. For each bin in Fig. 3.42, the invariant mass spectra for the data and two backgrounds are shown in appendix B and the fitting seems to be good.

3.10.2 Number of photons on the target (N'_γ)

The number of photons bombarded on the target was estimated from scaler counts of the tagger. These tagger signals were made from coincidence between TagF and TagB. The estimation must include the effects as follows

(i) Absorption of photons in the region between the radiator and the target, especially, at a collimator positioned upstream of the sweep magnet,

(ii) double count at a neighbor segment of the tagger

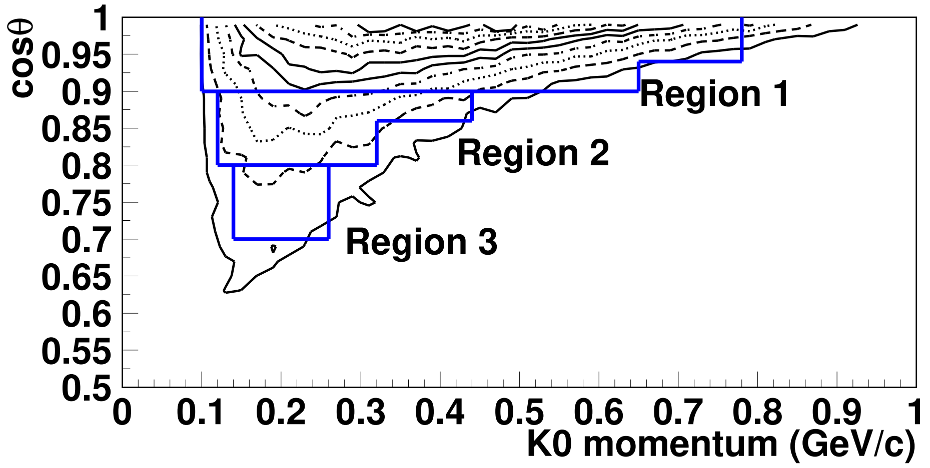

Figure 3.40: *Contour plot of the Fig. 3.38 Solid lines shows accepted region which have efficiency not too small.*

(iii) analysis cut

In the present analysis, two kind of correction factors were introduced; The first effect is named tagging efficiency ($\epsilon_{tagging}$), the second and last are named tagger analysis efficiency (ϵ_{tagana}).

Tagging efficiency ($\epsilon_{tagging}$)

The tagging efficiency was measured at the beginning and the endof each experimental period in order to estimate the number of photons irradiated on the target.

In September 2003, we measured the tagging efficiency with the CsI scintillation counter as a calorimeter. It was positioned at 260 cm downstream from the experimental target position.(see Fig. 3.43). We used CsI and lead glass Cerenkov counters (LG) in November 2003, and used only LG after December 2003 so as to measure the tagging efficiency with higher intensity photon using the LG. The position of the LG the same as the CsI. Figure 3.44 shows the correlation between a hit segment of TagF and ADC spectrum of LG measured in May 2004. The ADC spectrum of LG depends on the TagF segment, that is, photon energy. Dents around TagF15 and TagF46 are due to supports at the window on the accelerator ring.

The tagging efficiency is defined by

$$\epsilon_{tagging} = f_{att.} \cdot \frac{N_{calorimeter}}{N_{tagger}}$$

where $N_{calorimeter}$ and N_{TagF} are number of photons counted by the calorimeter and tagger, respectively, and $f_{att.}$ is the attenuation factor between the target and calorimeter. $\epsilon_{tagging}$ was estimated for each TagF segment.

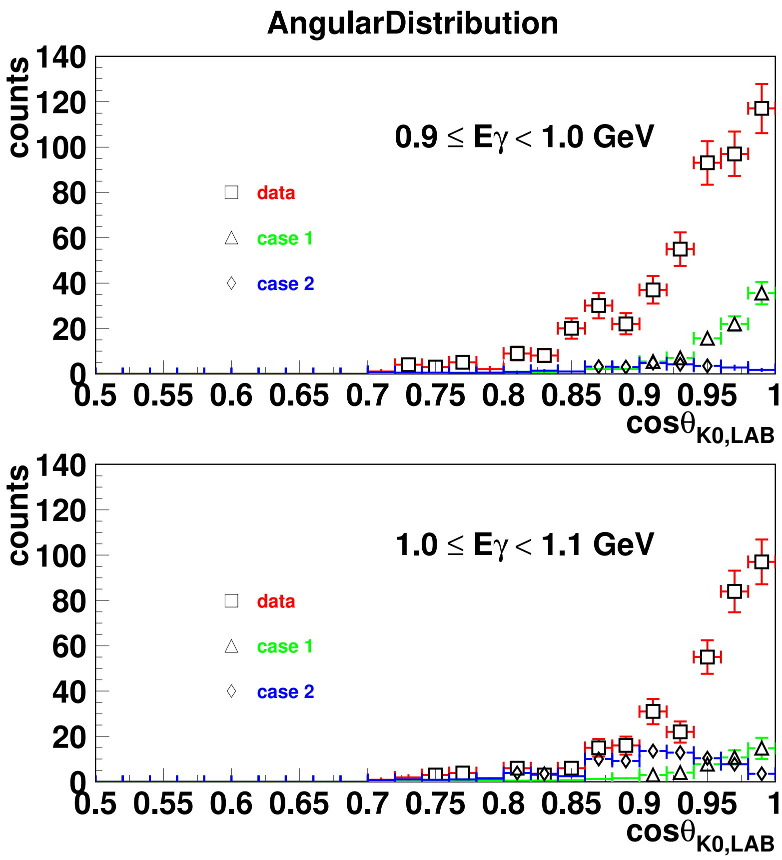

Figure 3.41: *Angular distribution of events after the the invariant mass cut and the selection of the acceptance region in the photon energy region from 0.9 to 1.0 GeV (upper) and from 1.0 to 1.1 GeV (lower). The background contributions (open triangle for leakage from the target, diamond for wrong combination) are compared with data (open square).*

Figure 3.45 shows the tagging efficiencies of each experimental period. Errors are statistical only. Decreases in efficiencies are found around TagF1-10 (high energy side for photon energy) and TagF35-48 (low energy side). In principle, the efficiencies for different segments should be equal because the photon interaction probability between the radiator and the target is almost same in the present energy region. The effect in the high energy side is considered to be caused by the background trigger which are made by interaction with residual gas in the accelerator ring. On the other hand, the effect in the low energy side is considered to be caused by the supports at the window on the accelerator ring. These effects are not corrected since the situation is the same as for the normal data taking in any beam intensity.

The $f_{att.}$ is estimated from radiation length of materials and by a simulation. Both estimations result in almost the same value, $f_{att.} > 99\%$.

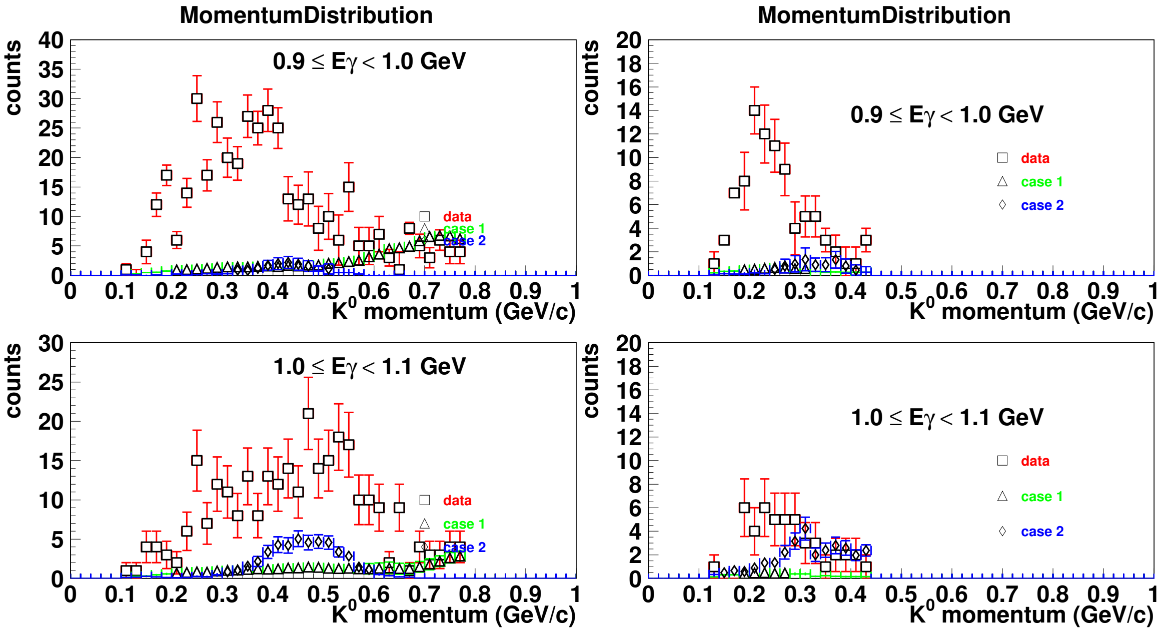

Figure 3.42: *Momentum distribution of events after the invariant mass cut and the selection of the acceptance Region1 (left) and Region2 (right) in the photon energy region from 0.9 to 1.0 GeV (upper) and from 1.0 to 1.1 GeV (lower). The background contributions (open triangle for leakage from the target, diamond for wrong combination) are compared with data (open square).*

Analysis efficiency (ϵ_{tagana})

As mentioned in Sect. 3.3, to remove accidental coincidence between TagF and TagB, we apply various cuts for the tagger in the analysis. The effect is defined as the tagger analysis efficiency, ϵ_{tagana}.

The efficiency is estimated using a tagger trigger run described in Sect. 2.5 and 2.6 and calculated from the ratio between the number of events before and after the cut.

Figure 3.46 shows the beam intensity dependence of the tagger analysis efficiency. These data were taken at beam intensities of 20 kHz, 130 kHz, 1.2 MHz, 1.8 MHz and 2.7 MHz, respectively. Obviously, the efficiencies depend on the beam intensity. This is attributed to increase of the accidental coincidence. In calculating the cross section, the tagger analysis efficiency was taken from a mean value of normal beam intensity runs for each experimental period. Typical efficiencies are listed in Table 3.6. These values are averaged from TagF segment 1 to 20. In normal data taking, fluctuation of the beam intensity was 2.0 ± 0.5 MHz. Therefore, the systematic error of the tagger analysis efficiency is $\pm$ 3%.

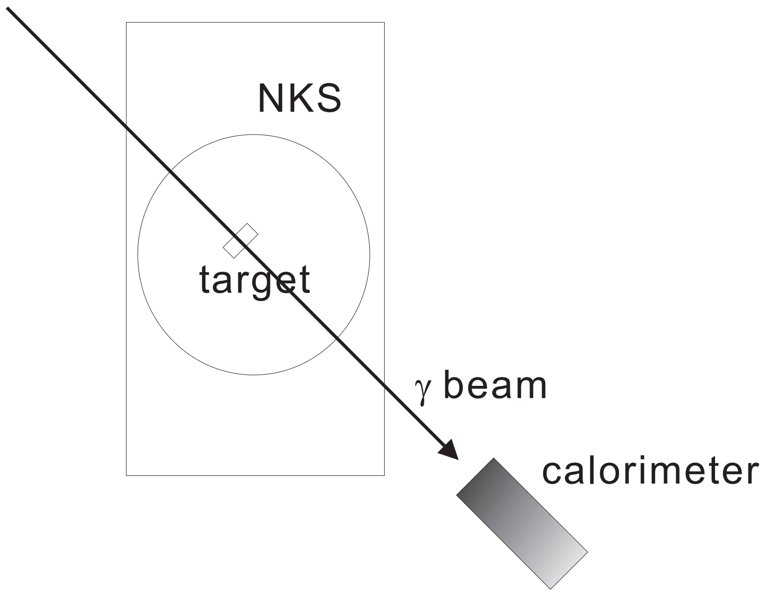

Figure 3.43: *Arrangement of detectors for the measurement of the tagging efficiency.*

Table 3.5: *A typical value of the tagging efficiency for each measurement. The values in the 2nd column are the effciency for tagF segment 1. The values in the 3rd column are averaged for tagF from the segment 10 to 48.*

period	minimum	average
September '03	73.5 %	80.3 %
November '03	74.6 %	79.8 %
December '03	74.9 %	79.7 %
April '04	74.5 %	78.9 %
May '04	74.1 %	78.3 %

Table 3.6: *Typical values of the tagger analysis efficiency for each measurement. The values are averaged for TagF from segment 1 to 20.*

period	average (1 to 20)
September '03	88.1 ± 0.2 (stat.)%
November '03	91.0 ± 0.1 (stat.)%
December '03	90.8 ± 0.1 (stat.)%
April '04	89.1 ± 0.1 (stat.)%
May '04	88.8 ± 0.2 (stat.)%

3.10.3 Number of target nucleon (N_{target})

As mentioned in Sect. 2.4, the temperature of the liquid deuterium and the pressure of residual deuterium gas were monitored through the experimental period. Thereby,

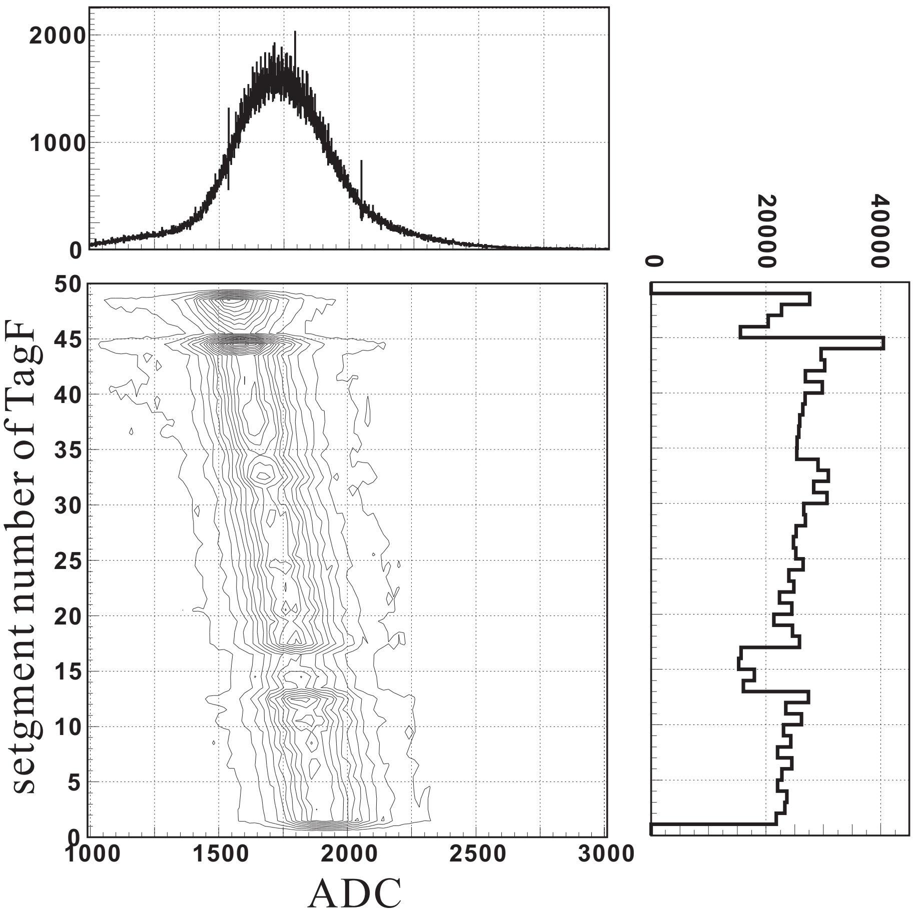

Figure 3.44: *Correlation between the segment number of TagF and the ADC spectrum of lead grass detector. Upper and right panels show the projected spectrum. Dents around TagF15 and TagF46 are due to the supports at the window on the vacuum chamber in STB-ring.*

the density of the liquid deuterium can be calculated. Because fluctuations of the temperature and the pressure did not much affect the density of deuterium target, these fluctuations give no uncertainty or error in the evaluated cross section. In contrast, the change of the thickness of the target cell due to the pressure of liquid deuterium gives larger uncertainty than density. The expansion of the target cell was calculated by finite element method (FEM) and evaluated to be about 2 mm for both side. Besides, the thickness of the target during the experiments was estimated to be about 3.3 cm from the vertex points distribution (Fig. 3.29). This is consistent with the FEM result.

In addition, due to fluctuation of the circulating electron beam trajectory, the position of photons on the target changed slowly. It was corrected by adjusting the position of the radiator, and so the fluctuation of the beam position on the target was less than 5 mm. The fluctuation of 1 mm at the radiator corresponds to that of 5 mm at the target. Besides, when the change of circulating electron beam orbit exceeded the threshold (0.5 mm), the beam orbit was corrected by adjusting RF frequency of accelerator. Figure

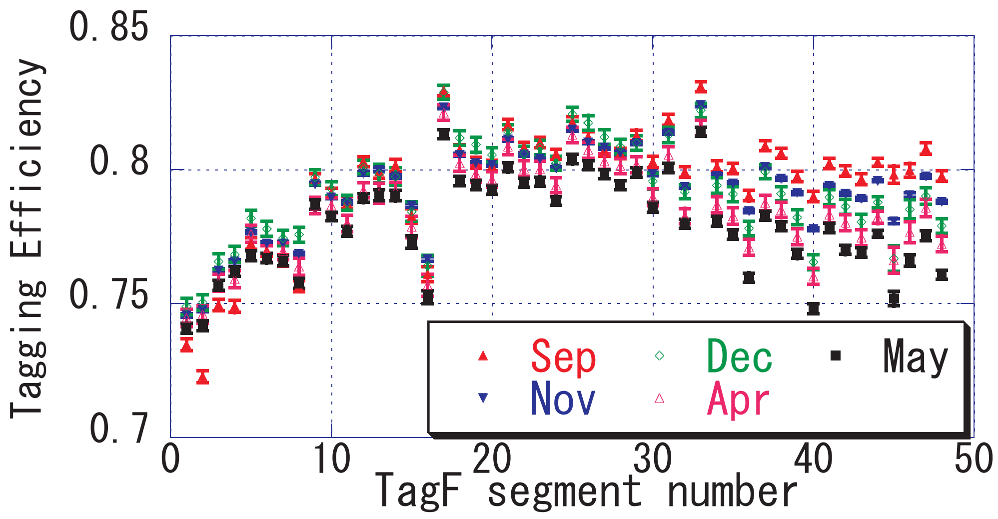

Figure 3.45: *Tagging Efficiencies measured in each experimental period.*

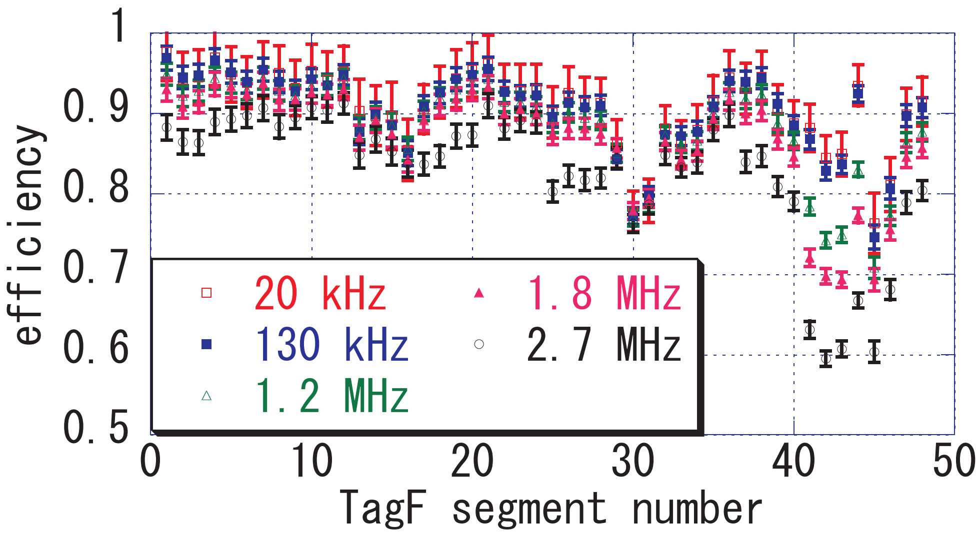

Figure 3.46: *Beam intensity dependence of the tagger analysis efficiencies. When the beam intensity is high, the tagger analysis efficiency is low due to increase of accidental coincidence.*

3.47 shows the dependence of the number of deuterons on the position of photon beam for various expanding condition of mylar films. Because the beam offset was 5 mm at the maximum in each experimental period, the number of deuterons used in analysis was calculated by taking a mean value between 0 to 5 mm. Table 3.7 shows typical values (the equations are written in Appendix A).

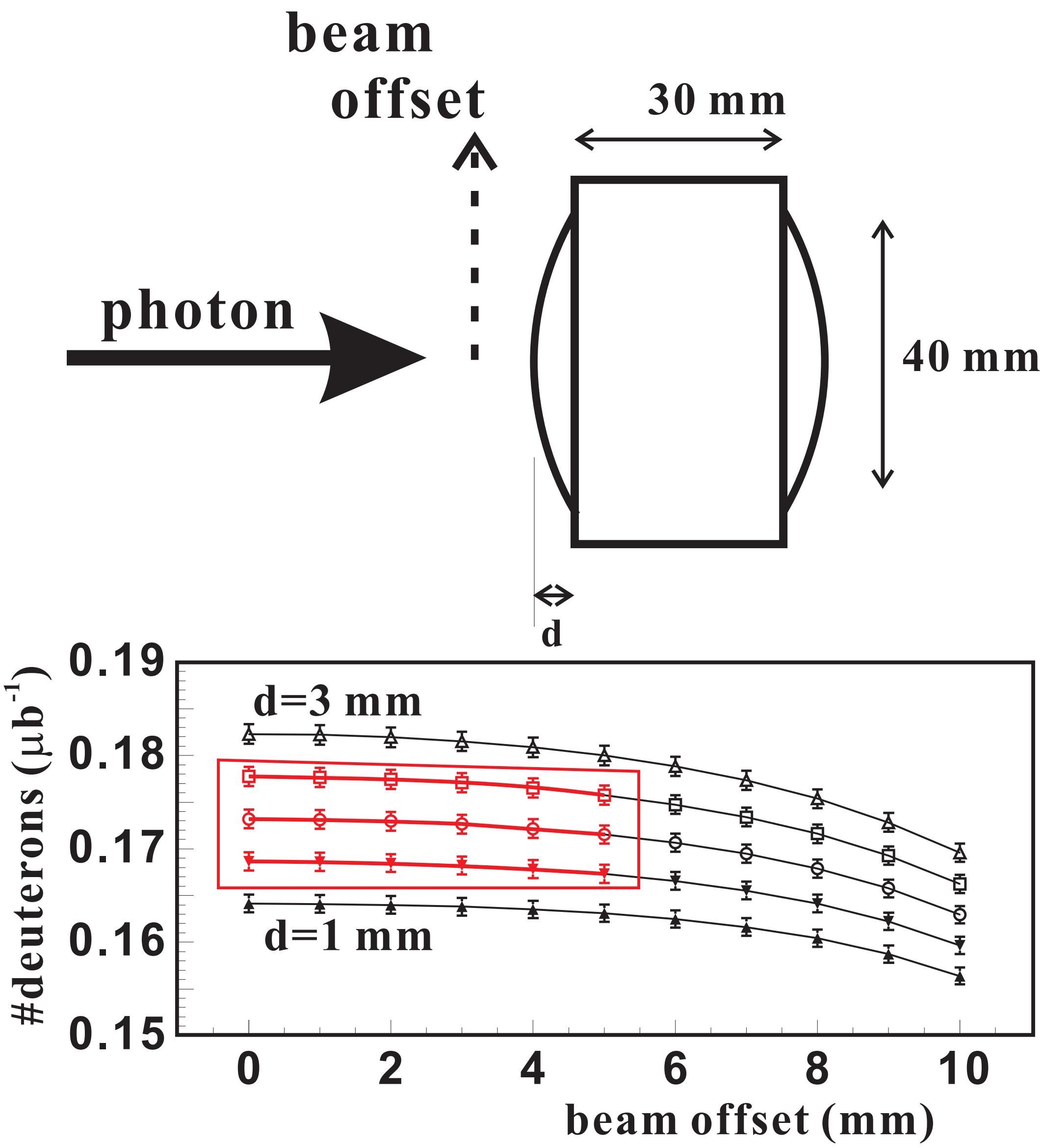

Figure 3.47: *Number of deutrons for the deuteron density of 0.173 g/cm*^{3}*. Upper figure shows the schematic view of the target cell. The expansion of mylar films is drawn exaggeratedly. Lower panel shows the number of neutrons for each beam offsets and expanding condition. The points from top to bottom correspond to the expansions of d=3.0, 2.5, 2.0, 1.5, 1.0 mm. Points inside box are used to evaluate the number of deuterons.*

3.10.4 DAQ efficiency (ϵ_{DAQ})

The DAQ efficiency was evaluated from scaler counts for the requested and accepted triggers. A DAQ efficiency was 90 % for a typical trigger rate of 100 Hz. The DAQ efficiency for each experimental period is listed in Table 3.8

Table 3.7: *The list of number of deuteron. The largest error is due to uncertainty of the thickness of the target.*

month	density of D_2 (g/cm^3)	thickness (cm)	number of deuteron (barn^{-1})
September	0.168 ± 0.001 (stat.)	3.4 ± 0.2 (syst.)	$0.168 \pm 0.001 \pm 0.01$
November $\sim$ May	0.173 ± 0.001 (stat.)	3.4 ± 0.2 (syst.)	$0.173 \pm 0.001 \pm 0.01$

Table 3.8: *DAQ efficiency for each period. In the latter half of September, because beam intensity was high, about 2∼2.5 MHz, DAQ efficiency in September was lower than those of other periods.*

month	DAQ efficiency	statistical error
September (first half)	90.1 %	< 0.1 %
(latter half)	85.1 %	< 0.1 %
November	89.4 %	< 0.1 %
December	91.7 %	< 0.1 %
April	89.8 %	< 0.1 %
May	88.1 %	< 0.1 %

3.10.5 Analysis efficiencies

Pre-selection efficiency (ϵ_{MLH})

Before track search, pre-selections of the MLH cut and the angle correlation cut were applied as mentioned in Sect. 3.4.2. The efficiency of the angle correlation cut depends on the kinematics of pion and the geometry of detectors. This efficiency is included in the acceptance correction. Besides, the MLH efficiency, ϵ_{MLH}, was estimated by the following method. This efficiencies were estimated for every OH segment. We require that the number of hits of TagH , IH and OH for each Left/Right arm are 1 in order to select events as clear as possible. Additionally, for the efficiency of Left arm, we require that the track in Right arm is identified as a pion. From these conditions, the triggered particle in the Left arm is expected to be a hadron. The results are shown in Figure 3.48 and listed in Table 3.9.

Tracking efficiency ($\epsilon_{tracking}$)

Tracking efficiencies were estimated for every OH segment. The event selection was the same as the selection for the MLH efficiency. Nevertheless, in forward and backward direction, there are electrons or positrons which do not go through the chamber but hit IH and OH, so the tracking efficiency is relatively low. Since the tracking efficiencies from OH segment 4 to 12 are nearly flat, we use the mean value in this region as the tracking efficiency. Table 3.10 shows the tracking efficiency for each month.

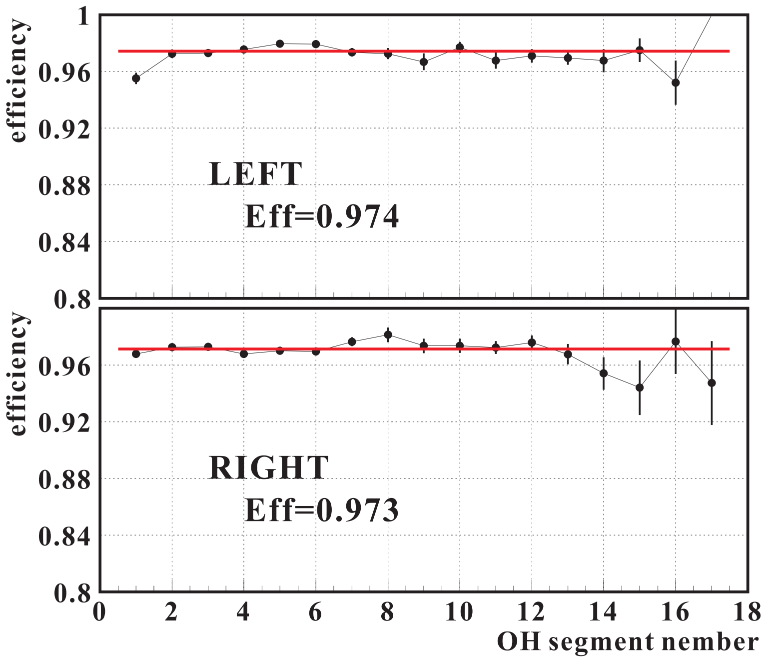

Figure 3.48: *The efficiency of MLH cut in May 2004. The solid line is the value averaged over the OH segments.*

Table 3.9: *MLH efficiency for each period. The error is a statistical one.*

month	Left	Right	Both
September	97.70 ± 0.08	97.72 ± 0.08	95.5 ± 0.1
November	97.56 ± 0.07	97.55 ± 0.06	95.3 ± 0.1
December	97.59 ± 0.05	97.73 ± 0.05	95.3 ± 0.1
April	97.61 ± 0.04	97.41 ± 0.04	95.3 ± 0.1
May	97.41 ± 0.04	97.31 ± 0.04	95.3 ± 0.1

Efficiency of cuts for χ^2 and number of hits in a track ($\epsilon_{goodtrack}$)

As mentioned in Sect. 3.4.2, χ^2 cut was applied for both tracks in Left arm and Right arm. Besides, it was required that the number of hits in a track are larger than 7 for both tracks. Accordingly, the efficiencies for these cuts are estimated. Firstly, the efficiency for the number of hits cut, $\epsilon_{\#hits}$ is estimated, and then the efficiency for χ^2 cut, ϵ_{χ^2} is estimated as

$$\begin{aligned}
\epsilon_{goodtrack} &= \epsilon_{\#htis} \cdot \epsilon_{\chi^2} \\
\epsilon_{\#hits} &= \frac{N_{\#hits>7}}{N} \\
\epsilon_{\chi^2} &= \frac{N_{\#hits>7,\chi^2<8}}{N_{\#hits>7}}.
\end{aligned}$$

The results are shown in Fig. 3.50.

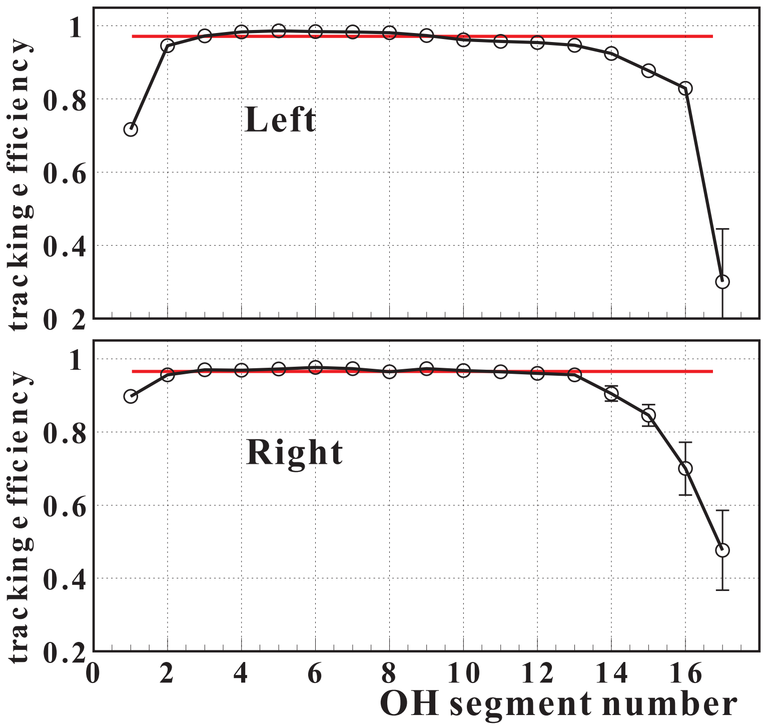

Figure 3.49: *Tracking efficiency*

The systematic error was estimated to be ± 5% from the dependence of photon intensity.

3.10.6 Summary of efficiencies

Table 3.11 shows typical values of efficiencies and its statistical or systematic errors.

Table 3.10: *Tracking efficiency for each period. The error is a statistical one.*

month	Left	Right	Both
September	97.40 ± 0.07	96.88 ± 0.11	94.4 ± 0.1
November	97.41 ± 0.07	96.88 ± 0.11	94.4 ± 0.1
December	97.38 ± 0.09	96.92 ± 0.13	94.4 ± 0.2
April	98.06 ± 0.07	96.48 ± 0.13	94.6 ± 0.1
May	98.00 ± 0.05	97.67 ± 0.06	95.7 ± 0.1

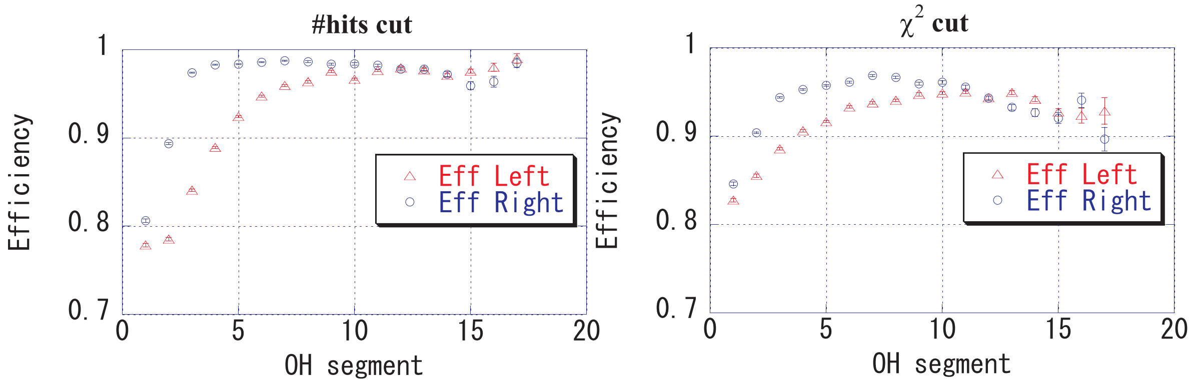

Figure 3.50: *Efficiency for #hits cut (left) and χ^2 cut (right) for the experimental data.*

Table 3.11: *Summary of efficiencies. Each value is averaged (for efficiency) or summed (for N_γ) for all experimental periods. Systematic errors are estimated from the fluctuations among the experimental periods or the fluctuations of photon intensity.*

	item	value	statistical error	systematic error
ϵ_{Gate}	Gating for timing and invariant mass efficiency	95.4%	$< 0.1\%$	$\pm$ 1 %
N_γ	number of hits of TagF from scaler counts	4.6×10^{12}	2.1×10^{6}	
N_{target}	number of target $[barn^{-1}]$	0.172	$\pm$0.001	$\pm$ 0.010
ϵ_{DAQ}	DAQ efficiency	89.1%	< 0.1 %	$\pm$ 1 %
$\epsilon_{tagging}$	tagging efficiency averaged for 10 to 48	79.1 %	$\pm$ 0.1%	$\pm$ 1 %
ϵ_{tagana}	tagger analysis efficiency averaged for TagF 1 to 20	89.4 %	$\pm$ 0.1%	$\pm$ 3 %
ϵ_{MLH}	multiplicity cut	95.2 %	$< 0.1\%$	$\pm$ 1 %
$\epsilon_{tracking}$	tracking efficiency	94.7 %	$< 0.1\%$	$\pm$ 1 %
$\epsilon_{\#hit}$	# hits cut in a track	95%	$< 0.1\%$	$\pm$ 5 %
ϵ_{χ^2}	χ^2 cut	95%	$< 0.1\%$	$\pm$ 3 %

Chapter 4

Results and discussion

In this chapter, experimental results are presented and compared with theoretical calculations mentioned in Chap.1. Firstly, experimental data are presented with a brief description for integrated range of K^0 momentum or angle. Next, theoretical calculation not only isobar model for the elementary process but also how to calculate the cross section for the deuteron target. Finally, experimental results are discussed comparing with the calculations in Sect.4.4.

4.1 Experimental results

The angular distribution of the cross sections for K^0 in the laboratory frame after subtraction of background contributions is shown in Fig.4.1 for the photon energy regions of $0.9 < E_\gamma < 1.0$ and $1.0 < E_\gamma < 1.1$ GeV. As mentioned in Sect.3.10.1, we select the three regions, Reg1, Reg2 and Reg3 on the acceptance map. Therefore, the cross sections in Fig.4.1 are calculated by

$$\frac{d\sigma}{d\Omega} = \int_{E_{min}}^{E_{max}} dE_\gamma \int_{Reg1+Reg2+Reg3} \frac{d\sigma}{dpd\Omega} dp \quad [\mu b/sr * GeV].$$

where $\frac{d\sigma}{dpd\Omega}$ is calculated according to Eq. 3.1.

K^0 momentum spectra shown in Fig. 4.2 were obtained for each photon energy and angular region as follows

$$\frac{d\sigma}{dp} = \int_{E_{min}}^{E_{max}} dE_\gamma \int_{Reg1 \ or \ 2} \frac{d\sigma}{dpd\Omega} d\cos\theta \quad [\mu b/(GeV/c) * GeV].$$

In Fig. 4.1 and 4.2, both statistical and systematical errors are shown. It is assumed that systematic errors listed in Table 3.11 are collected by root mean square.

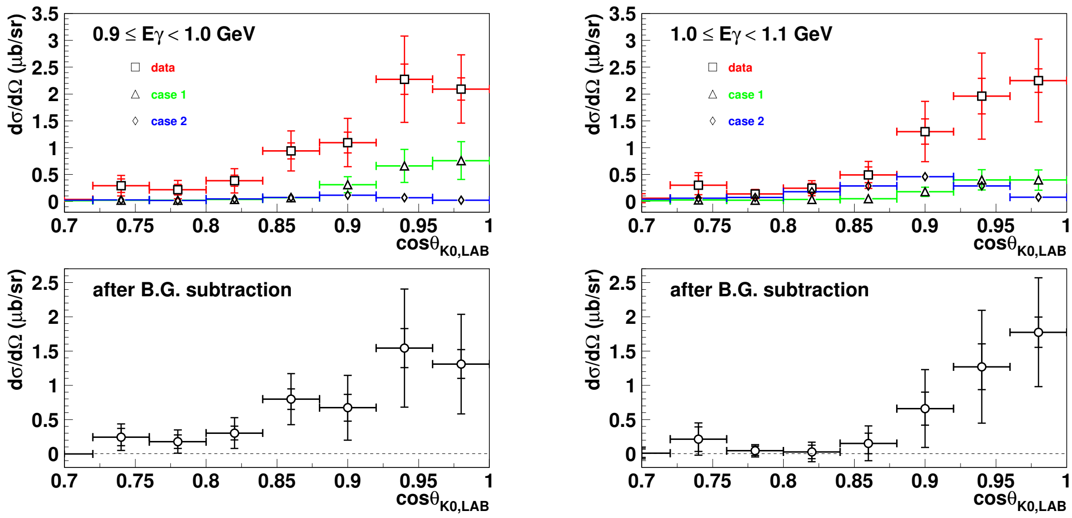

Figure 4.1: *Angular distributions of cross section in the photon energies from 0.9 to 1.0 GeV (left) and from 1.0 to 1.1 GeV (right), where square with red error bar is experimental data before subtraction of the background contributions, triangle with green error bar and diamond with blue error bar are the background from leakage from the target and from wrong combination, respectively, in upper figures. And lower figures show the results after subtraction of the background contributions. Error bars are overdrawn for (statistic) and (statistic + systematic) errors.*

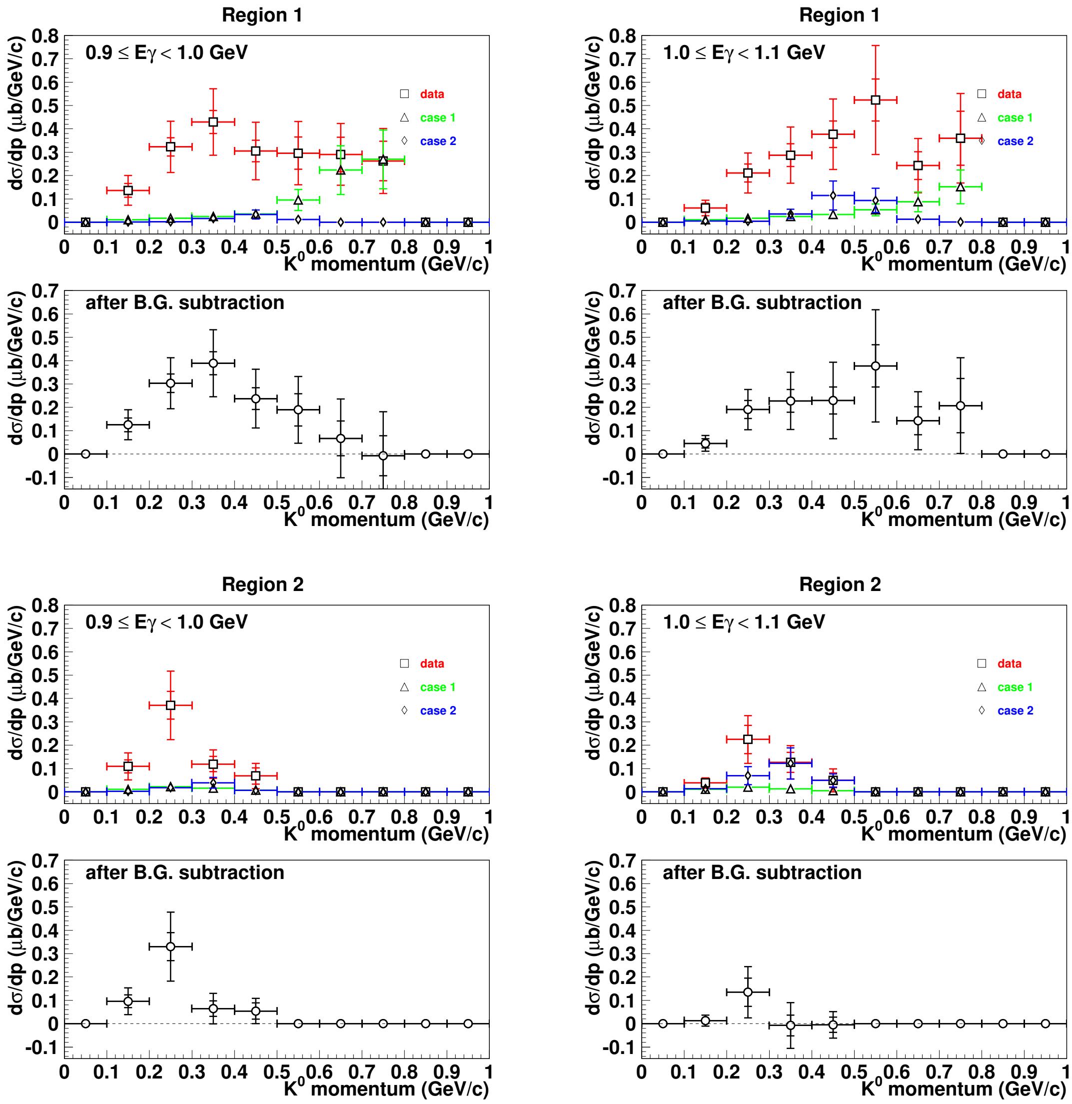

Figure 4.2: *Momentum dependence of the cross section in the photon energies from 0.9 to 1.0 GeV (left) and from 1.0 to 1.1 GeV (right), for Region 1 (upper group) and Region 2 (lower group), where square with red error bar is experimental data before subtraction the background contributions, triangle with green and diamond with blue error bar are the background from leakage from the target and from wrong combination, respectively. Squares with black error bars are results after subtraction of the background contributions. Error bars are overdrawn for (statistic) and (statistic + systematic) errors.*

4.2 Theoretical calculations

We measured the cross section of the inclusive process d(γ,K^0)Λ p in laboratory frame. The inclusive cross section on a deuteron according to the elementary models for kaon photoproduction should be calculated and compared with the present results. Firstly, the phenomenological models used in the present analysis are explained in Sect.4.2.1. In Section 4.2.2, the way of estimation of the K^0 photoproduction cross section is explained.

4.2.1 Isobar models

As mentioned in Sect. 1.1.2, two theoretical models, Kaon-MAID[2] and Saclay-Lyon A (SLA, [29]), are compared with our data in the present analysis.

Kaon-MAID

The Kaon-MAID model is one of the latest isobar models. This includes four nucleon resonances and two kaon resonances as intermediate state in resonance terms of s-channel and t-channel, respectively (Table 4.1). The resonance D_{13}, a candidate of missing resonances which have been not yet discovered experimentally but predicted by the constituent quark model, is added to reproduce the bump structure of the total cross section of $p(\gamma, K^+)$ reaction around $E_\gamma^{lab} = 1.5$ GeV taken by SAPHIR[16]. The hadronic form factors are introduced in the model according to the gauge invariance prescription[39].

SLA

The SLA is a simple version of the full Saclay-Lyon model[22], in which the nucleon resonances with spin $\frac{1}{2}$ and $\frac{5}{2}$ are excluded. The included resonances are one nucleon resonance in s-channel, two kaon resonances in t-channel and four hyperon resonances in u-channel (Table 4.1).

4.2.2 Calculation of K^0 photoproduction

The elementary cross section

The parameters in the isobar models are constrained by some symmetries. As mentioned in Sect. 1.1.2 (Eq. 1.1,1.2), the flavor SU(3) symmetry limits the main coupling constants as, $-4.5 < g_{K\Lambda p}/\sqrt{4\pi} < -3.0$ and $0.9 < g_{K\Sigma^0 p}/\sqrt{4\pi} < 1.3$.

Table 4.2 shows the particles associated each vertexes in Feynman diagrams. The fitting parameters are the main coupling constants, $g_{K\Lambda p}$, $g_{K\Sigma^0 p}$, and the products of photo-coupling and hadronic coupling constants for s-/u-/t-channels. For example, one of them is a coupling parameter $G_{N^*} = g_{N^* N\gamma} \cdot g_{K\Lambda N^*}/\sqrt{4\pi}$ for s-channel.

When the elementary cross section of the $K\Lambda$ channel (or a certain isospin channel) is calculated, we assume the isospin symmetry for hadronic coupling constants,

$$g_{K^+\Lambda p} = g_{K^0\Lambda n}$$

Table 4.1: *The conditions of Kaon-MAID and Sacray-Lyon A.*

particle	mass (MeV/c^2)	$I(J^P)$	Kaon-MAID	SLA
$N^*(1650)$, S_{11}	1640 to 1680	$\frac{1}{2}(\frac{1}{2}^-)$	○	×
$N^*(1710)$, P_{11}	1680 to 1740	$\frac{1}{2}(\frac{1}{2}^+)$	○	×
$N^*(1720)$, P_{13}	1650 to 1750	$\frac{1}{2}(\frac{3}{2}^+)$	○	○
$N^*(1900)$, D_{13}	~ 1900	$\frac{1}{2}(\frac{3}{2}^-)$	○	×
$K^*(892)$	891.66 ± 0.5	$\frac{1}{2}(1^-)$	○	○
$K_1(1270)$	1273 ± 7	$\frac{1}{2}(1^+)$	○	○
$\Lambda(1405)$, S_{01}	1406.5 ± 4.0	$0(\frac{1}{2}^-)$	×	○
$\Lambda(1670)$, S_{01}	1660 to 1680	$0(\frac{1}{2}^-)$	×	○
$\Lambda(1810)$, P_{01}	1750 to 1850	$0(\frac{1}{2}^+)$	×	○
$\Sigma(1660)$, P_{11}	1630 to 1690	$1(\frac{1}{2}^+)$	×	○
hadronic form factor and contact term			○	×
Input data				
$K^+\Lambda$			○	○
$K^+\Sigma^0$			○	×
$K^0\Sigma^+$			○	×

Table 4.2: *Associated particles at vertices in tree level Feynman diagrams except for Born terms. For each reaction, upper ones show the photo-couplings, while lower ones show the hadronic couplings.*

reaction	s-channel	t-channel	u-channel
$p(\gamma, K^+)\Lambda$	$(N^{*+}p\gamma)$ $(K^+\Lambda N^{*+})$	$(K^{*+}K^+\gamma), (K_1^+K^+\gamma)$ $(K^{*+}\Lambda p), (K_1^+\Lambda p)$	$(\Lambda^*\Lambda\gamma), (\Sigma^0\Lambda\gamma), (\Sigma^{*0}\Lambda\gamma)$ $(K^+\Lambda^* p), (K^+\Sigma^0 p), (K^+\Sigma^{*0} p)$
$n(\gamma, K^0)\Lambda$	$(N^{*0}n\gamma)$ $(K^0\Lambda N^{*0})$	$(K^{*0}K^0\gamma), (K_1^0K^0\gamma)$ $(K^{*0}\Lambda n), (K_1^0\Lambda n)$	$(\Lambda^*\Lambda\gamma), (\Sigma^0\Lambda\gamma), (\Sigma^{*0}\Lambda\gamma)$ $(K^0\Lambda^* n), (K^0\Sigma^0 n), (K^0\Sigma^{*0} n)$

$$\begin{aligned} g_{K^+\Sigma^0 p} = -g_{K^0\Sigma^0 n} &= g_{K^0\Sigma^+ p}/\sqrt{2} = g_{K^+\Sigma^- n}/\sqrt{2} \\ g_{K^+\Sigma^0\Delta^+} = g_{K^0\Sigma^0\Delta^0} &= -\sqrt{2}g_{K^0\Sigma^+\Delta^+} = \sqrt{2}g_{K^+\Sigma^-\Delta^0}. \end{aligned}$$

Following Ref.[40], helicity amplitudes given by the Particle Data Group[41] can be written in terms of electromagnetic coupling constants for resonances. For spin $\frac{1}{2}$ resonances only a magnetic transition is possible, and for spin $\frac{3}{2}$ resonances two couplings can contribute. Namely,

$$\frac{g_{N^{*0}n\gamma}}{g_{N^{*+}p\gamma}} = \frac{A^n_{1/2}}{A^p_{1/2}} \quad (\text{ for spin } \tfrac{1}{2})$$

$$\left.\begin{array}{l} \dfrac{g^{(1)}_{N^{*0}n\gamma}}{g^{(1)}_{N^{*+}p\gamma}} = \dfrac{\sqrt{3}A^n_{1/2} \pm A^n_{3/2}}{\sqrt{3}A^p_{1/2} \pm A^p_{3/2}} \\ \dfrac{g^{(2)}_{N^{*0}n\gamma}}{g^{(2)}_{N^{*+}p\gamma}} = \dfrac{\sqrt{3}A^n_{1/2} - (m_N/m_{N^*})A^n_{3/2}}{\sqrt{3}A^p_{1/2} - (m_N/m_{N^*})A^p_{3/2}} \end{array}\right\} \quad (\text{ for spin } \tfrac{3}{2})$$

where A^N_s means the helicity amplitude of nucleon (N) with spin-s.

From the relations above, the couplings in s-channel and u-channel can be converted from those for $K^+\Lambda$ to $K^0\Lambda$ channel.

On the other hands, it is not so easy for t-channel diagrams. The decay width of kaon resonances are written as the following equation,

$$\Gamma_{K'\to K\gamma} = \frac{1}{24}\frac{|g_{K'K\gamma}|^2}{4\pi M^2}\left(m_{K'}\left(1-\frac{m_K^2}{m_{K'}^2}\right)\right)^3$$

where K' means K^* and K_1, and $M = 1$ GeV is a normalized factor to make $g_{K'K\gamma}$ dimensionless. For both charged and neutral K^*, the decay widths are well known[41]. Therefore ratio of couplings can be deduced as

$$r_{K^*K\gamma} = \frac{g_{K^{*0}K^0\gamma}}{g_{K^{*+}K^+\gamma}} = -\sqrt{\Gamma_{K^{*0}\to K^0\gamma}/\Gamma_{K^{*+}\to K^+\gamma}} = -1.53$$

where the sign is decided from the quark model prediction. However, since the decay widths of K_1 are not well known, $r_{K_1K\gamma}$ should be a free parameter to be derived from data.

For Kaon-MAID, since the set of parameters were fitted simultaneously by the $K^+\Lambda$, $K^+\Sigma^0$ and $K^0\Sigma^+$ data, it can predict the K^0 photoproduction under the conditions mentioned above. The ratio $r_{K_1K\gamma}$ was determined to be -0.4474 by fitting the $K\Sigma$ data.

For SLA, however, the parameters were adjusted from only $K^+\Lambda$ production data, and so the ratio of the charged and neutral K_1 ($r_{K_1K\gamma}$) could not be determined. Therefore, when $K^0\Lambda$ production is calculated with SLA, $r_{K_1K\gamma}$ should be considered as a free parameter.

The cross section on the deuteron target

The differential cross section of K^0 photoproduction on the deuteron target is calculated by Bydžovský et al. using a simple model based on the impulse approximation in which a proton acts as a spectator[42]. The reason why this approach neglects the final sate interaction (FSI) is justified by following. Since the parameters are determined from K^+Y production on proton, the FSI effect of KΛ is included in the coupling constants of the elementary amplitude. Besides the KN interaction is weak in the hadronic scale. In addition, the Λ N interaction is not so important for the inclusive d(γ,K^+)Λ n reaction near the threshold[43], and the nature of the FSI in the K^+ and K^0 production is considered to be not so different.

The kinematics to be calculated is

$$\gamma(P_\gamma,\lambda) + d(P_d,\mu) \to K(P_K) + \Lambda(P_\Lambda,\eta') + N'(P_{N'},\xi')$$

where P's are 4-momenta and $\lambda, \mu, \eta', \xi'$ are spins of γ, d, Λ and N', respectively.

Then, the first-order of the S-matrix is

$$S_{fi} = i(2\pi)^4\delta^4(P_f - P_i)M_{fi}\sqrt{\left(\frac{1}{2E_\gamma V}\right)\left(\frac{1}{2E_d V}\right)\left(\frac{1}{2E_K V}\right)\left(\frac{m_\Lambda}{E_\Lambda V}\right)\left(\frac{m_{N'}}{E_{N'} V}\right)}$$

where $P_i = P_\gamma + P_d$ and $P_f = P_K + P_\Lambda + P_{N'}$, V is the volume in which the reaction occurs. The cross section in a general reference frame is

$$\begin{aligned} d^9\sigma &= \frac{1}{6}\sum_{spin}|S_{fi}|^2\frac{d^3p_K V}{(2\pi)^3}\frac{d^3p_\Lambda V}{(2\pi)^3}\frac{d^3p_{N'} V}{(2\pi)^3}/\left(T\ v_{rel}/V\right) \\ &= \frac{1}{(2\pi)^5}\frac{m_\Lambda m_{N'}}{8P_\gamma\cdot P_d E_K E_\Lambda E_{N'}}\delta^4(P_f - P_i)\frac{1}{6}\sum_{spin}|M_{fi}|^2 d^3P_K d^3p_\Lambda d^3p_{N'} \end{aligned}$$

where T is the reaction time, v_{rel} is the relative velocity between the incident and the target particle and the factor 1/6 arises from spin average of the incident photon and deuteron. Up to here, it is a general formula.

In the *spectator approximation*, it can be written as

$$\begin{aligned} d^9\sigma &= \frac{1}{(2\pi)^5}\frac{m_\Lambda m_{N'}}{8P_\gamma\cdot P_d E_K E_\Lambda E_{N'}}\int d^4P_N\delta^4(P_f^e - P_i^e)4\pi\frac{(s-m_N^2)^2}{m_\Lambda m_N}\frac{d\sigma^{ele}}{dt} \\ &\quad\times\delta^4(P_d - P_N - P_{N'})\frac{\frac{1}{6}\sum|M_{fi}|^2}{\frac{1}{4}\sum|M_{fi}^{ele}|^2}d^3P_K d^3p_\Lambda d^3P_{N'} \end{aligned}$$

where the integrated value of P_N is the four-momentum of the target, the δ function is separated into two parts, and the separated elementary cross section

$$\frac{d\sigma^{ele}}{dt}(s,t) = \frac{1}{4\pi}\frac{m_N m_\Lambda}{(s-m_N^2)^2}\frac{1}{4}\sum_{\lambda\xi\eta'}|M_{fi}^{ele}|^2$$

is introduced. The $s = (P_\gamma + P_N)^2$ and $t = (P_\gamma - P_K)^2$ are the Mandelstam variables. The kinematics of the elementary process is

$$\gamma(P_\gamma, \lambda) + N(P_N, \xi) \to K(P_K) + \Lambda(P_\Lambda, \eta')$$

After some algebra, spin averaged matrix element can be expressed as

$$\frac{1}{6}\sum|M_{fi}|^2 = (2\pi)^3\frac{2m_d E_{N'}}{E_N}\frac{1}{4}\sum|M_{fi}^{ele}|^2 u_d(p_{N'})^2$$

where $u_d(p_{N'})$ is the wave function of the deuteron, the expression for the differential cross section in the laboratory frame is

$$\frac{d^3\sigma}{d|\vec{p}_K|d\Omega} = \int\frac{m_{N'}(s-m_N^2)^2\vec{p}_K^2|\vec{p}_{N'}|}{4m_N E_\gamma E_K E_N|\vec{p}_\gamma - \vec{p}_K|}\frac{u_d(p_{N'})^2}{\pi}\frac{d\sigma^e}{dt}d|\vec{p}_{N'}|d\Phi'_{N'}.$$

where Φ is the azimuthal angle of the spectator nucleon. The isospin formalism, $m_n = m_p$, is assumed and the isospin factor $\sqrt{2}$ is multiplied to take account of the antisymmetrization of two nucleons in the intermediate state. The energy of the target nucleon is given by $E_N = E_d - E_{N'} = E_K + E_\Lambda - E_\gamma$ for off-shell approximation and by $E_N = \sqrt{m_N^2 + \vec{p}_N^2}$ for on-shell approximation, and the effective mass of the target nucleon is taken to be consistent with kinematics, $m_N = \sqrt{P_N^2}$, $\vec{p}_N = -\vec{p}_{N'}$.

In this calculations non relativistic Bonn OBEPQ (one-boson-exchange-potential in q-space) deuteron wave function [44] is used to the neutron distribution.

Angular and momentum distribution

Figure 4.3 and 4.4 show the results of the theoretical calculations of the differential cross section on the deuteron targets.

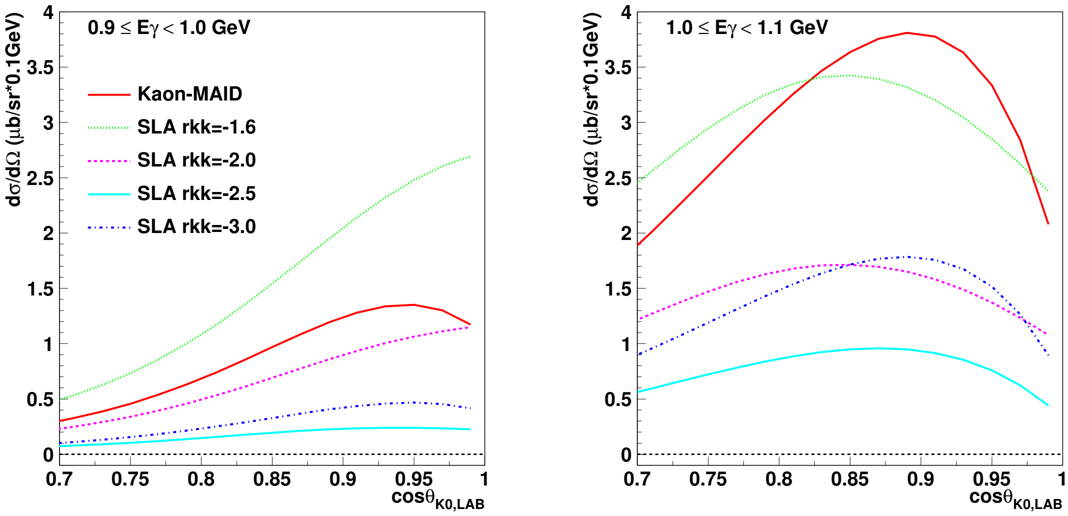

Figure 4.3: *Laboratory angular distribution of the calculations in the region* $0.7 \leq \cos\theta < 1.0$. *and in the photon energy region* $0.9 \leq E_\gamma < 1.0$ *(left) and* $1.0 \leq E_\gamma < 1.1$ *(right). The lines represent the calculations using Kaon-MAID (solid), SLA (*$r_{K_1K\gamma}$ $=-1.6$*, dotted), SLA (*$r_{K_1K\gamma}$ $=-2.0$*, dashed), SLA (*$r_{K_1K\gamma}$ $=-2.5$*, solid) and SLA (*$r_{K_1K\gamma}$ $=-3.0$*, dash-dotted). The values are averaged each 0.02 bin and connected by line.*

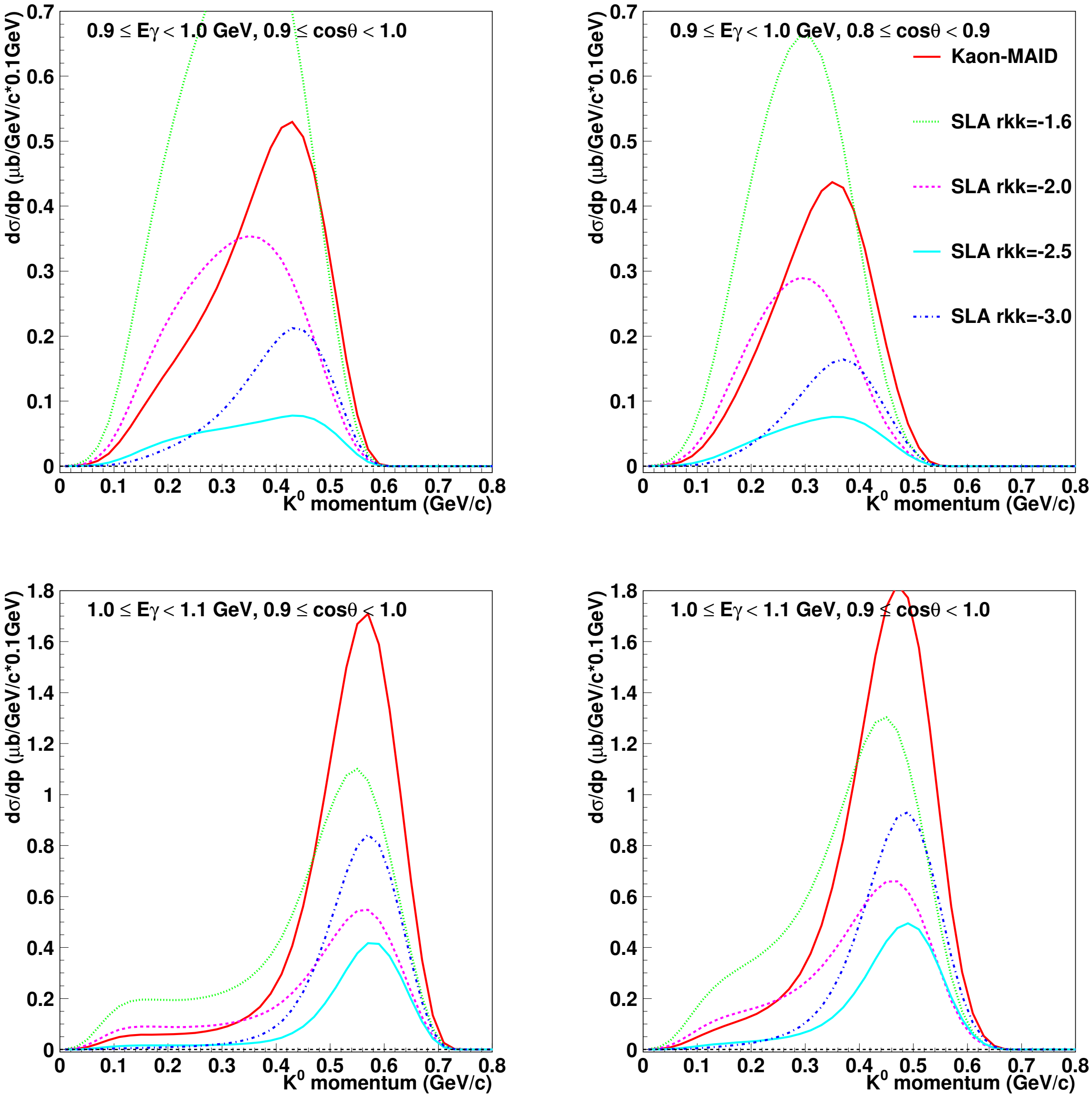

Figure 4.4: *Momentum spectra of calculations in the region* $0.8 \le \cos\theta < 0.9$ *(right) and* $0.9 \le \cos\theta < 1.0$ *(left) and in the photon energy region* $0.9 \le E_\gamma < 1.0$ *(upper) and* $1.0 \le E_\gamma < 1.1$ *(lower). The lines represent the calculations using Kaon-MAID (solid), SLA (*$r_{K_1K\gamma}$ $=-1.6$*, dotted), SLA (*$r_{K_1K\gamma}$ $=-2.0$*, dashed), SLA (*$r_{K_1K\gamma}$ $=-2.5$*, solid) and SLA (*$r_{K_1K\gamma}$ $=-3.0$*, dash-dotted). The values are averaged each 0.02 GeV/c bin and connected by line.*

4.3 Comparison

Figure 4.5 shows the relation of the NKS acceptance region to the kinematical distribution using Kaon-MAID and SLA($r_{K_1K\gamma}$ =−1.6). For higher photon energy, the kinematical region tends to move away from the acceptance region of NKS. The Region 1 covers more than 97% of the area of $0.9 \leq \cos\theta_{Lab} < 1.0$. for both models and energy regions. However, the efficiency of the Region 2 extremely changes with the photon energy.

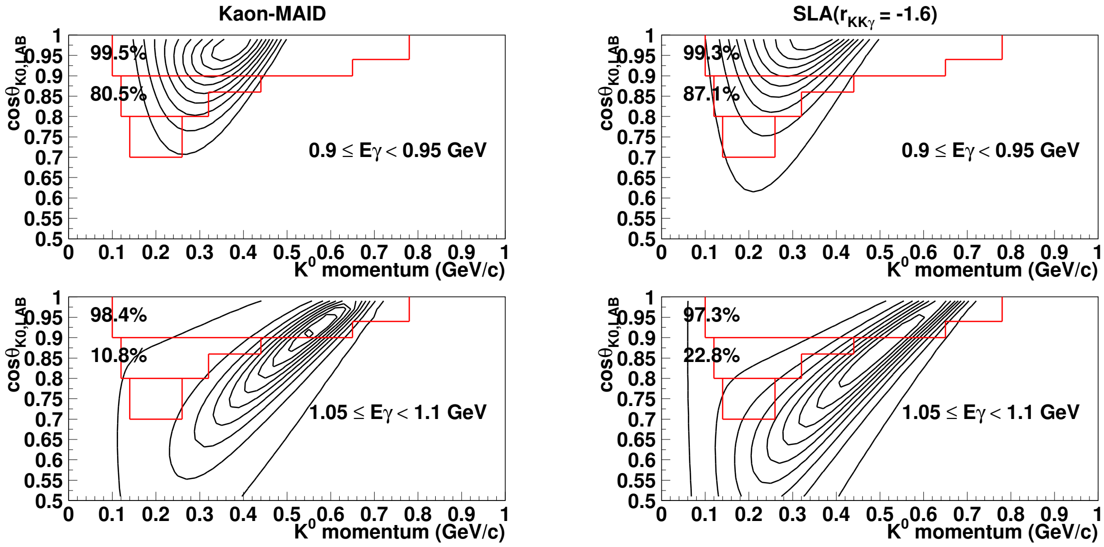

Figure 4.5: *Comparison between the effective region of NKS acceptance and theoretical calculations, Kaon-MAID (left) and SLA($r_{K_1K\gamma}$ = −1.6) (right). Red lines represent the accepted region. The values mean the efficiencies of Region 1 and 2.*

Angular distribution

Figure 4.6 show the angular distributions in the laboratory frame. Theoretical calculation are also drawn. The rugged structure of the theoretical calculation is due to the shape of the effective region on the acceptance map of NKS. The region cuts are also applied to the theoretical calculations. For the photon energy region from 0.9 to 1.0 GeV, the magnitude of the cross sections from Kaon-MAID and SLA($r_{K_1K\gamma}$ =−2.0 or −3.0) are almost consistent with our data. However, for the region from 1.0 to 1.1 GeV, the estimation from Kaon-MAID seems to be large.

Momentum dependence

Figure 4.7 show the momentum dependence in the laboratory frame and the results of the calculations are also overdrawn. For the photon energy region from 0.9 to 1.0 GeV, Kaon-MAID and SLA($r_{K_1K\gamma}$ =−2.0) give almost consistent results with the data.

However for the region from 1.0 to 1.1 GeV, the calculations from Kaon-MAID or SLA($r_{K_1K\gamma}$ =-1.6,-3.0) overestimate the cross section at the higher momentum region.

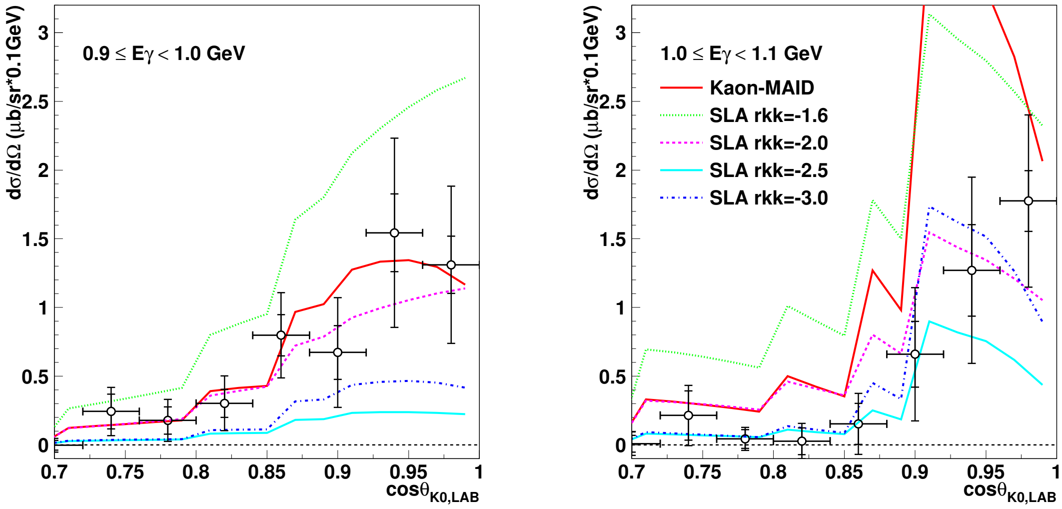

Figure 4.6: *Laboratory angular distribution of the data and the calculations in Region 1 to 3. The lines represent the calculations using Kaon-MAID(solid), SLA($r_{K_1K\gamma}$ =−1.6, dotted), SLA($r_{K_1K\gamma}$ =−2.0, dashed) , SLA($r_{K_1K\gamma}$ =−2.5, solid) and SLA($r_{K_1K\gamma}$ =−3.0, dash-dotted). Since these values are averaged each 0.02 bin and connected by line. Error bars are overdrawn as (statistic) and (statistic + systematic).*

From Fig.4.5, since the peak of the yield distribution crosses the edge of the effective acceptance region in Region 2, the spectrum is easily influenced by any conditions , e.g. the resolution of K^0 kinematics or photon energy. A reliable comparison may be performed only in Region 1. Therefore, the calculations are compared with data only in Region 1 in this section. The figures of the comparison for Region 2 are shown in Appendix C.

In Region 1 at photon energy from 0.9 to 1.0 GeV, Kaon-MAID and SLA with $r_{K_1K\gamma}$ of about −2 seem to explain the magnitude of the data. However, the shape of the momentum spectrum from Kaon-MAID is larger at higher momentum than that of the data, and the shape from SLA is more consistent with the data if $r_{K_1K\gamma}$ =−2.0. Furthermore, at photon energy from 1.0 to 1.1 GeV, Kaon-MAID and SLA with $r_{K_1K\gamma}$ more than -2.0 or less than -2.5 are too large. The χ^2 function calculated as

$$\chi^2 = \frac{1}{\#data - 1} \sum_i \left(\frac{(d\sigma/dp)^{th} - (d\sigma/dp)^{exp}}{\Delta(d\sigma/dp)^{exp}} \right)^2$$

are shown in Fig.4.8.

It was found that the χ^2 of SLA had a minimum value at $r_{K_1K\gamma} = -2.0 \sim -2.5$.

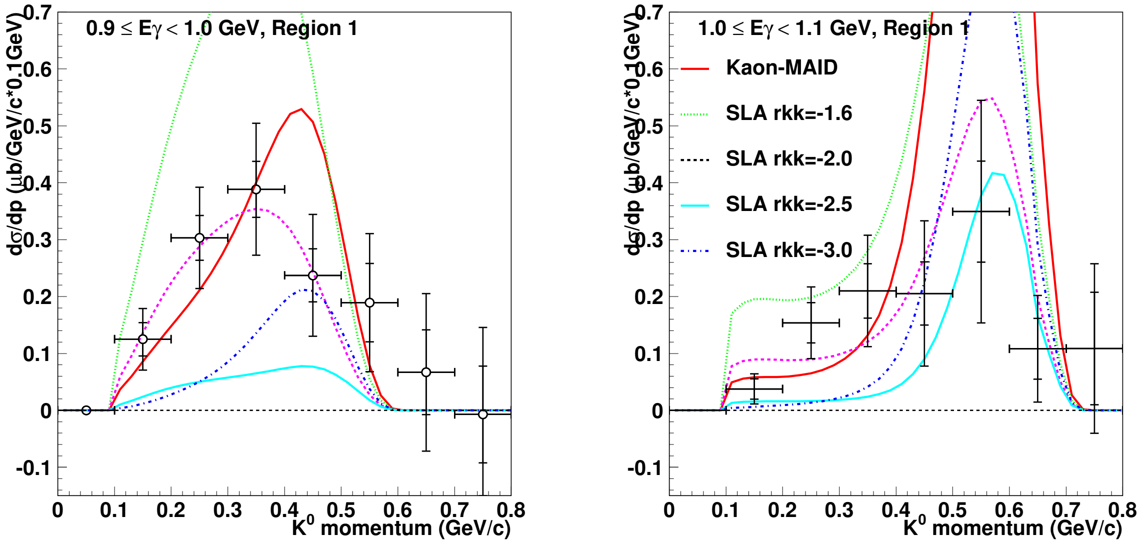

Figure 4.7: *Momentum dependence after correction for efficiencies. The photon energy range is* $0.9 < E_\gamma < 1.0$ *(left) and* $1.0 < E_\gamma < 1.1$ *(right). Backgrounds from case 1 and case 2 are subtracted. Error bars are overdrawn for the (statistic) and (statistic + systematic) errors.*

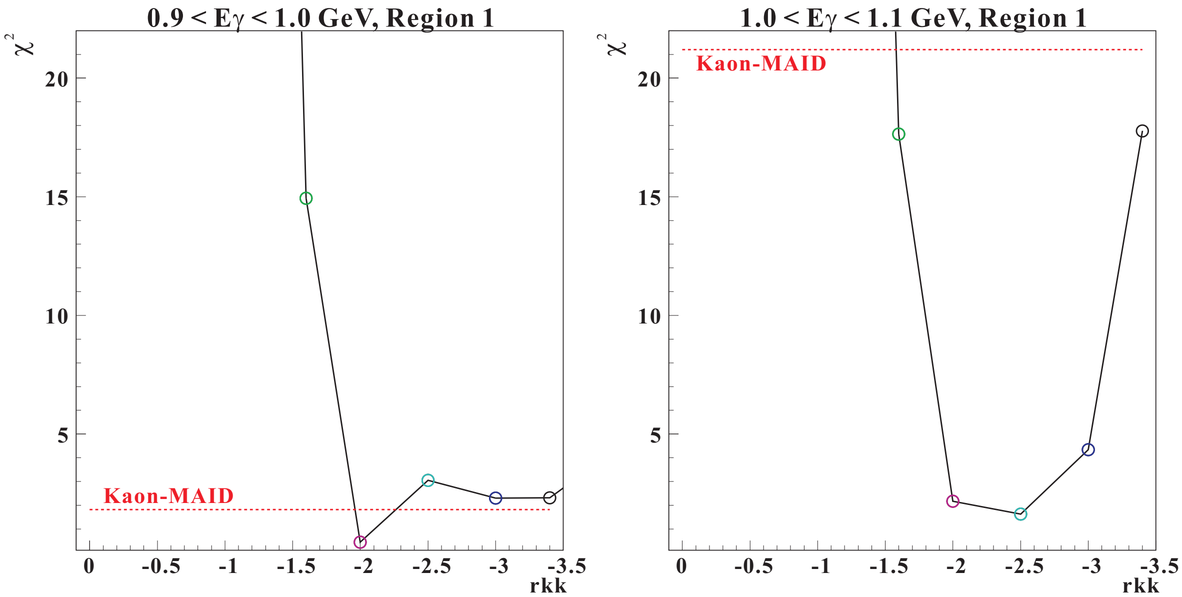

Figure 4.8: *The values of the* χ^2 *function which was calculated for the non-zero data points at Region 1 at photon energy from 0.9 to 1.0 GeV (left) and 1.0 to 1.1 GeV (right). The horizontal axis mean the value of the* $r_{K_1 K\gamma}$ *for SLA. Solid lines mean the* χ^2 *of Kaon-MAID.*

4.4 Discussion

The contribution of Σ production

Since we measured only K^0, Σ production processes, that is $p(\gamma, K^0)\Sigma^+$ and $n(\gamma, K^0)\Sigma^0$, may contribute in addition to $K^0\Lambda$ production. The contributions of the Σ production are calculated by the Kaon-MAID using the on-shell approximation and shown in Fig.4.9. Because the FSI effects are not included in the present calculation, there are no rescattering effects. Therefore, the $K^0\Lambda$ and $K^0\Sigma$ channels are not coupled together. The total inclusive cross section is then given by a sum of the cross sections of the three channels: $\sigma = \sigma(K^0\Lambda) + \sigma(K^0\Sigma^0) + \sigma(K^0\Sigma^+)$. Although the difference between the on-shell and the off-shell calculation is 30 − 40 % in the photon energy region from 0.9 to 1.0 GeV and less than 10 % in the photon energy region from 1.0 to 1.1 GeV, respectively, the contribution of the Σ production is considered to be the same for both the on-shell and the off-shell calculations.

The cross section of the Σ production is less than 10 % to the that of the Λ production in the photon energy region from 0.9 to 1.0 GeV. Since it is enough smaller than the error of the present data, the contribution from Σ production process is considered to be negligible.

In the photon energy region from 1.0 GeV to 1.1 GeV, since the contribution is large, it is not negligible, especially, in lower momentum region. However, even if the contribution from Σ production for SLA is the same with that for Kaon-MAID, SLA with $r_{K_1K\gamma}$ of -2.0 can explain the present data.

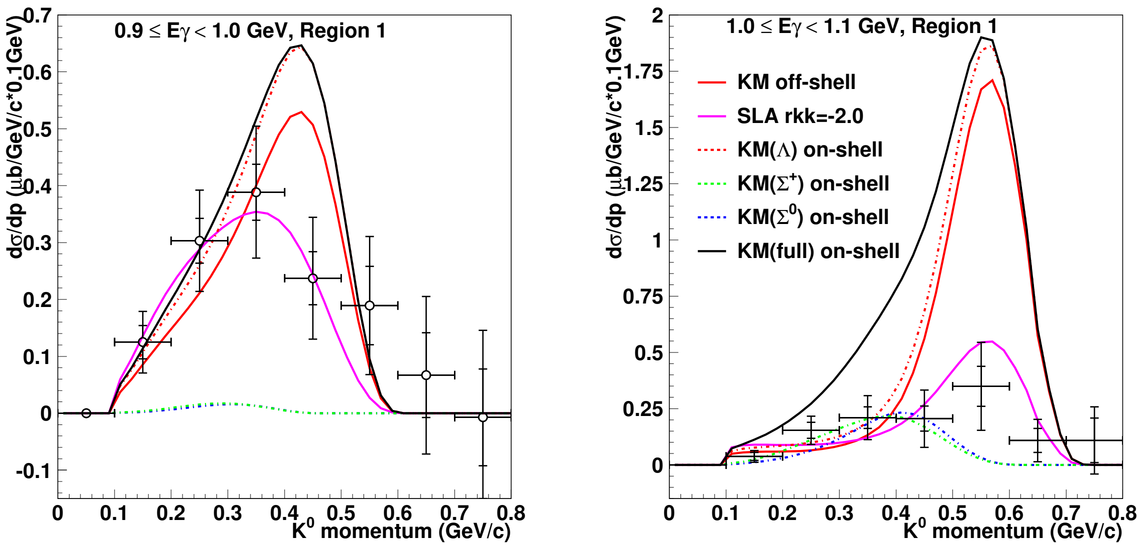

Figure 4.9: *The contribution of the Sigma production in the Kaon-MAID. The photon energy range is* $0.9 < E_\gamma < 1.0$ *(left) and* $1.0 < E_\gamma < 1.1$ *(right). KM means the Kaon-MAID and KM(full) = KM(Λ) + KM(Σ^+) + KM(Σ^0).*

The ambiguity of the photon energy

As mentioned in Sect. 3.3.2, the photon energy had systematic error of $\binom{+10}{-16}$ MeV. Therefore, the results assuming that the photon energy region was shifted by 10 MeV and 20 MeV are shown in Fig. 4.10. SLA with $r_{K_1K\gamma}=-2.0$ can reproduce the present data well in the both photon energy regions even if the ambiguity of the photon energy of ± 20 MeV is considered. On the other hand, Kaon-MAID can reproduce the present data in the photon energy from 0.9 to 1.0 GeV but gives too large estimation in the photon energy from 1.0 GeV to 1.1 GeV even if the shift of -20 MeV of the photon energy is assumed,

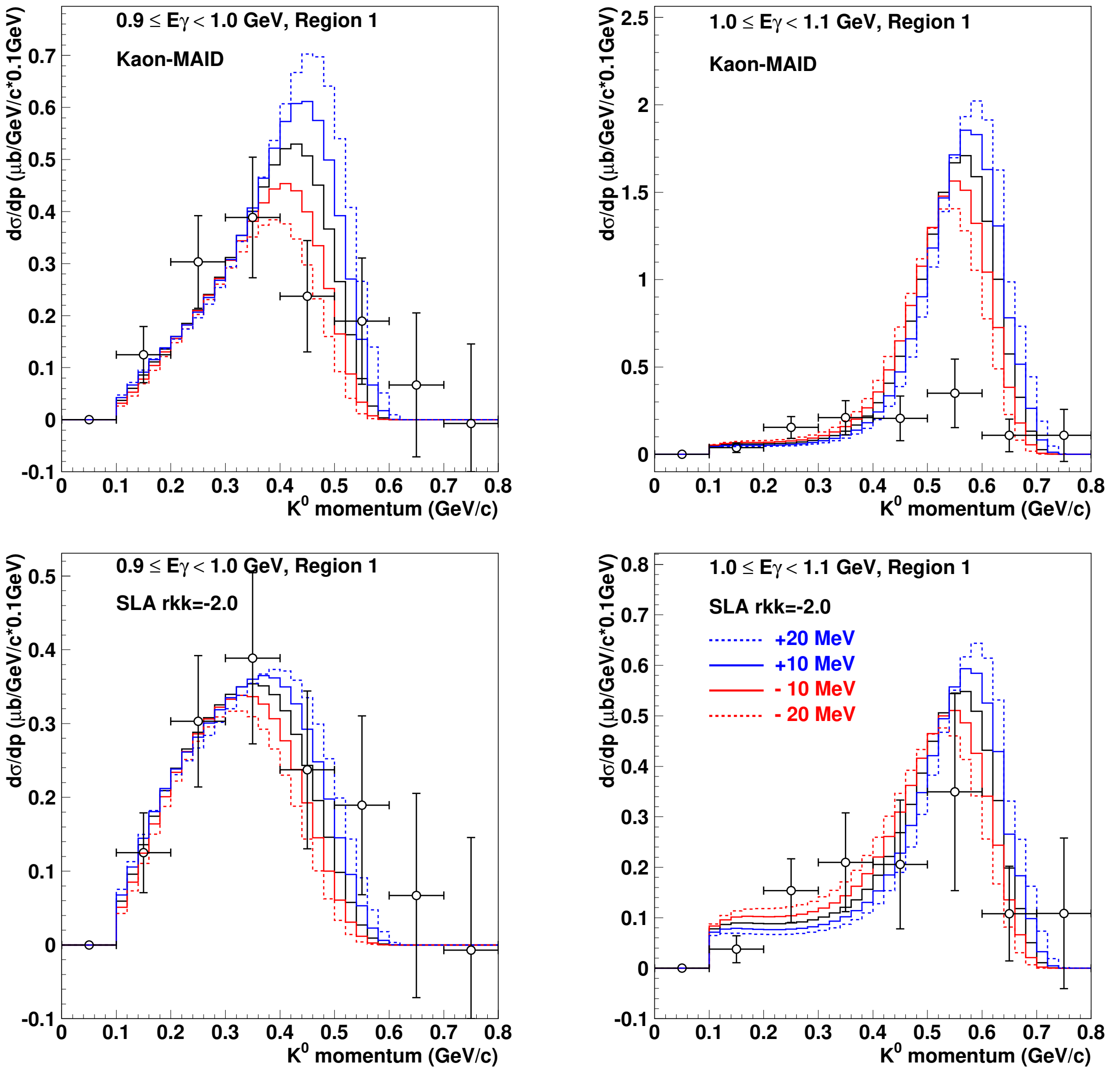

Figure 4.10: *The ambiguity of the photon energy in the calculation using Kaon-MAID (upper) and SLA with $r_{K_1K\gamma}$ of -2.0 (lower). In left figures, the values were integrated over the photon energy region from 0.9 to 1.0 GeV (black solid line), from 0.91 to 1.01 GeV (blue solid line), from 0.92 to 1.02 GeV (blue dashed line), from 0.89 to 0.99 GeV (red solid line) and from 0.88 to 0.98 GeV (red dashed line), respectively. In right figures, the values were integrated around the energy region from 1.0 to 1.1 GeV.*

Elementary cross section

In most reliable region, that is in Region 1 at the photon energy from 0.9 to 1.0 GeV, Kaon-MAID and SLA with $r_{K_1K\gamma}$ =−2.0 can explain the magnitude of the differential cross section of the present data.

However, at the photon energy from 1.0 to 1.1 GeV, Kaon-MAID is too large. Fig. 4.11 shows energy dependence of the total cross section of K^0 photoproduction using Kaon-MAID and SLA with some $r_{K_1K\gamma}$ value.

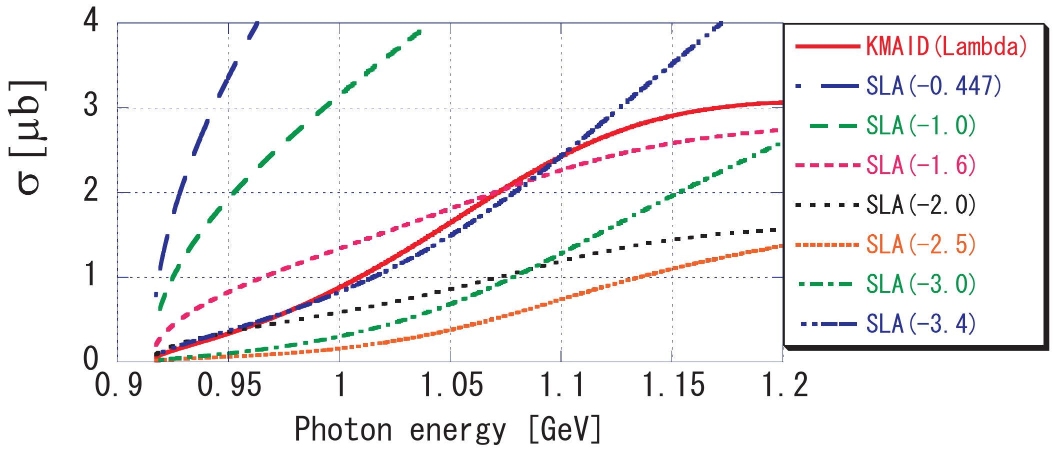

Figure 4.11: *Energy dependence of the total cross section of K^0 photoproduction. Kaon-MAID and SLA with $r_{K_1K\gamma}$ of -0.447 are already shown in Fig. 1.3.*

Figure 4.12 shows the elementary differential cross section in center of mass system using Kaon-MAID and SLA with various $r_{K_1K\gamma}$ at photon energy of 0.95 and 1.05 GeV.

The difference of the shape of the momentum spectra between Kaon-MAID and SLA with $r_{K_1K\gamma}$ of −2.0 at the photon energy from 0.9 to 1.0 GeV is caused by the angular distribution in the center of mass system. On the other hand, at the photon energy from 1.0 to 1.1 GeV, the origin of the difference of the momentum spectra is not the angular distribution but the magnitude of the cross section. As mentioned in Sect. 1.2, because no charge is involved in the $n(\gamma, K^0)\Lambda$ reaction, Born term in t-channel does not contribute. Therefore, if we assume a simple model using only Born term for the kaon photoproduction, it is naturally considered that the angular distribution for the $n(\gamma, K^0)\Lambda$ reaction is backward peak due to the absence of t-channel. As shown in Fig. 4.12, the angular distribution of Kaon-MAID is 90 degree peak and those of SLAs with $r_{K_1K\gamma}$ larger than −2.5 are backward peak. From the definition of $r_{K_1K\gamma}$, when the absolute of $r_{K_1K\gamma}$ is large, the contribution of the K_1 exchange term in t-channel also becomes large to suppress the backward peak.

Hence, SLA can be used as a probe to investigate the elementary cross section of $n(\gamma, K^0)\Lambda$ reaction, and it is found that the angular distribution of $n(\gamma, K^0)\Lambda$ reaction in center of mass system is backward peak.

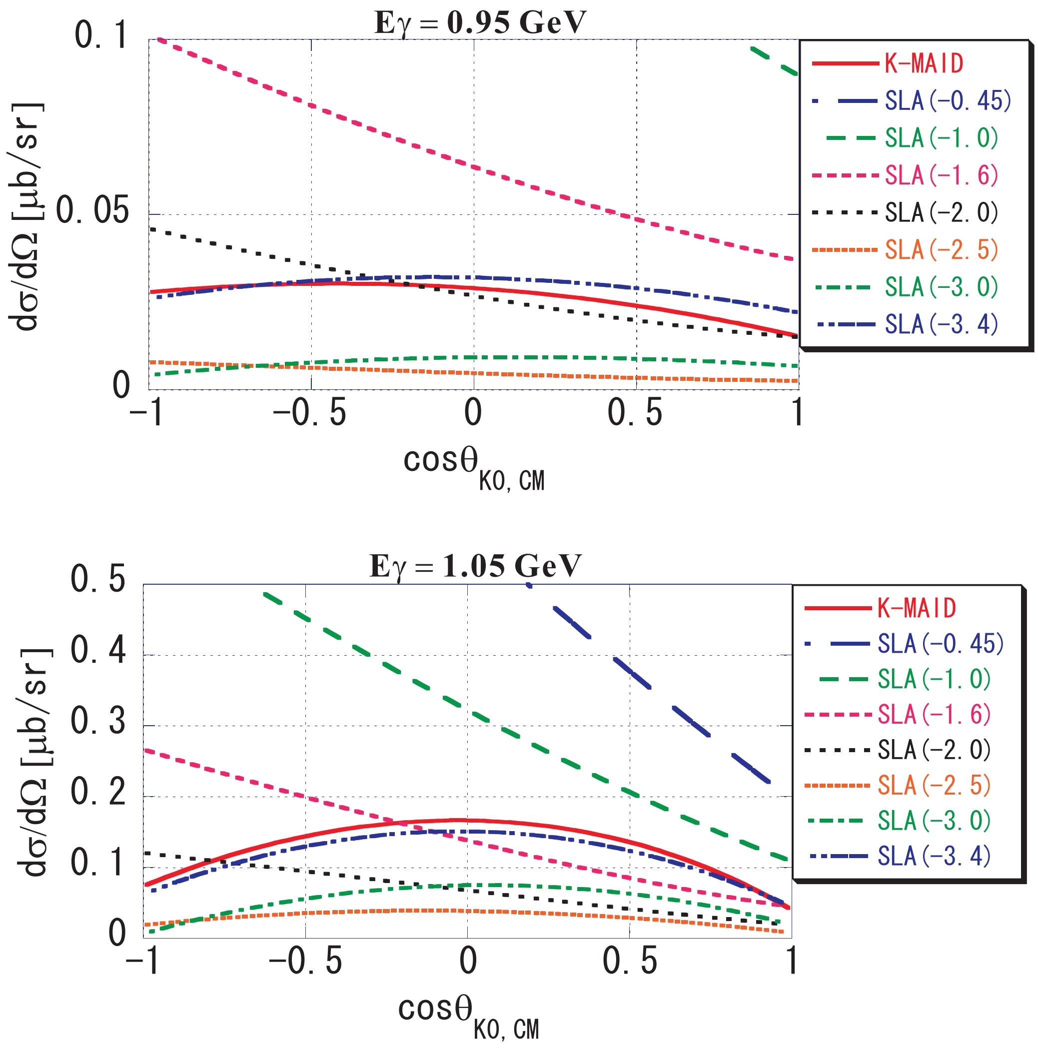

Figure 4.12: *The angular distribution of differential elementary cross sections in center of mass system of* K^0 *photoproduction using Kaon-MAID and SLA with some values of* $r_{K_1K\gamma}$ *in photon energy region from 0.9 to 1.0 GeV (upper) and from 1.0 to 1.1 GeV (lower). When* $r_{K_1K\gamma} \geq -2.5$*, the distribution has a backward peak.*

Chapter 5

Summary and conclusion

For the investigation of strangeness photoproduction, the $n(\gamma, K^0)\Lambda$ reaction has important and unique features.

We have measured the K^0 photoproduction on a deuteron in the threshold region following the measurement of quasi-free process using a carbon target[34]. The experiment was carried out at Laboratory of Nuclear Science, Tohoku University which provides tagged photon beams in the region of threshold energy from 0.8 to 1.1 GeV. A liquid deuteron target system was constructed and its density was kept stable to be about 0.17 g/cm^2 during the data taking. K^0's were detected by the Neutral Kaon Spectrometer via the $\pi^+\pi^-$ decay channel. The resolution of the $\pi^+\pi^-$ invariant mass spectrum was found to be about 15 MeV/c^2. About 600 K^0's were measured during the 1000 hours data taking.

The angular and momentum distributions were obtained and compared with the latest two theoretical model calculations by convoluting the acceptance of the NKS. The calculations were carried out by Bydžovský et al. in the spectator approximation using the realistic deuteron wave function. Although the Kaon-MAID model can calculate the $K^0\Lambda$ channel in its framework, the SLA model has free parameter ($r_{K_1K\gamma}$: ratio of the photo coupling constants of neutral and charged K_1) for the $K^0\Lambda$ channel. Therefore, the calculation was carried out by SLA using various $r_{K_1K\gamma}$ values. The results from SLA with various $r_{K_1K\gamma}$ can be used as a probe to investigate the elementary cross section of $n(\gamma, K^0)\Lambda$ reaction.

Both models could roughly explain the magnitude and the shape of the data in the photon energy region from 0.9 to 1.0 GeV. However, Kaon-MAID gave a large result in the photon energy region from 1.0 to 1.1 GeV. The most reasonable calculation was provided by SLA with $r_{K_1K\gamma} = -2.0$. This result implies that the angular distribution of K^0 in CM system is backward peak.

Appendix A

Liquid deuterium

number of neutron is estimated as following formula

$$
\begin{aligned}
N &= \int L(x,y)\rho_n I(x,y)dS \\
L(x,y) &= W + 2\times(\sqrt{l^2-(x^2+y^2)} - l + d) \\
l &= \frac{d^2+R^2}{2d} \\
I(x,y) &= \frac{1}{2\pi\sigma^2}\exp\left(-\frac{(x-x_0)^2+(y-y_0)^2}{2\sigma^2}\right) \\
\rho_n &= \frac{N_A}{M_{D_2}}\times 2\times\rho_{D_2}\ [cm^{-3}] \\
\text{avogadro number} : N_A &= 6.02\times 10^{23}\ [mol^{-1}]\ ,\ M_{D_2} = 2.014\times 2\ [g/mol] \\
\text{cell width} : W &= 30mm\ ,\ \text{radius of windows} : R = 20mm \\
\text{beam size} : \sigma &= 5mm \\
\text{deuteron density} : \rho_{D_2} &= 0.168\ ,\ 0.173\ [g/cm^3] \\
\text{off set} : y_0 &= 0\ ,\ x_0 = 0 \sim 10mm\ \text{ by 1mm} \\
\text{expansion} : d &= 1.0\ ,\ 1.5\ ,\ 2.0\ ,\ 2.5\ ,\ 3.0mm
\end{aligned}
$$

where $L(x,y)$ is the width of the cell including the expansion , l is the radius assuming the expansion as a circle and $I(x,y)$ is the distibution of the photon beam. Since the fluctuation of the beam was considered only horizontally, the position dependence of the amount of the deuteron was calculated along x.

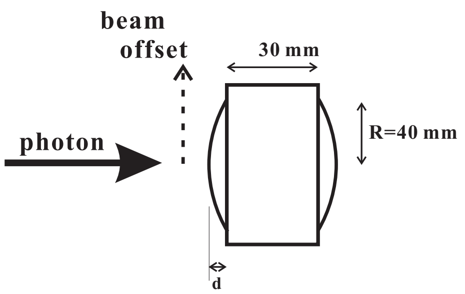

Appendix B

Invariant mass spectra for each bin in the momentum dependence of the cross section

In Sect. 3.7, to estimate the contribution of background, two background sources are considered. Hence, the magnitude of the backgrounds are derived by fitting the invariant mass spectrum in the photon region from 0.9 to 1.0 and from 1.0 to 1.1 GeV. However, it is not guaranteed that the fitting is good in any kinematical region. Figure B.1, B.2, B.3, B.4 show the invariant mass spectra by 50 MeV/c bin in the Fig. 3.42. Two backgrounds are consistent with the data in all region.

$0.9 \leq E_\gamma < 1.0$, Region 1

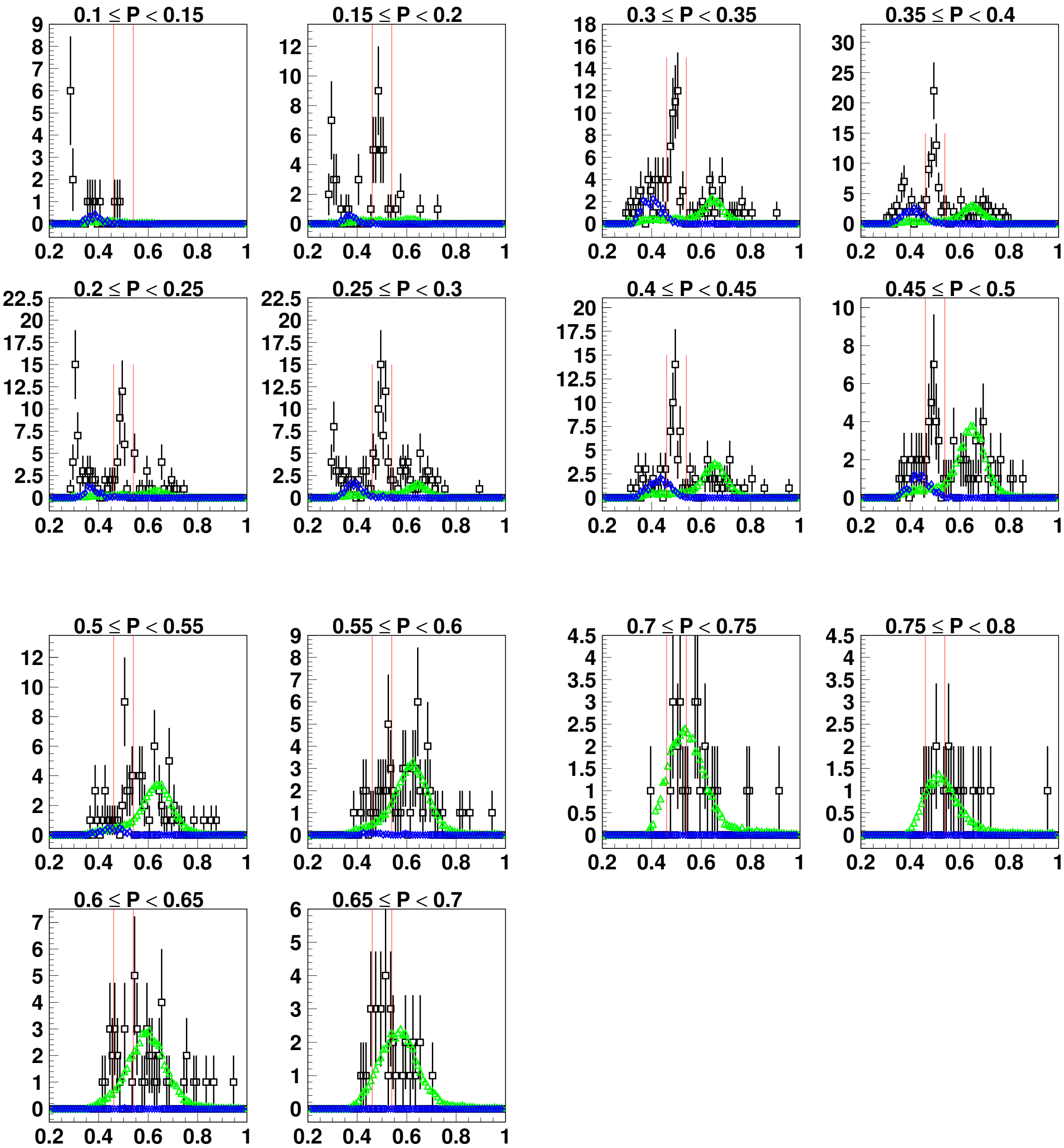

Figure B.1: *Invariant mass spectra in the Region 1 in the photon region from 0.9 to 1.0 GeV.*

$1.0 \leq E_\gamma < 1.1$, Region 1

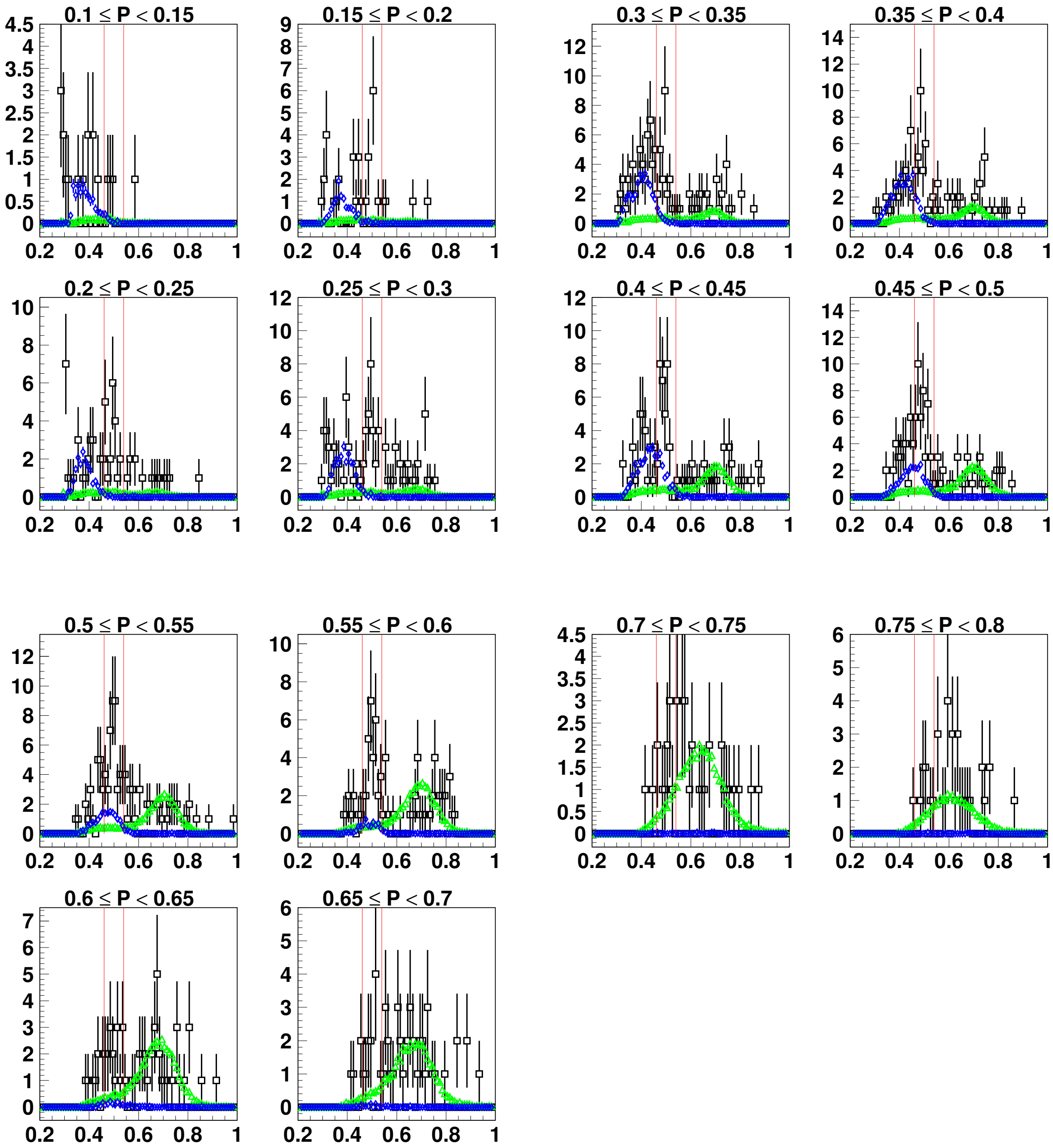

Figure B.2: *Invariant mass spectra in the Region 1 in the photon region from 1.0 to 1.1 GeV.*

$0.9 \leq E_\gamma < 1.0$, Region 2

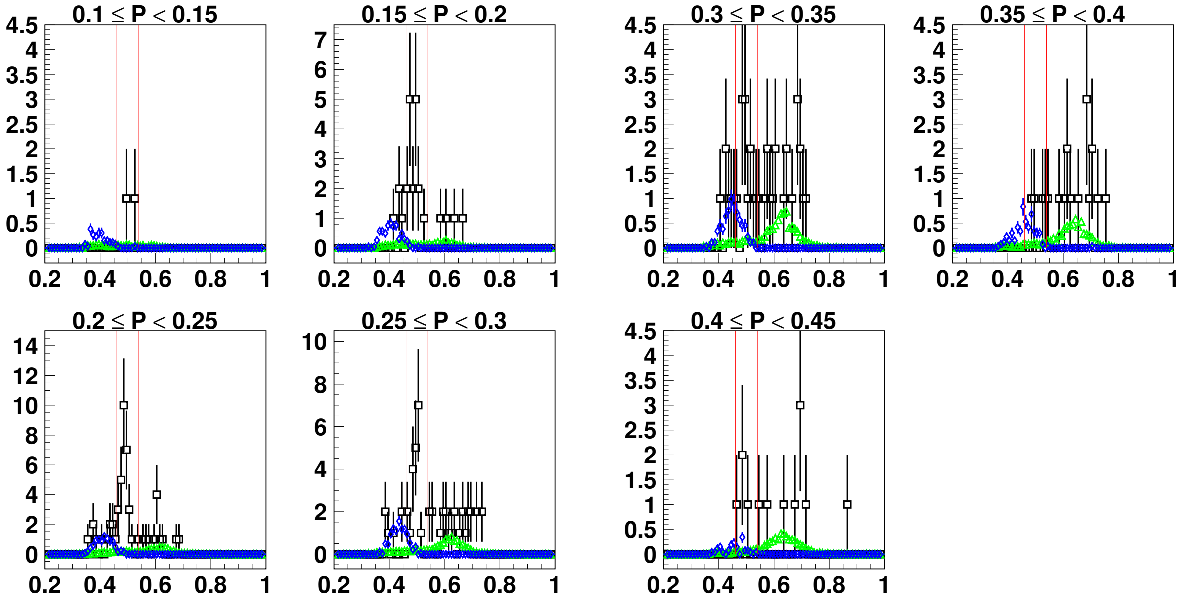

Figure B.3: *Invariant mass spectra in the Region 2 in the photon region from 0.9 to 1.0 GeV.*

$1.0 \leq E_\gamma < 1.1$, Region 2

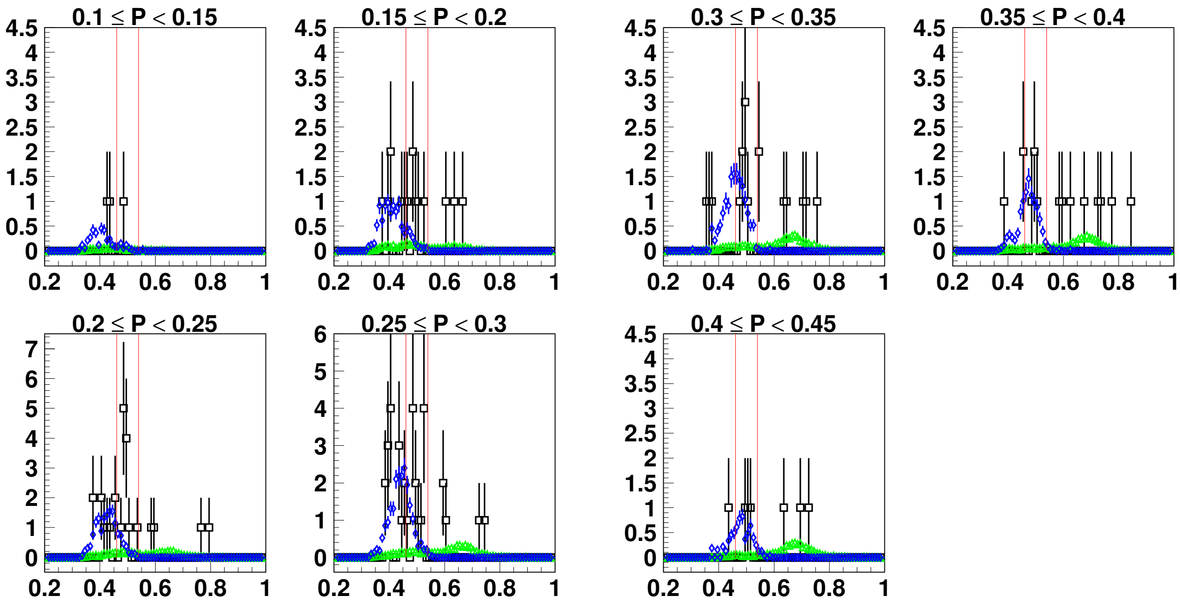

Figure B.4: *Invariant mass spectra in the Region 2 in the photon region from 1.0 to 1.1 GeV.*

Appendix C

Comparison of calculations with data in Region 2

Bibliography

[1] K. H. Glander et al., *Eur. Phys. J.*, A19:251–273, 2004.

[2] F. X. Lee, T. Mart, C. Bennhold, and L. E. Wright, *Nucl. Phys.*, A695:237–272, 2001.

[3] R. L. Anderson et al., *Phys. Rev. Lett.*, 9:131, 1968.

[4] Charles W. Peck, *Phys. Rev.*, 135:B830, 1964.

[5] D. E. Groom, *Phys. Rev.*, 159:1213, 1967.

[6] A. Bleckmann et. el., *Z. Phys.*, 239:1–15, 1970.

[7] T. Fujii et al., *Phys. Rev.*, D2:439–448, 1970.

[8] P. Feller, D. Menze, U. Opara, W. Schulz, and W. J. Schwille, *Nucl. Phys.*, B39:413–420, 1972.

[9] R. Erbe et al., *Phys. Rev.*, 188:2060–2077, 1969.

[10] K. H. Althoff et al., *Nucl. Phys.*, B137:269–275, 1978.

[11] ABBHHM collaboration, *Phys. Rev.*, 175:1669, 1968.

[12] C. N. Brown et al., *Phys. Rev. Lett.*, 28:1086–1089, 1972.

[13] C. J. Bebek et al., *Phys. Rev. Lett.*, 32:21–24, 1974.

[14] D. S. Carman et al., *Phys. Rev. Lett.*, 90:131804, 2003.

[15] J. W. C. McNabb et al., *Phys. Rev.*, C69:042201, 2004.

[16] M. Q. Tran et al., *Phys. Lett.*, B445:20–26, 1998.

[17] R. G. T. Zegers et al., *Phys. Rev. Lett.*, 91:092001, 2003.

[18] M. Guidal, J. M. Laget, and M. Vanderhaeghen, *Nucl. Phys.*, A627:645–678, 1997.

[19] Sven Steininger and Ulf-G. Meissner, *Phys. Lett.*, B391:446–450, 1997.

[20] R. A. Adelseck and B. Saghai, *Phys. Rev.*, C42:108–127, 1990.

[21] R. A. Williams, C. R. Ji, and S. R. Cotanch, *Phys. Rev.*, C46:1617–1635, 1992.

[22] J. C. David, C. Fayard, G. H. Lamot, and B. Saghai, *Phys. Rev.*, C53:2613–2637, 1996.

[23] H. Thom, *Phys. Rev.*, 151:1322, 1966.

[24] R. A. Adelseck, C. Bennhold, and L. E. Wright, *Phys. Rev.*, C32:1681–1692, 1985.

[25] R. A. Adelseck and L. E. Wright, *Phys. Rev.*, C38:1965–1967, 1988.

[26] C. Bennhold and L. E. Wright, *Phys. Rev.*, C39:927–941, 1989.

[27] R. A. Williams, C. R. Ji, and S. R. Cotanch, *Phys. Rev.*, C43:452–455, 1991.

[28] Ron L. Workman, *Phys. Rev.*, C44:552–553, 1991.

[29] T. Mizutani, C. Fayard, G. H. Lamot, and B. Saghai, *Phys. Rev.*, C58:75–90, 1998.

[30] Stijn Janssen, Jan Ryckebusch, Dimitri Debruyne, and Tim Van Cauteren, *Phys. Rev.*, C65:015201, 2002.

[31] H. Haberzettl, C. Bennhold, T. Mart, and T. Feuster, *Phys. Rev.*, C58:40–44, 1998.

[32] T. Mart and C. Bennhold, *Phys. Rev.*, C61:012201, 2000.

[33] Simon Capstick and W. Roberts, *Phys. Rev.*, D58:074011, 1998.

[34] T. Watanabe, *Doctoral thesis, Tohoku Univ., 2005.*

[35] H. Yamazaki et al., *Phys. Rev.*, C52:1157–1160, 1995.

[36] K. Maruyama et al., *Nucl. Instrum. Meth.*, A376:335–355, 1996.

[37] H.Wind, *Nucl. Instrum. Meth.*, 1974.

[38] J. W. Tukey, *Introduction to Today's Data Analysis, Proceedings of the Conference on Critical Evaluation of Chemical and Physical Structural Information*, 1974.

[39] H. Haberzettl, C. Bennhold, and T. Mart, *Nucl. Phys.*, A684:475–477, 2001.

[40] T. Feuster and U. Mosel, *Phys. Rev.*, C59:460–491, 1999.

[41] S. Eidelman et al., *Phys. Lett.*, B592:1, 2004.

[42] P. Bydzovsky, M. Sotona, O. Hashimoto, and T. Takahashi, 2004.

[43] X. Li and L. E. Wright, *J. Phys.*, G17:1127–1137, 1991.

[44] R. Machleidt, K. Holinde, and C. Elster, *Phys. Rept.*, 149:1–89, 1987.